Eclética Química Journal

Volume 45 • number 1 • year 2020

Proposed structures of the complexes at B3LYP/6-31G** level

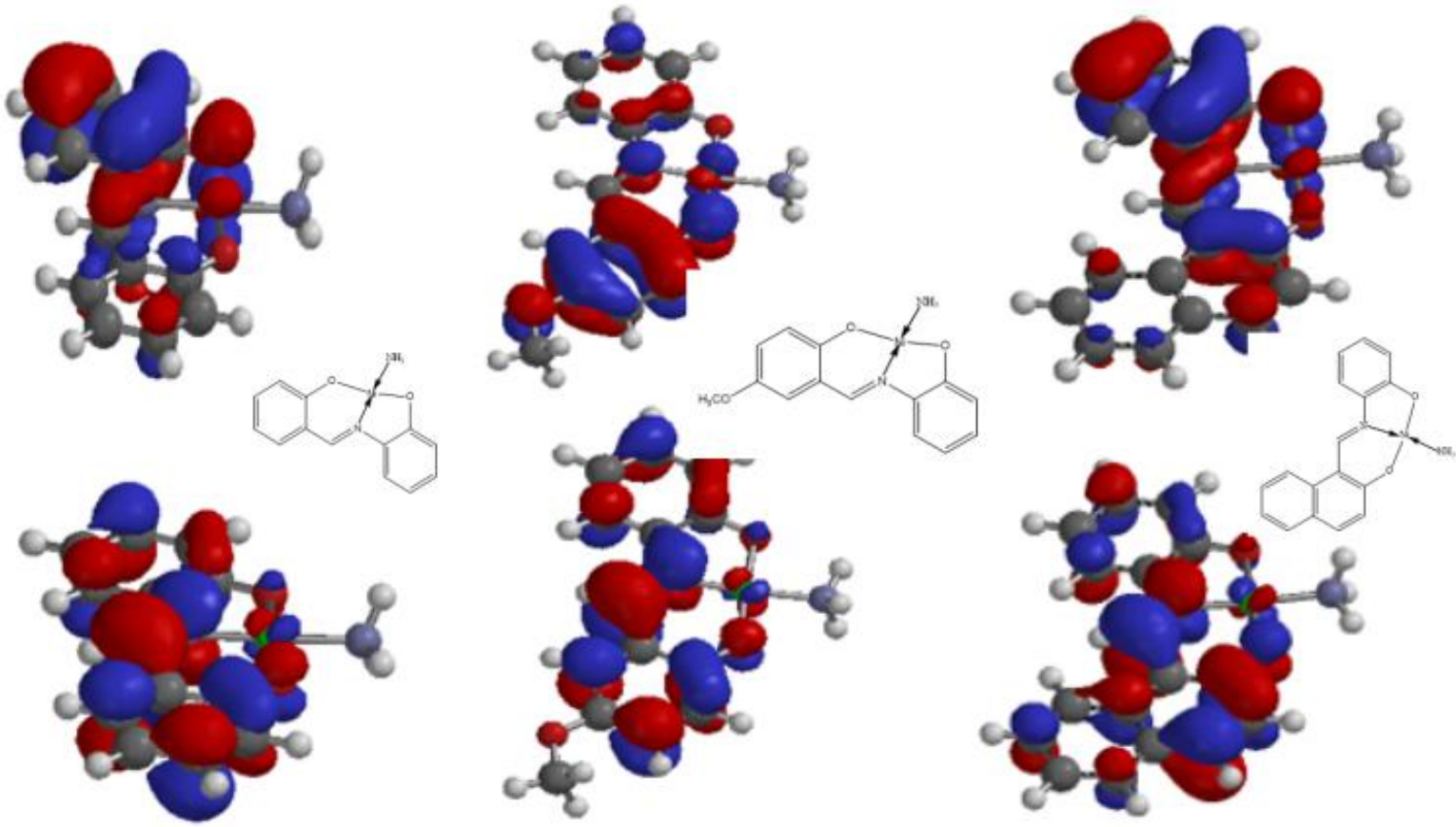

Estimating bulk density in leguminous grains with different traits using color parameters from digital images combined with artificial neural networks

Determination of harpagoside in Harpagophytum procumbens DC tablet's using analytical method by high performance liquid chromatography

Bound state solutions of the Schrödinger equation with energy-dependent molecular Kratzer potential via asymptotic iteration method

Synthesis, spectroscopic, biological activities and DFT calculations of nickel (II) mixed-ligand complexes of tridentate Schiff bases

Grain-size mineral analysis of verdete rock coarse and fine aggregates and adjustment to two granulometric distribution models

unesp
UNIVERSIDADE ESTADUAL PAULISTA
"JÚLIO DE MESQUITA FILHO"

Instituto de Química
UNESP
Araraquara

ISSN 1678-4618

UNIVERSIDADE ESTADUAL PAULISTA

Reitor

Sandro Roberto Valentini

Vice-Reitor

Sergio Roberto Nobre

Pró-Reitor de Planejamento Estratégico e Gestão

Leonardo Theodoro Büll

Pró-Reitora de Graduação

Gladis Massini-Cagliari

Pró-Reitora de Pós-Graduação

Telma Teresinha Berchielli

Pró-Reitora de Extensão Universitária

Cleopatra da Silva Planeta

Pró-Reitor de Pesquisa

Carlos Frederico de Oliveira Graeff

INSTITUTO DE QUÍMICA

Diretor

Eduardo Maffud Cilli

Vice-Diretora

Dulce Helena Siqueira Silva

Eclética Química Journal

Editorial team
iq.unesp.br/ecletica

| Vol. 45 | n. 1 | 2020 |

Editorial Team

Eclética Química Journal

Editorial
iq.unesp.br/ecletica

| Vol. 45 | n. 1 | 2020 |

Editorial

The Editor is very happy to announce the first issue of **Eclética Química Journal** of 2020, which contains varied and interesting subjects for the readers. The first article combines the color parameters of digital images with artificial neural networks (ANN) to predict the bulk density in leguminous grains of different traits. The challenge of estimating physicochemical properties of dry grains includes variations in shape, texture, and size and similarity of grains colors to the naked eye. The study allowed to obtain a very good correlation between the reference values and values predicted by the ANN. In the sequence, the synthesis, characterization using different physicochemical techniques, and theoretical calculations on the optimized structures of the Ni(II) mixed-ligand complexes are presented and discussed. The Schiff bases are coordinated to the Ni(II) ion via the two deprotonated phenolic oxygen and azomethine nitrogen atoms. The presented complexes, according to biological studies, demonstrated to have antibacterial and antioxidant properties. Following, a satisfactory method for identification and quantification of a widely used medicinal plant, species *Harpagophytum procumbens* DC, is described using high-performance liquid chromatography allows the quality control of commercial products. The importance of this medicinal plant is promptly recognized due to the anti-inflammatory properties, which are attributed to an iridoid glycoside. Afterwards, it is well known that the continuous research endeavors for the optimization of mineral resource utilization efforts, justified by the primacy of the mineral industry and the need to fulfill the demand of the global market. In this sense, mineral characterization may be the first step, which was here achieved by grain-size analysis of coarse and fine aggregates of verdete rock and the methodology used represents a contribution to the mineral characterization. This issue of EQJ is closed with the description of how to obtain of exact bound state energy spectrum of the Schrödinger equation with energy dependent molecular Kratzer potential, using asymptotic iteration method. Particularly, the influence of the energy-dependent Kratzer potential on some diatomic molecules is described.

The Editor and his team thank all the authors for their effective contributions, and the reviewers for their excellent evaluation of the manuscripts, wishing everyone a prosperous year in 2020.

Assis Vicente Benedetti
Editor-in-Chief of EQJ

Eclética Química Journal

Author guidelines
iq.unesp.br/ecletica

| Vol. 45 | n. 1 | 2020 |

Instructions for Authors

Preparation of manuscripts

• **Only manuscripts in English will be accepted.** British or American usage is acceptable, but they should not be mixed.

• **The corresponding author should submit the manuscript online at**
http://revista.iq.unesp.br/ojs/index.php/ecletica/author

• **Manuscripts must be sent in editable files as** *.doc, *.docx or *.odt. The text must be typed using font style Times New Roman and size 11. Space between lines should be 1.5 mm and paper size A4.

• **The manuscript should be organized in sections as follows:** Introduction, Experimental, Results and Discussion, Conclusions, and References. Sections titles must be written in bold and sequentially numbered; only the first letter should be in uppercase letter. Subsections should be written in normal and italic lowercase letters. For example: **1. Introduction**; *1.1 History;* **2. Experimental**; *2.1 Surface characterization; 2.1.1 Morphological analysis.*

• **The cover letter should include**: the authors' full names, e-mail addresses, ORCID code and affiliations, and remarks about the novelty and relevance of the work. The cover letter should also contain a declaration of the corresponding author, on behalf of the other authors, that the article being submitted is original and its content has not been published previously and is not under consideration for publication elsewhere, that no conflict of interest exists and if accepted, the article will not be published elsewhere in the same form, in any language, without the written consent of the publisher. Finally, the cover letter should also contain the suggestion of 3 (three) suitable reviewers (please, provide full name, affiliation, and e-mail).

• **The first page of the manuscript** should contain the title, abstract and keywords. **Please, do not give authors names and affiliation, and acknowledgements since a double-blind review system is used. Acknowledgements should be added to the proof only.**

• **All contributions should include** an Abstract (200 words maximum), three to five Keywords and a Graphical Abstract (8 cm wide × 4 cm high) with an explicative text (2 lines maximum).

• **Citations should be sequentially numbered** and presented in square brackets throughout the text, and references should be compiled in square brackets at the end of the manuscript as follows:

***Journal*:**

[1] Adorno, A. T. V., Benedetti, A. V., Silva, R. A. G. da, Blanco, M., Influence of the Al content on the phase transformations in Cu-Al-Ag Alloys, Eclet. Quim. 28 (1) (2003) 33-38. https://doi.org/10.1590/S0100-46702003000100004.

***Book*:**

[2] Wendlant, W. W., Thermal Analysis, Wiley-Interscience, New York, 3rd ed., 1986, ch1.

***Chapter in a book*:**

[3] Ferreira, A. A. P., Uliana, C. V., Souza Castilho, M. de, Canaverolo Pesquero, N., Foguel, N. V., Pilon dos Santos, G., Fugivara, C. S., Benedetti, A. V., Yamanaka, H., Amperometric Biosensor for Diagnosis of Disease, In: State of the Art in Biosensors - Environmental and Medical Applications, Rinken, T., ed., InTech: Rijeka, Croatia, 2013, Ch. 12.

***Material in process of publication*:**

[4] Valente Jr., M. A. G., Teixeira, D. A., Lima Azevedo, D., Feliciano, G. T., Benedetti, A. V., Fugivara, C. S., Caprylate Salts Based on Amines as Volatile Corrosion Inhibitors for Metallic Zinc: Theoretical and Experimental Studies, Frontiers in Chemistry. https://doi.org/10.3389/fchem.2017.00032.

• Figures, Schemes, and Tables should be numbered sequentially and presented at the end of the manuscript.

• Nomenclature, abbreviations, and symbols should follow IUPAC recommendations.

• Figures, schemes, and photographs already published by the same or different authors in other publications may be reproduced in manuscripts of **Eclet. Quim. J.** only with permission from the editor house that holds the copyright.

• Graphical Abstract (GA) should be a high-resolution figure (900 dpi) summarizing the manuscript in an interesting way to catch the attention of the readers and accompanied by a short explicative text (two lines maximum). GA must be submitted as *.jpg, *.jpeg or *.tif.

• **Communications** should cover relevant scientific results and are limited to 1,500 words or three pages of the Journal, not including the title, authors' names, figures, tables and references. However, Communications suggesting fragmentation of complete contributions are strongly discouraged by Editors.

• **Review articles** should be original and present state-of-the-art overviews in a coherent and concise form covering the most relevant aspects of the topic that is being revised and indicate the likely future directions of the field. Therefore, before beginning the preparation of a Review manuscript, send a letter (one page maximum) to the Editor with the subject of interest and the main topics that would be covered in the Review manuscript. The Editor will communicate his decision in two weeks. Receiving this type of manuscript does not imply acceptance to be published in **Eclet. Quím. J.** It will be peer-reviewed.

• **Short reviews** should present an overview of the state-of-the-art in a specific topic within the scope of the Journal and limited to 5,000 words. Consider a table or image as corresponding to 100 words. Before beginning the preparation of a Short Review manuscript, send a letter (one page maximum) to the Editor with the subject of interest and the main topics that would be covered in the Short Review manuscript.

• **Technical Notes**: descriptions of methods, techniques, equipment or accessories developed in the authors' laboratory, as long as they present chemical content of interest. They should follow the usual form of presentation, according to the peculiarities of each work. They should have a maximum of 15 pages, including figures, tables, diagrams, etc.

• **Articles in Education in Chemistry and chemistry-correlated areas**: research manuscript related to undergraduate teaching in Chemistry and innovative experiences in undergraduate and graduate education. They should have a maximum of 15 pages, including figures, tables, diagrams, and other elements.

Special issues with complete articles dedicated to Symposia and Congresses can be published by **Eclet. Quim. J.** under the condition that a previous agreement with Editors is established. All the guides of the journal must be followed by the authors.

Eclet. Quim. J. Ethical Guides and Publication Copyright:

Before beginning the submission process, please be sure that all ethical aspects mentioned below were followed. Violation of these ethical aspects may prevent authors from submitting and/or publishing articles in **Eclet. Quim. J.**

- The corresponding author is responsible for listing as coauthors only researchers who have really taken part in the work, for informing them about the entire manuscript content and for obtaining their permission to submit and publish it.

- Authors are responsible for carefully searching for all the scientific work relevant to their reasoning irrespective of whether they agree or not with the presented information.

- Authors are responsible for correctly citing and crediting all data used from works of researchers other than the ones who are authors of the manuscript that is being submitted to **Eclet. Quim. J.**

- Citations of Master's Degree Dissertations and PhD Theses are not accepted; instead, the publications resulting from them must be cited.

- Explicit permission of a nonauthor who has collaborated with personal communication or discussion to the manuscript being submitted to **Eclet. Quím. J.** must be obtained before being cited.

- Simultaneous submission of the same manuscript to more than one journal is considered an ethical deviation and is conflicted to the declaration has been done below by the authors.

- Plagiarism, self-plagiarism, and the suggestion of novelty when the material was already published are unaccepted by **Eclet. Quim. J.**

- The word-for-word reproduction of data or sentences as long as placed between quotation marks and correctly cited is not considered ethical deviation when indispensable for the discussion of a specific set of data or a hypothesis.

- Before reviewing a manuscript, the *Turnitin* antiplagiarism software will be used to detect any ethical deviation.

- The corresponding author transfers the copyright of the submitted manuscript and all its versions to **Eclet. Quim. J.**, after having the consent of all authors, which ceases if the manuscript is rejected or withdrawn during the review process.

- Before submitting manuscripts involving human beings, materials from human or animals, the authors need to confirm that the procedures established, respectively, by the institutional committee on human experimentation and Helsinki's declaration, and the recommendations of the animal care institutional committee were followed. Editors may request complementary information on ethical aspects.

- When a published manuscript in EQJ is also published in other Journal, it will be immediately withdrawn from EQJ and the authors informed of the Editor decision.

• Manuscript Submissions

For the first evaluation: the manuscripts should be submitted in three files: the cover letter as mentioned above, the graphical abstract and the entire manuscript.

The entire manuscript should be submitted as *.doc, *.docx or *.odt files.

The Graphical Abstract (GA) 900 dpi resolution is mandatory for this Journal and should be submitted as *.jpg, *.jpeg or *.tif files as supplementary file.

The cover letter should contain the title of the manuscript, the authors' names and affiliations, and the relevant aspects of the manuscript (no more than 5 lines), and the suggestion of 3 (three) names of experts in the subject: complete name, affiliation, and e-mail).

When appropriate, important data to complement and a better comprehension of the article can be submitted as Supplementary File, which will be published online and will be made available as links in the original article. This might include additional figures, tables, text, equations, videos or other materials that are necessary to fully document the research contained in the paper or to facilitate the readers' ability to understand the work. Supplementary Materials should be presented in appropriate .docx file for text, tables, figures and graphics. The full title of the paper, authors' names and affiliations, and corresponding author should be included in the header. All supplementary figures, tables and videos should be referred in the manuscript body as "Table S1, S2…", "Fig. S1, S2…" and "Video S1, S2 …".

• Reviewing

The time elapsed between the submission and the first response of the reviewers is around 3 months. The average time elapsed between submission and publication is seven months.

• **Resubmission** (manuscripts "rejected in the present form" or subjected to "revision"): **A LETTER WITH THE RESPONSES TO THE COMMENTS/CRITICISM AND SUGGESTIONS OF REVIEWERS/EDITORS SHOULD ACCOMPANY THE REVISED MANUSCRIPT. ALL MODIFICATIONS MADE TO THE ORIGINAL MANUSCRIPT MUST BE HIGHLIGHTED.**

• Editor's requirements

Authors who have a manuscript accepted in **Eclética Química Journal** may be invited to act as reviewers.

Only the authors are responsible for the correctness of all information, data and content of the manuscript submitted to **Eclética Química Journal**. Thus, the Editors and the Editorial Board cannot accept responsibility for the correctness of the material published in **Eclética Química Journal**.

• Proofs

After accepting the manuscript, **Eclet. Quim. J.** technical assistants will contact you regarding your manuscript page proofs to correct printing errors only, i.e., other corrections or content improvement are not permitted. The proofs shall be returned in 3 working days (72 h) via e-mail.

• Authors Declaration

The corresponding author declares, on behalf of the other authors, that the article being submitted is original and has been written by the stated authors who are all aware of its content and approve its submission. Declaration should also state that the article has not been published previously and is not under consideration for publication elsewhere, that no conflict of interest exists and if accepted, the article will not be published elsewhere in the same form, in any language, without the written consent of the publisher.

• Appeal

Authors may only appeal once about the decision regarding a manuscript. To appeal against the Editorial decision on your manuscript, the corresponding author can send a rebuttal letter to the editor, including a detailed response to any comments made by the reviewers/editor. The editor will consider the rebuttal letter, and if dimmed appropriate, the manuscript will be sent to a new reviewer. The Editor decision is final.

• Contact

Gustavo Marcelino de Souza (ecletica@journal.iq.unesp.br)

Submission Preparation Checklist

As part of the submission process, authors are required to check off their submission's compliance with all of the following items, and submissions may be returned to authors that do not adhere to these guidelines.

In **Step 1**, select the appropriate section for this submission.

Be sure that Authors' names, affiliations and aknowledgements were removed from the manuscript. The manuscript must be in *.doc, *.docx or *.odt format before uploading in **Step 2**.

In **Step 3**, add the full name of each author including the ORCID IDs in its full URL ONLY WITH HTTP, NOT HTTPS (eg. http://orcid.org/0000-0002-1825-0097).

Add the authors in the same order as they appear in the manuscript in **step 3**.

Be sure to have the COVER LETTER and GRAPHICAL ABSTRACT (according to the Author Guildelines) to upload them in **Step 4**.

Check if you've followed all the previous steps before continuing the submission of your manuscript.

Copyright Notice

The corresponding author transfers the copyright of the submitted manuscript and all its versions to **Eclet. Quim. J.**, after having the consent of all authors, which ceases if the manuscript is rejected or withdrawn during the review process.

Self-archive to institutional, thematic repositories or personal web page is permitted just after publication.

Eclética Química Journal

Summary
ig.unesp.br/ecletica

| Vol. 45 | n. 1 | 2020 |

SUMMARY

Eclética Química Journal

Original article
iq.unesp.br/ecletica

| Vol. 45 | n. 1 | 2020 |

Estimating bulk density in leguminous grains with different traits using color parameters from digital images combined with artificial neural networks

Bruna Gava Floriam, Fabíola Manhas Verbi Pereira, Érica Regina Filletti*

São Paulo State University (Unesp), Institute of Chemistry, 55 Prof. Francisco Degni St, Araraquara, São Paulo, Brazil

*Corresponding author: Érica Regina Filletti, Phone: +55 16 3301-9839 email address: erica.filletti@unesp.br

ARTICLE INFO

Article history:
Received: December 18, 2018
Accepted: September 17, 2019
Published: January 1, 2020

Keywords:
1. grain
2. digital images
3. bulk density
4. learning algorithm
5. error propagation

ABSTRACT: Dry grains from leguminous species, such as soybeans (*Glycine max* L.), common beans (*Phaseolus vulgaris* L.), chickpeas (*Cicer arietinum* L.) and corn (*Zea mays* L.), are regularly consumed for human nutrition. This paper showed the possibility of estimating bulk density as quality parameter of 4 different dry grains (soybeans, common beans, chickpeas and corn) in a same model using the average values of color descriptors from digital images combined with an artificial neural network, with low computational costs. These food products are good sources of carbohydrates, protein and dietary fiber, and they possess significant amounts of vitamins and minerals and a high energetic value. Estimation of the physicochemical properties of grains is challenging due to variations in shape, texture, and size and because the grain colors appear similar to the naked eye. In this work, an analytical method was developed based on digital images converted into ten color scale descriptors combined with a neural model to provide an accurate parameter for grain quality control with a low computational cost. The bulk densities of four type of grains, i.e., soybeans, beans, chickpeas and corn, were predicted using numerical data represented by the average values of color histograms of a ten color scale (red - R, green - G, blue - B, hue - H, saturation - S, value - V, relative RGB and luminosity - L) from digital images combined with artificial neural networks (ANNs). The reference bulk densities were empirically measured. A very good correlation between the reference values and values predicted by the ANN was achieved, and with a single ANN developed for the four grains, a correlation coefficient of 0.98 was observed for the test set. Moreover, the relative errors were between 0.01 and 5.6% for the test set.

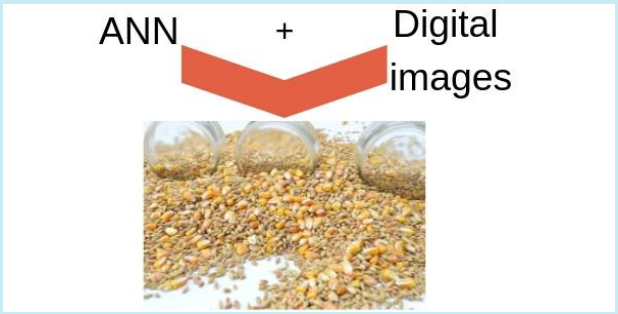

1. Introduction

Soybeans (*Glycine max* L.), common beans (*Phaseolus vulgaris* L.), chickpeas (*Cicer arietinum* L.) and corn (*Zea mays* L.) are a part of most human diets, regardless of culture. These grains are leguminous species consumed as dry grains. They are remarkable sources of carbohydrates, protein and dietary fiber, and they possess significant amounts of vitamins and minerals and a high energetic value[1].

The quality of food grains is dependent on several physicochemical parameters, including the bulk density (or density in each mass). In a grain, the bulk density is more closely related to its shape than its size[2]. Stored food materials can suffer from variations in bulk density according to the bin depth[3]. Thus, a model that can monitor this parameter would be helpful to avoid losses in agri-food supply chains. For instance, in the study by Bart-Plange and Baryeh[4] several laborious physicochemical methods were applied to evaluate cocoa beans, as the raw material for manufacturing chocolate and other food products, including the determination of their bulk density.

Using the method presented here, the quality of four types of grains can be estimated using an accurate approach based on a relevant

physicochemical parameter, i.e., the bulk density, which is related to the storage system, type of container and characteristics of the grains.

Color data from digital images are considered reliable sources of analytical information for many purposes, independent of the type of device, for example, scanners, cell phones or cameras[5]. The combination of digital images and an artificial neural network (ANN) can be adapted for applications such as the shape analysis of grains[6] and for variety identification[7]. However, in both cited studies, many complex steps were necessary to develop a predictive response model with good accuracy.

The advantage of this study is that additional information from a color histogram of a ten color scale[8,9] can be determined using a simple computational routine with fast calculations. In addition, by using the average color values instead of the entire color histogram, which includes 2560 colors[10,11], the speed of the ANN calculations is improved, and accurate results are achieved. Therefore, ANNs are useful tools for this research because they require less computational effort than other numerical techniques.

ANNs are computational models consisting of simple processing units called neurons, which are inspired by the central nervous system of intelligent organisms that acquire knowledge through experimentation; ANNs can perform machine learning to predict parameters and recognize patterns[12,13].

Initially, an ANN undergoes a learning phase in which some examples are presented to it during training, and it automatically extracts the necessary characteristics to represent the information learned by adjusting the synaptic weights of the neurons through an adequate learning algorithm. Then, these characteristics are used to generate answers to the problem studied. In other words, by providing input data to an ANN and reporting the desired output (response), the ANN can provide coherent results for new input data that are different from those used in training.

There are several advantages to using ANNs; for instance, ANNs are easy to use and update, they have data error tolerance because of the ability to respond in an acceptable way, even if partially damaged, they have great freedom in the adjustment of synaptic weights of neurons due to the presence of bias, which is a special processing unit that allows better adaptation on the part of the neural network to the knowledge provided to it, and they provide a precise response at high speeds[14-16]. The main advantage of ANNs is their ability to generalize or learn from examples[17]; that is, ANNs can generalize learned information to provide satisfactory results for cases not seen in training. Therefore, ANNs have been used in many fields, such as chemistry[18], geology[19], medicine[20], neurocomputations[21] and biomedical engineering[22], among others.

In this sense, after an ANN has been trained and tested, it can predict the output (desired response) of new input data in the domain covered by the training examples. For food analysis, data from digital images acquired using both a camera and a desktop scanner have been applied to predict the fermentation index of cocoa beans by ANN modeling[23]. An ANN was also combined with digital images and showed excellent potential for wheat varietal identification[24] using the morphometric characteristics of these grains for the classification of different varieties with 88% accuracy and individual varieties with 84% and 94% accuracy.

Our study shows a feasible analytical method based on digital images converted into ten color scale descriptors combined with an ANN to estimate the bulk density of leguminous grains such as soybeans, beans, chickpeas and corn.

2. Materials and methods

2.1. Procurement of samples and instruments

Grains of soybeans, beans, chickpeas and corn were purchased locally. The grains were sorted to eliminate external material and damaged grains. For the tests, the grains were separated in small packets made of transparent plastic bags (10 × 6 cm), as shown in Fig. 1. According to the size of the grains, each plastic bag was filled with 100 soybeans, 100 beans, 50 chickpeas, or 100 kernels of corn, resulting in 56 packets of soybeans, 35 packets of beans, 30 packets of chickpeas and 50 packets of corn.

The content of each packet was weighed on an analytical balance with ±0.0001 g precision (FA-2104N, EQUIPAR, Curitiba, PR, Brazil), and the apparent volume was measured with graduated cylinders with a volume of (50.0±0.5) mL for soybeans, corn and beans and with a volume of (100±1) mL for chickpeas. Using the measured masses (m) and apparent volumes (V), the bulk

Eclética Química Journal, vol. 45, n. 1, 2020, 11-17
ISSN: 1678-4618
DOI: 10.26850/1678-4618eqj.v45.1.2020.p11-17

densities of the samples were estimated using the ratio $\rho = \frac{m}{V}$, and these values were considered the reference values in this study.

Figure 1. Examples of the scanned images of soybean (A), bean (B), chickpea (C) and corn (D) grains.

Then, each packet was digitalized using a conventional scanner (HP, LaserJet Pro 200 Color MFP M276nw, Brazil). The final size of the images was 550 × 1000 pixels with a resolution of 96 dots per inch (dpi).

2.2. Image treatment

The digital images were processed and converted into the average values of ten color scale descriptors, red (R), green (G), blue (B), hue (H), saturation (S), value (V), relative red (Rr), relative green (Rg), relative blue (Rb) and luminosity (L), using the Matlab R2015b (The MathWorks, Natick, MA, USA) code available in the supplementary material of Camargo, Santos and Pereira[8]. Figure 2 shows an image of the data. Using this code, the average value of each histogram color, which includes 256 colors, is obtained; thus, each color is represented by one value per color histogram.

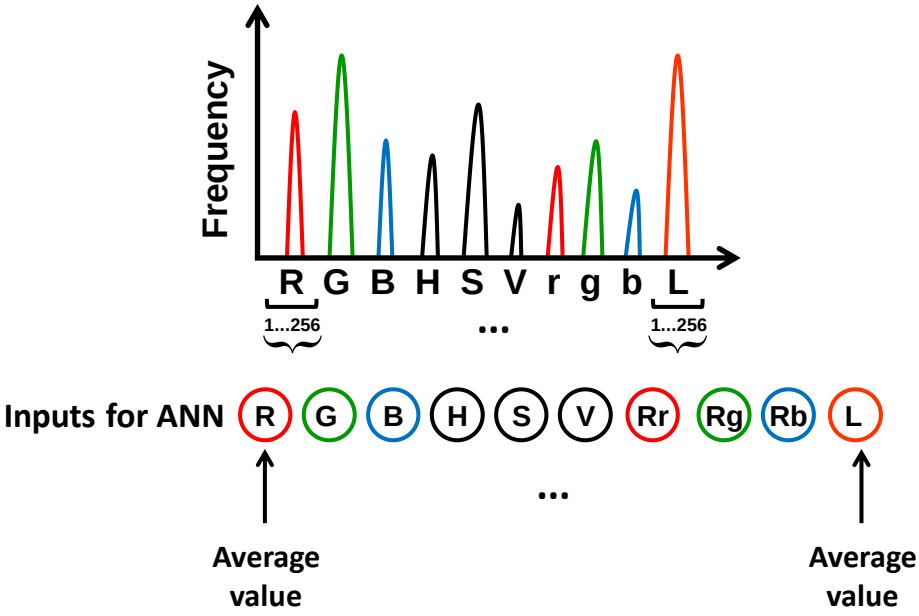

Figure 2. Diagram of the input data for the ANN calculations

2.3. ANN description

A feedforward neural network[25] was implemented in Matlab R2015b. Two learning algorithms were tested in the development of the ANN: error backpropagation and the Levenberg-Marquardt algorithm. The Levenberg-Marquardt algorithm presented correlation coefficients in the mean of 0.88 and RMSE (Root Mean Square Error) equal to 0.031 for the test set, while the backpropagation algorithm provided results with correlation coefficient equal 0.98 and RMSE 0.014. Therefore, the backpropagation algorithm provided the best results and is described briefly below[12,13]:

1) Set the initial parameters of the network $w_{i,j}$ and $b_{i,j}$ (weights and bias) as random numbers.

2) From a training data set with pre-assigned input/output pairs, take the k-th (p_i^k, a_i^k) pair, calculate the outputs of the network with the same input, and form the new pair (p_i^k, t_i^k).

Eclética Química Journal, vol. 45, n. 1, 2020, 11-17
ISSN: 1678-4618
DOI: 10.26850/1678-4618eqj.v45.1.2020.p11-17

3) Calculate the error between the desired a_i^k and the obtained t_i^k output values through the formula

$$e = \sqrt{\sum_i \left(a_i^k - t_i^k\right)^2} \quad (1)$$

4) Calculate the partial derivatives of error e with respect to the weights and bias.

5) Change the weights and bias according to the steepest descent strategy and a specified learning rate α:

$$b_{i,j} \leftarrow b_{i,j} - \alpha \frac{\partial e}{\partial b_{i,j}} \quad (2)$$

and

$$w_{i,j} \leftarrow w_{i,j} - \alpha \frac{\partial e}{\partial w_{i,j}} \quad (3)$$

6) Iterate steps 2 to 5 by successively modifying $b_{i,j}$ and $w_{i,j}$ until a defined number of learning cycles or a stopping criterion is reached.

The parameter learning rate, number of neurons per layer, number of layers, activation functions and number of epochs were varied by trial and error to obtain the best result, and early stopping of the training was performed to avoid overtraining.

3. Results and discussion

The ranges of bulk density measured using the reference method were in g cm^{-3} for soybean between 0.61 and 0.65, bean (0.75-0.78), chickpea (0.63-0.68) and corn (0.68-0.85). The variation of values among the colors converted from the images were: (i) soybean grains: R (174–192), G (128–135), B (83–91), H (0.079–0.081), S (0.52–0.57), V (0.68–071), r (0.46–0.48), g (0.32–0.33), b (0.19–0.21), and L (386–407); (ii) bean grains: R (140–147), G (91–99), B (63–72), H (0.066–0.072), S (0.56–0.61), V (0.55–0.58), r (0.51–0.53), g (0.29–0.30), b (0.18–0.20), and L (294–317); chickpea grains: R (167–174), G (131–137), B (103–111), H (0.070–0.074), S (0.39– 0.42), V (0.66–0.68), r (0.43–0.44), g (0.318–0.321), b (0.24–0.25), and L (401–421) and (iv) corn grains: R (196–217), G (122–145), B (75–100), H (0.06–0.07), S (0.55–0.64), V (0.77–0.85), r (0.49–0.53), g (0.30–0.31), b (0.17–0.20), and L (397–461). In all of cases, differences among the samples were revealed that justify an ANN model using the 10 colors as input layer. Tests were also performed without variables H and L, for example, showed worse than all input variables were used. For this case, the correlation coefficients were 0.94, 0.84 and 0.92 for training, validation and test sets, respectively. Therefore, the input variables of the ANN training set were the R, G, B, H, S, V, Rr, Rg, Rb and L color descriptors, for a total of 10 input variables for each packet of grain sample; that is, the developed ANN had 10 neurons in the input layer (Fig. 2). The strategy of averaged value of each histogram color was applied because the entire histogram for the 10 colors corresponds to 2560 variables. For the ANN, 2560 values imply 2560 neuron in input layer, then the calculations would be slower than that computed using the averaged color values, mainly considering that the information would not be improved. The information from the hue (H) and saturation (S) color scales was also important as revealed by our previous evaluation[8].

The ANN outputs were the reference bulk density values. The samples were randomly divided into three sets as follows: a total of 70% of the samples were used in the ANN training set, 15% was used for the validation of ANN, and the remaining 15% was used to test the generalizability of the ANN. The training set consisted of 119 samples, i.e., 38 soybean, 19 bean, 24 chickpea and 38 corn samples, the validation set had 26 samples, i.e., 8 soybean, 10 bean, 2 chickpea and 6 corn samples, and the test set had 26 samples, i.e., 10 soybean, 6 bean, 4 chickpea and 6 corn samples. The number of samples were related to the size of the grains and the size of the packet (plastic bag) was the same. The main goal was to analyze the entire packet then the variation in size of the grain had determined the number of packets, which did not affect ANN results, since it was not necessary for ANN to know which grain sample was being analyzed to estimate grain density in each packet.

A single ANN was developed for all four types of grains (soybeans, beans, chickpeas and corn). Several ANN architectures were tested with one intermediate layer (varying the number of neurons from 10 to 20) and with two intermediate layers (with 8 and 4 neurons in each layer, respectively). The ANN that obtained the best result had only one intermediate layer with 15 neurons, and its performance was below 10^{-3} for the mean square error obtained after 1500 epochs, as shown in Fig. 3. The training was interrupted in 1500 epochs to avoid excessive adjustment by ANN, which could lead to an overfitting. The activation functions were a hyperbolic tangent function in

Eclética Química Journal, vol. 45, n. 1, 2020, 11-17
ISSN: 1678-4618
DOI: 10.26850/1678-4618eqj.v45.1.2020.p11-17

the intermediate layer and a linear function in the output layer.

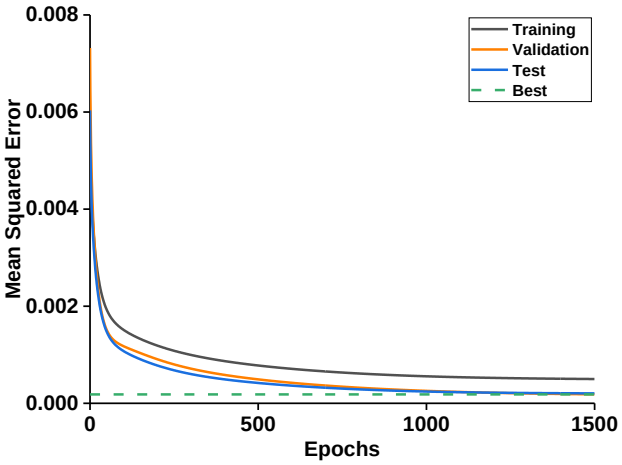

Figure 3. ANN performance results for the training, validation and test sets. The green dotted line denoted as "best" shows the lowest value of the mean square error reached in the ANN validation in 1500 epochs.

The highest efficiency for the four types of grains together had a learning rate of 0.8. Training was also performed with higher and lower learning rates, but the network became unstable with learning rates below 0.3, meaning that it failed to provide good results for the test samples. At a learning rate of 0.8, the ANN was stable, and the training was very fast (close to 1 min). The training error was small, approximately 10^{-3}, and it was stable throughout the learning process.

Among the four types of grains used in this work, the corn grains are the least uniform, that is, they present the most variation in density (between 0.68 e 0.85 g cm^{-3}), so the estimated values were more distributed along the linear adjustment, as shown in the Fig. 4. And the values of bean grains density (0.75-0.78 g cm^{-3}) are within the range of corn grains density, which agrees with the results obtained for these two grains. On the other hand, soybean and chickpea grains are more uniform with little variation in density.

The plots in Fig. 4 show a high correlation of 0.94 between the reference bulk density values and the values predicted by the ANN model for both the training sets (Fig. 4A) and a correlation coefficient of 0.98 for the data from both validation and test sets (Fig. 4B and 4C). The best fit equations for the training, validation and test data are

$y = 0.86x + 0.10$, $y = 0.92x + 0.057$, and $y = 0.90x + 0.069$, respectively.

The mean relative error was 2.1, 1.5 and 1.4% for the training, validation and test data, respectively, with the lowest and highest relative errors of the ANN responses for the test set samples between 0.01 and 5.6%, which is a noteworthy result.

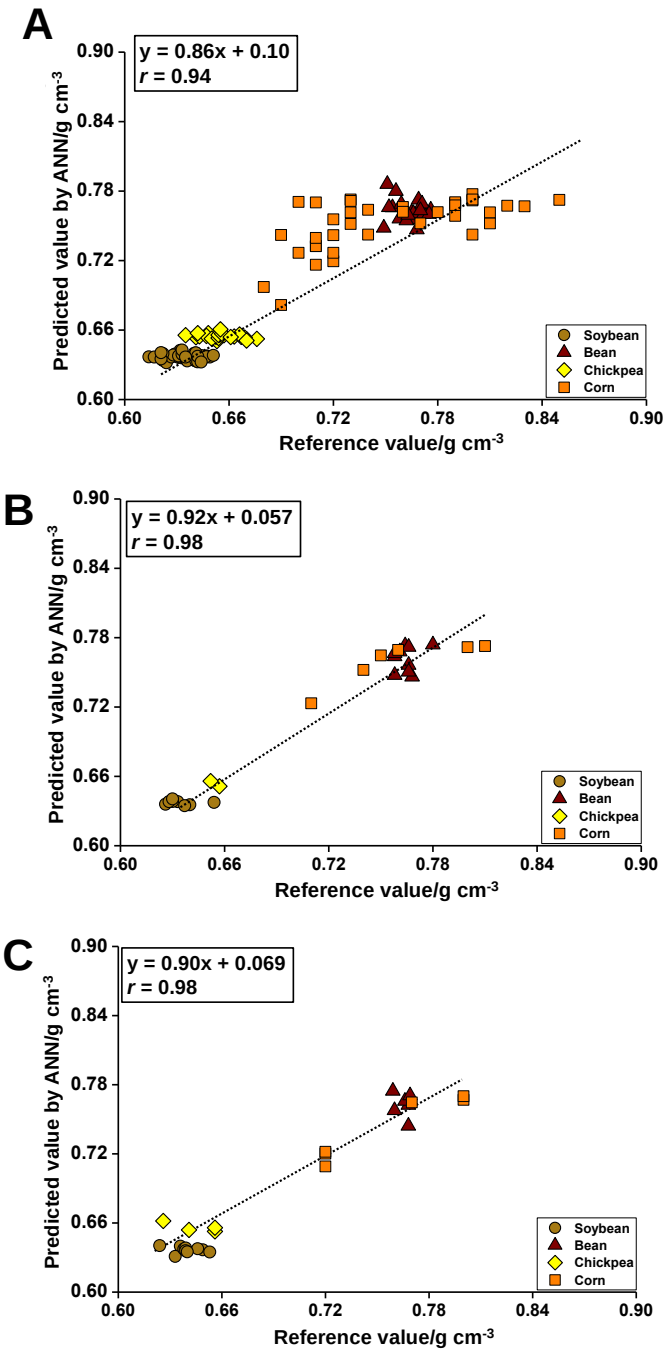

Figure 4. Predicted bulk densities (g cm^{-3}) obtained by the ANN model using image color data of the grains (soybean, bean, chickpea and corn) for the training (A), validation (B) and test (C) sets.

Eclética Química Journal, vol. 45, n. 1, 2020, 11-17
ISSN: 1678-4618
DOI: 10.26850/1678-4618eqj.v45.1.2020.p11-17

The accuracy of the results is shown by the plots in Fig. 5, giving the equations $y = 0.90x + 0.10$ and $y = 0.90x + 0.036$, which envelop the results obtained by the ANN calculations. These equations were based on calculations involving the linear regression of the test set (Fig. 4C), replacing the term x by each reference value and summing the linear coefficient to 3 times the standard deviation obtained for the absolute errors (difference between the reference values and those predicted by the ANN) of the 26 samples. Thus, for a given bulk density ρ, the response of the neural network will be in the interval $[\rho - 0.03, \rho + 0.03]$, where $[\rho - 3\sigma_r, \rho + 3\sigma_r]$ and $\sigma_r = 0.01$; a range with a very small amplitude indicates high reliability in the ANN response.

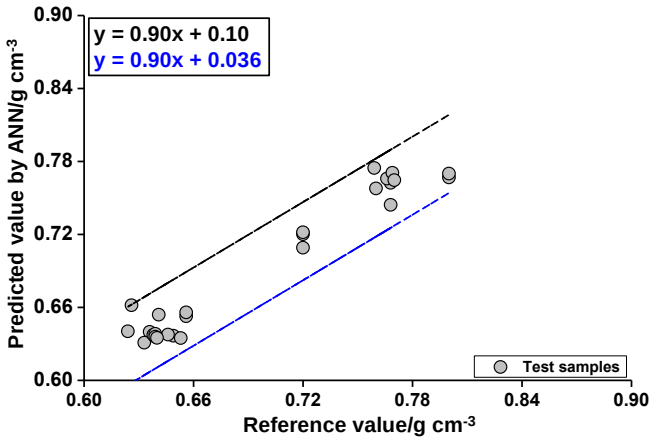

Figure 5. Bulk densities (g cm^{-3}) of soybean, bean, chickpea and corn provided by the ANN for the test set samples.

4. Conclusions

The bulk densities of four different dry grains were accurately estimated using the average values of color descriptors from digital images combined with an ANN. This method is promising, considering that these grain foods have similar colors and different shapes and textures. The reference values and the values predicted by the ANN model were highly correlated (r = 0.98) for the test set, with low relative errors between 0.01 and 5.6%. Thus, our study showed the possibility of using an ANN to provide accurate grain quality control parameters with low computational costs.

5. Acknowledgments

This work was supported by the São Paulo Research Foundation (FAPESP) (grant numbers 2015/20813-1 and 2016/00779-6).

6. References

[1] Costa, G. E. A., Queiroz-Monici, K. S., Reis, S. M. P. M., Oliveira, A. C., Chemical composition, dietary fibre and resistant starch contents of raw and cooked pea, common bean, chickpea and lentil legumes, Food Chemistry 94 (3) (2006) 327-330. https://doi.org/10.1016/j.foodchem.2004.11.020.

[2] Bhattacharya, K. R., Rice quality, A guide to rice properties and analysis. Woodhead Publishing Series Limited, Cambridge, 2013.

[3] Haque, E., Estimating bulk density of compacted grains in storage bins and modifications of Janssen's load equations as affected by bulk density, Food Science & Nutrition 1 (2) (2013) 150-156. https://doi.org/10.1002/fsn3.23.

[4] Bart-Plange, A., Baryeh, E. A., The physical properties of Category B cocoa beans, Journal of Food Engeneering 60 (3) (2003) 219-227. https://doi.org/10.1016/S0260-8774(02)00452-1.

[5] Wong, J. X. H., Liu, F. S. F., Yu, H. Z., Mobile app-based quantitative scanometric analysis, Analytical Chemistry 86 (24) (2014) 11966-11971. https://doi.org/10.1021/ac5035727.

[6] Shouche, S. P., Rastogi, R., Bhagwat, S. G., Sainis, J. K., Shape analysis of grains of Indian wheat varieties, Computers and Electronics in Agriculture 33 (1) (2001) 55-76. https://doi.org/10.1016/S0168-1699(01)00174-0.

[7] Chen, X., Xun, Y., Li, W., Zhang, J., Combining discriminant analysis and neural networks for corn variety identification, Computers and Electronics in Agriculture 71 (S1) (2010) S48-S53. https://doi.org/10.1016/j.compag.2009.09.003.

[8] Camargo, V. R., Santos, L. J., Pereira, F. M. V., A Proof of Concept Study for the Parameters of Corn Grains Using Digital Images and a Multivariate Regression Model, Food Analytical Methods 11 (7) (2018) 1852-1856. https://doi.org/10.1007/s12161-017-1028-6.

Eclética Química Journal, vol. 45, n. 1, 2020, 11-17
ISSN: 1678-4618
DOI: 10.26850/1678-4618eqj.v45.1.2020.p11-17

[9] Santos, P. M., Wentzell, P. D., Pereira-Filho, E. R., Scanner digital images combined with color parameters: a case study to detect adulterations in liquid cow's milk, Food Analytical Methods 5 (1) (2012) 89-95. https://doi.org/10.1007/s12161-011-9216-2.

[10] Borin, A., Ferrão, M. F., Mello, C., Cordi, L., Pataca, L. C. M., Durán, N., Poppi, R. J., Quantification of *Lactobacillus* in fermented milk by multivariate image analysis with least-squares support-vector machines, Analytical & Bioanalytical Chemistry 387 (2007) (3) 1105-1112. https://doi.org/10.1007/s00216-006-0971-7.

[11] Pereira, F. M. V., Milori, D. M. B. P., Pereira-Filho, E. R., Venâncio, A. L., Russo, M. S. T., Martins, P. K., Freitas-Astúa, J., Fluorescence images combined to statistic test for fingerprinting of citrus plants after bacterial infection, Analytical Methods 3 (2011) 552-556. https://doi.org/10.1039/C0AY00538J.

[12] Hagan, M. T., Demuth H. B, Beale M., Neural network design. PWS Publishing Company, Boston, 1996.

[13] Haykin, S., Neural Networks: a comprehensive foundation. Prentice Hall, New Jersey, 1999.

[14] Li, G., Shi, J., On comparing three artificial neural networks for wind speed forecasting, Applied Energy 87 (7) (2010) 2313-2320. https://doi.org/10.1016/j.apenergy.2009.12.013.

[15] Nafey, A. S., Neural network based correlation for critical heat flux in steam-water flows, International Journal of Thermal Sciences 48 (12) (2009) 2264-2270. https://doi.org/10.1016/j.ijthermalsci.2009.04.010.

[16] Niemi, H., Bulsari, A., Palosaari, S., Simulation of membrane separation by neural networks, Journal of Membrane Science 102 (1995) 185-191. https://doi.org/10.1016/0376-7388(94)00314-O.

[17] Zhang, Z., Friedrich, K., Artificial neural networks applied to polymer composites: a review, Composites Science and Technology 63 (14) (2003) 2029-2044. https://doi.org/10.1016/S0266-3538(03)00106-4.

[18] Tanzifi, M., Yaraki, M. T., Kiadehi, A. D., Hosseini, S. H., Olazar, M., Bharti, A. K., Agarwal, S., Gupta, V. K., Kazemi, A., Adsorption of Amido Black 10B from aqueous solution using polyaniline/ SiO_2 nanocomposite: Experimental investigation and artificial neural network modelling, Journal of Colloid and Interface Science 510 (2018) 246-261. https://doi.org/10.1016/j.jcis.2017.09.055.

[19] Ramil, A., López, A. J., Rivas, T., A computer vision system for identification of granite-forming minerals based on RGB data and artificial neural networks, Measurement 117 (2018) 90-95. https://doi.org/10.1016/j.measurement.2017.12.006.

[20] Walczak, S., Velanovich, V., Improving prognosis and reducing decision regret for pancreatic cancer treatment using artificial neural networks, Decision Support Systems 106 (2018) 110-118. https://doi.org/10.1016/j.dss.2017.12.007.

[21] Ortega-Zamorano, F., Jerez, J. M., Juarez, G. E., Franco, L., FPGA Implementation of Neurocomputational Models: Comparison Between Standard Back-Propagation and C-Mantec Constructive Algorithm, Neural Processing Letters 46 (3) (2017) 899-914. https://doi.org/10.1007/s11063-017-9655-x.

[22] Filletti, É. R., Roque, W. L., Estimating the mechanical competence parameter of the trabecular bone: a neural network approach, Research in Biomedical Engineering 32 (2) (2016) 137-143. https://doi.org/10.1590/2446-4740.05615.

[23] León-Roque, N., Abderrahim, M., Nuñez-Alejos, L., Arribas, S. M., Condezo-Hoyos, L., Prediction of fermentation index of cocoa beans (*Theobroma cacao* L.) based on colour measurement and artificial neural networks, Talanta 161 (1) (2016) 31-39. https://doi.org/10.1016/j.talanta.2016.08.022.

[24] Dubey, B. P., Bhagwat, S. G., Shouche, S. P., Sainis, J. K., Potential of Artificial Neural Networks in Varietal Identification using Morphometry of Wheat Grains, Biosystems Engineering 95 (1) (2006) 61-67. https://doi.org/10.1016/j.biosystemseng.2006.06.001.

[25] Demuth, H., Beale, M., Hagan, M., Neural Network toolbox™ 6: User's Guide. The Math Works, Natick, 2010.

Eclética Química Journal, vol. 45, n. 1, 2020, 11-17
ISSN: 1678-4618
DOI: 10.26850/1678-4618eqj.v45.1.2020.p11-17

Eclética Química Journal

Original article
iq.unesp.br/ecletica

| Vol. 45 | n. 1 | 2020 |

Synthesis, spectroscopic, biological activities and DFT calculations of nickel(II) mixed-ligand complexes of tridentate Schiff bases

Abidemi Iyewumi Demehin[1], Mary Adelaide Oladipo[2+], Banjo Semire[2]

1 Adeyemi College of Education, Department of Chemistry, Ondo, Ondo State, Nigeria
2 Ladoke Akintola University of Technology, Department of Pure and Applied Chemistry, Ogbomoso, Oyo State, Nigeria

+Corresponding author: Mary Adelaide Oladipo, Phone: +234 803 3817017 email address: mooladipo@lautech.edu.ng

ARTICLE INFO

Article history:
Received: March 02, 2019
Accepted: November 11, 2019
Published: January 1, 2020

Keywords:
1. Schiff bases
2. antibacterial
3. antioxidant
4. nickel(II) ion
5. mixed-ligand complex

ABSTRACT: Ni(II) mixed-ligand complexes of [NiLNH$_3$] (where L = N-salicylidene-o-aminophenol (L_1), N-(5-methoxysalicylidene-o-aminophenol) (L_2) and N-(2-hydroxy-1-naphthalidene)-o-aminophenol) (L_3) containing ONO tridentate Schiff bases and ammonia were synthesized and characterized by elemental analysis, infrared, ultraviolet-visible, proton and carbon-13 spectroscopies. Theoretical calculations were also performed on the optimized structures of the Ni(II) mixed-ligand complexes. The infrared and ultraviolet-visible spectra of the complexes were calculated, and the results compared with the corresponding experimental spectra to augment the experimental structural identification. The elemental analysis data confirmed the formation of 1:1:1 [metal:Schiff base:ammonia] molar ratio. The NMR spectra showed that the Schiff bases coordinated to the Ni(II) ion via the two deprotonated phenolic oxygen and azomethine nitrogen atoms. The biological studies showed that the complexes exhibited higher antibacterial and antioxidant activities than the free Schiff base ligands.

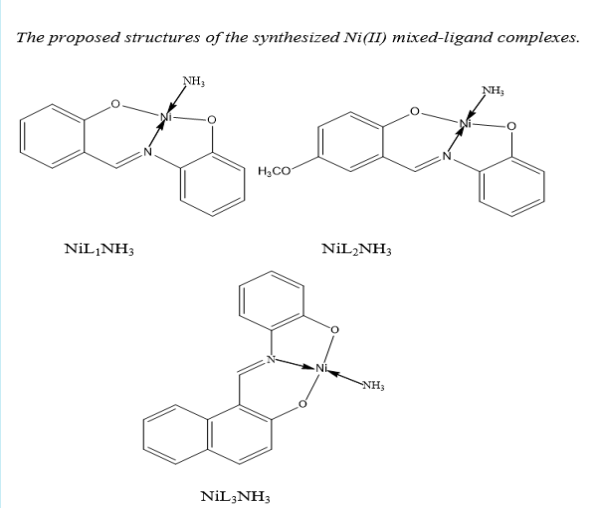

1. Introduction

Schiff bases are compounds that are comparable to ketone or aldehyde, they have azomethine (HC=N) group instead of the carbonyl (C=O) group in the carbonyl compounds. Schiff bases can also be called azomethines or imines[1,2]. They were discovered by Hugo Schiff in 1864[3]. They have the general formula $RR_1C{=}N{-}R_2$. If R equals hydrogen, alkyl or aryl, R_1 hydrogen and R_2 alkyl or aryl; the compounds are referred to as aldimines ($R_1{-}CH{=}NR_2$) while compounds where both R and R_1 are alkyl or aryl groups are called ketoimines. R_2 can either be an alkyl or aryl group[4-6]. They are significant chelating ligands in coordination chemistry. Their chemical properties can be changed by varying the substituents on either the carbonyl or the amine ring. Intra- and intermolecular hydrogen bonds can be formed from Schiff bases obtained from various substituted salicylaldehydes and 2-hydroxyl-1-naphthaldehyde and these usually determine their chemical and physicochemical properties[7]. They have vital donor atoms like nitrogen and oxygen which make them resemble living systems and display different biological properties. The resulting imines are involved in binding with metal ions via nitrogen lone pair of electrons. Schiff bases can bind to the central metal ions as monodentate and polydentate[8,9]. Schiff bases lead to the formation of many mononuclear and binuclear complexes with different coordination modes and stereochemistry[8].

The imine groups in Schiff bases are significant for biological activities, they are very useful active centers of many biological systems[10]. Schiff bases have played essential roles in understanding the coordination chemistry of transition metal ions. Studies showed that Schiff bases derived from salicylaldehyde, 2-hydroxyl-1-naphthaldehyde including the derivatives and complexes with some transition metals displayed significant biological properties which make them gain attention. Some of the reported significant biological properties are anti-inflammatory, antimicrobial, analgesic, anticonvulsant and antioxidants which make them attract more attention[1,11-19].

Many mixed-ligand complexes have been synthesized for their pronounced biological activities. However, literature search showed that reports on mixed-ligand complexes bearing ammonia as co-ligand are less explored. Hence this study, which synthesized, characterized, and carried out the biological and theoretical studies of nickel(II) mixed-ligand complexes of tridentate Schiff bases and ammonia. Besides the experimental studies, quantum chemical methods were used to augment the experimental observations[9]. Therefore, the molecular structures of the Schiff base ligands and complexes were modelled, and the theoretical calculations were carried out on their optimized structures. These were utilized for their IR, UV-Vis and NMR spectra. A consideration of the similarities between the calculated and experimental spectra, mostly the electronic spectra could further be used for identification of the molecular geometry.

2. Experimental

2.1. Materials

Salicylaldehyde, 5-methoxysalicylaldehyde, 2-hydroxy-1-naphthaldehyde, *o*-aminophenol, nickel(II) acetate tetrahydrate, ammonium hydroxide and formic acid were purchased from Merck (Germany) and used as supplied. The solvents were of pure grade except ethanol and water which were distilled.

2.2. Instruments

A Thermo Finnigan Flash EA 1112 Series was used for the elemental analyses (C, H, N). The Infrared spectroscopy analysis were carried out using the attenuated (ATR) technique with a Perkin-Elmer 400 FT-IR/FT-FIR spectrometer. An MPD Mitamura Riken Kogyo (Japan) electrothermal was used to determine the melting points. The nuclear magnetic resonance spectra were carried out on a Bruker Avance III 600 Spectrometer in solution with DMSO-d_6 and tetramethylsilane (TMS) as internal standard at 600 MHz. The UV-Visible spectra were recorded in 1.0×10^{-4} mol L^{-1} DMSO solution using Shimadzu UV-2600 Spectrophotometer in the range 250-900 nm.

2.3. Syntheses

2.3.1. The Schiff bases syntheses

5.0 mmol of the *o*-aminophenol in 10 mL of ethanol was added in drops to 5.0 mmol of the corresponding salicylaldehyde in 20 mL of the same solvent. The resulting solution was stirred for 2 h on addition of three drops of formic acid. The colored solids precipitated were separated by filtration and recrystallized from hot ethanol.

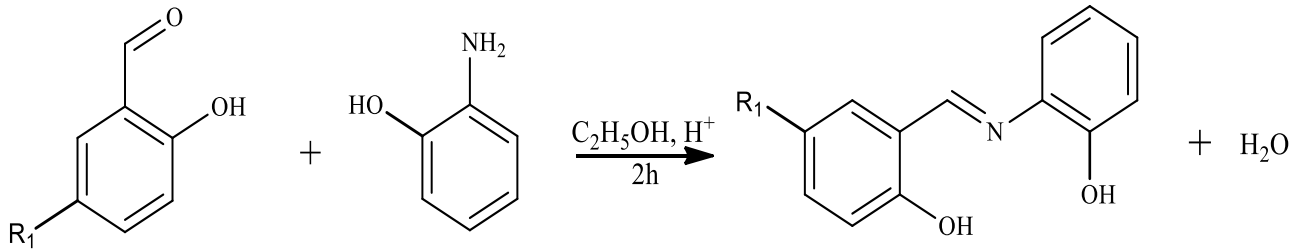

L_1: R_1 = H; L_2: R_1 = OCH_3; L_3: R_1 = C_4H_4

Scheme 1. Synthetic route of the Schiff bases.

L_1 ($C_{13}H_{11}NO_2$): Yield: 97%, orange solid, mol wt: 213.14, m.pt: 187 °C. Elemental analysis, % (found) C: 73.25, H: 5.21, N: 6.60; calculated C: 73.23, H: 5.20, N: 6.57. FT-IR (ATR, cm^{-1}): 3746, 3046, 2696, 2533, 1970, 1840, 1627, 1613, 1592, 1529, 1506, 1486, 1459, 1415, 1369, 1309, 1274,

Eclética Química Journal, vol. 45, n. 1, 2020, 18-43
ISSN: 1678-4618
DOI: 10.26850/1678-4618eqj.v45.1.2020.p18-43

1241, 1220, 1176, 1159, 1137, 1115, 1097, 1047, 1019, 967, 945, 902, 853, 806, 763, 741, 725, 630, 572, 547, 525, 475. ^{1}H NMR: 13.78 (s, 1H, −OH), 9.73 (s, 1H, −OH), 8.92 (s, 1H, −HC=N), 7.56-6.84 (m, 8H, aromatic).

L_2 ($C_{14}H_{13}NO_3$): Yield: 95%, deep wine solid, mol wt: 243.14, m.pt: 157 °C. Elemental analysis % (found) C: 69.10, H: 5.38, N: 5.77; calculated C: 69.12, H: 5.39, N: 5.77. FT-IR (cm^{-1}) 3747, 3046, 2987, 2942, 2896, 2832, 2687, 2561, 2071, 1839, 1626, 1591, 1527, 1494, 1494, 1456, 1437, 1417, 1330, 1300, 1273, 1247, 1221, 1204, 1165, 1143, 1131, 1098, 1039, 941, 931, 869, 854, 811, 787, 738, 663, 589, 566, 549, 516, 499, 479, 471. ^{1}H NMR: 13.07 (s, 1H, −OH), 9.68 (s, 1H, −OH), 8.89 (s, 1H, −HC=N), 7.29-6.82 (m, 7H, aromatic), 3.71 (s, 3H, −OCH_3).

L_3 ($C_{17}H_{13}NO_2$): Yield: 86%, yellow solid, mol wt: 263.29, m.pt: 249 °C. Elemental analysis % (found) C: 77.56, H: 5.00, N: 5.29; calculated, C: 77.55, H: 4.98, N: 5.32. FT-IR (cm^{-1}) 3119, 3017, 2925, 2427, 2175, 1617, 1584, 1547, 1547, 1513, 1459, 1407, 1354, 1316, 1270, 1238, 1210, 1170, 1140, 1114, 1039, 993, 968, 920, 854, 825, 774, 740, 647, 594, 577, 549, 519, 482, 467. ^{1}H NMR: 13.62 (s, 1H, −OH), 10.31 (s, 1H, −OH), 9.47 (s, 1H, −HC=N), 8.34-6.70 (m, 10H, aromatic)

2.3.1. Synthesis of the mixed-ligand complexes

A methanolic solution of $Ni(CH_3COO)_2.4H_2O$ (5.0 mmol) was added in drops to the corresponding Schiff base solution (5.0 mmol) while stirring in 10ml of the same solvent. Some drops of anhydrous ammonia were added to modify the pH of the resulting mixture to 7-7.5 and refluxed at 60 °C for 3 h. The colored solids precipitated were filtered by vacuum filtration, washed with distilled water, diethyl ether and methanol. These were dried over silica gel in a desiccator for two days and recrystallized from DMSO.

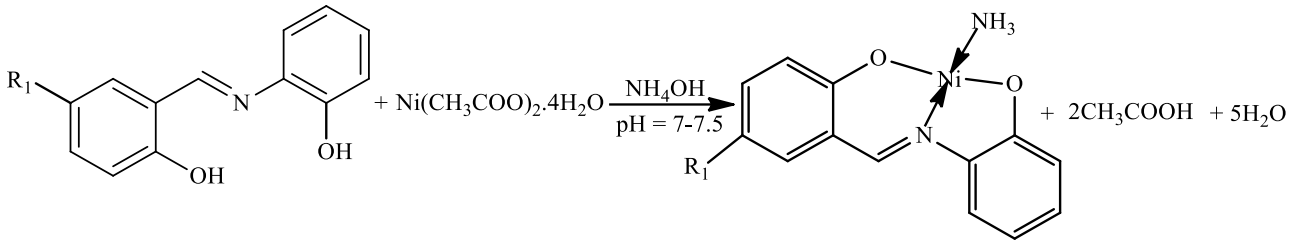

Scheme 2. Synthetic route of the Ni(II) mixed-ligand complexes.

NiL_1NH_3 ($C_{13}H_{12}N_2O_2Ni$): Yield: 85%, wine solid, mol wt.: 286.94. m.pt: > 260 °C. Elemental analysis % (found) C: 54.44, H: 4.23, N: 9.78; calculated C: 54.42, H: 4.22, N: 9.76. FT-IR (ATR, cm^{-1}): 3336, 3276, 3235, 3158, 3040, 3016, 2685, 2591, 2541, 2323, 2098, 1916, 1880, 1843, 1802, 1760, 1689, 1602, 1580, 1526, 1479, 1468, 1441, 1375, 1358, 1322, 1313, 1303, 1283, 1263, 1225, 1172, 1156, 1143, 1130, 1111, 1029, 960, 941, 926, 941, 926, 875, 840, 796, 772, 750, 743, 730, 695, 657, 614, 568, 546, 524, 484, 461. ^{1}H NMR (DMSO-d_6, δ, ppm): 8.79 (s, 1H, −HC=N), 7.75-6.46 (m, 8H, aromatic), 2.37 (s, 3H, −NH_3). ^{13}C NMR (DMSO-d_6, δ, ppm): 167.43, 162.96, 148.06, 139.55, 135.52, 134.04, 129.09, 120.83, 118.51, 116.56, 115.44, 114.75.

NiL_2NH_3 ($C_{14}H_{14}N_2O_3Ni$): Yield: 82%, wine solid, mol wt.: 316.97, m.pt: > 260 °C. Elemental analysis, % (found) C: 53.10, H: 4.47, N: 8.85; calculated C: 53.05, H: 4.45, N: 8.84. FT-IR (cm^{-1}): 3341, 3236, 3159, 2935, 2832, 2009, 1840, 1601, 1584, 1529, 1477, 1445, 1424, 1367, 1314, 1302, 1282, 1257, 1238, 1212, 1177, 1147, 1111, 1049, 1031, 952, 939, 898, 871, 846, 821, 804, 750, 994, 658, 643, 582, 567, 550, 522 503, 487, 474, 464, 456. ^{1}H NMR (DMSO-d_6, δ, ppm): 8.65 (s, 1H, −HC=N), 7.71-6.45 (m, 7H, aromatic), 3.69 (s, 3H, −OCH_3), 2.25 (s, 3H, −NH_3). ^{13}C NMR (DMSO-d_6, δ, ppm): 167.39, 158.49, 149.25, 147.55, 139.62, 129.15, 124.40, 121.55, 120.98, 118.56, 116.34, 114.79, 56.44.

NiL_3NH_3 ($C_{17}H_{14}N_2O_2Ni$): Yield: 84%, brown solid, mol wt.: 337, m.pt: > 260 °C. Elemental analysis % (found) C: 60.71, H: 4.09, N: 8.27; calculated C: 60.59, H: 4.19, N: 8.31. FT-IR (cm^{-1}): 3340, 3239, 3163, 3038, 2338, 2148, 1613, 1600, 1578, 1533, 1509, 1476, 1457, 1428, 1397, 1361, 1344, 1314, 1297, 1280, 1262, 1252, 1205, 1171, 1145, 1111, 1041, 1029, 986, 963, 912, 835, 817, 775, 757, 693, 670, 653, 587, 563, 508, 470, 457.

Eclética Química Journal, vol. 45, n. 1, 2020, 18-43
ISSN: 1678-4618
DOI: 10.26850/1678-4618eqj.v45.1.2020.p18-43

^{1}H NMR (DMSO-d_6, δ, ppm): 9.25 (s, 1H, −HC=N), 8.49-6.30 (m, 10H, aromatic), 2.37 (s, 3H, $-NH_3$). ^{13}C NMR (DMSO-d_6, δ, ppm): 167.18, 163.60, 141.43, 140.48, 134.85, 134.39, 129.17, 128.80, 128.01, 127.12, 124.19, 123.06, 121.66, 118.36, 116.78, 114.89, 111.71.

2.4. Antibacterial study

The antibacterial potentials of the compounds were measured against some Gram-positive and Gram-negative bacterial strains by agar-well diffusion method. The Gram-positive bacterial strains were *Streptococcus agalactiae* and *Staphylococcus aureus* while *Escherichia coli*, *Klebsiella pneumoniae*, *Proteus mirabilis*, *Pseudomonas aeruginosa* and *Salmonella typhimurium* were the Gram-negative bacterial strains used. The nutrient agar medium was used to sub-culture the isolates of bacterial strains which were nurtured at 37 °C for 24 h. 20 mL of disinfected nutrient agar medium was dispensed in each germfree Petri dish after modifying the bacterial strains cultures to 0.5 McFarland standards, these were allowed to gel. The dishes were swabbed with the inoculum of the bacterial strains and left for 15 min to adsorb unto the gel. Varying concentrations of the samples (5, 10 and 15 mg mL^{-1}) were filled into the wells that were drilled on the seeded agar dishes by a sterile cork borer of 6 mm diameter. These were kept for 1 h in the refrigerator to allow for thorough circulation of the samples into the medium and then nurtured for 24 h at 37 °C observing the inhibition zones. Antimicrobial activities were expressed as inhibition diameter zones in millimeter (mm). Standard Gentamycin (10 µg mL^{-1}) was employed as control[17,20,21].

2.5. Phosphomolybdate total antioxidant capacity (PTAC) assay

The total antioxidant capacities (TAC) of the compounds were determined by phosphomolybdenum assay and ascorbic acid was used as the standard. 1.0 mL of reagent (0.6 mol L^{-1} sulfuric acid, 28 µmol L^{-1} sodium phosphate and 4 µmol L^{-1} ammonium molybdate) was reacted with a fractional part of the extract solution (1.0 mL of 1000 µg). The covered tubes were incubated at 95 °C in a water bath for 90 min after which the samples were cooled to room temperature and a UV spectrophotometer was used to measure the absorbance of the aqueous solution of each at 695 nm. The procedure was repeated for an empty solution containing 1.0 mL of reagent solution. The TAC studies were performed three times and the mean was expressed as equivalents of ascorbic acid[22].

2.6. Computational method

The Ni(II) complexes were modeled and optimized using Gaussian 9 and Spartan 14 computational software packages which were implemented on an Intel Core i3-3100M computer. They were modeled based on the electronic spectra and elemental analyses data. Density functional theory (DFT) was employed for the geometry optimization, chemical shifts, electronic transitions and frequency calculations of the complexes. The DFT calculations were performed on the optimized geometry in the ground state using Becke's three-parameter hybrid functional employing the Lee-Yang-Parr correlation functional (B3LYP) and the Empirical Density Functional 1 methods (EDF1) with 6-31G** basis set[23-26].

3. Results and discussion

The Schiff base ligands and the mixed-ligand complexes were stable and colored solids. The complexes were not soluble in water and almost all organic solvents except in DMSO and DMF. The mixed-ligand complexes have higher melting points than the parent Schiff base ligands, this showed that they have better stability than the Schiff bases. Elemental analyses data indicated the formation of 1:1:1 [nickel:Schiff base:ammonia] molar ratio for the mixed-ligand complexes. The crystals obtained in DMSO were not suitable for X-ray diffraction measurement. No crystal was obtained in DMF. Attempts to isolate single crystal suitable for X-ray diffraction measurement were not successful.

3.1 Spectroscopic studies

3.1.1. FT-IR spectra

The spectra of the free Schiff base ligands (L_1, L_2 and L_3) showed the azomethine, ν(−HC=N) bands at 1627, 1617 and 1626 cm^{-1} respectively, these bands shifted to lower wavenumbers (1601-1600 cm^{-1}) in the mixed-ligand complexes (Figs. 1-3). This revealed the involvements of the

Eclética Química Journal, vol. 45, n. 1, 2020, 18-43
ISSN: 1678-4618
DOI: 10.26850/1678-4618eqj.v45.1.2020.p18-43

azomethine nitrogen atoms in coordination with the Ni(II) ions and the formation of metal−ligand bonds. The bands at 1274, 1228 and 1247 cm^{-1} in the spectra of the free Schiff base ligands were assigned to the phenolic C−O stretching vibrations of L_1, L_2 and L_3 respectively. These bands shifted to higher wave numbers at 1301-1261 cm^{-1} in the complexes, these showed the participation of the oxygen atoms of phenolic groups in coordination with the Ni(II) ions. The free Schiff bases (L_1, L_2 and L_3) exhibited hydroxyl ν(O−H) absorption bands at 3746, 3747 and 3119-2427 cm^{-1} respectively, these bands were absent in the complexes which further confirmed the deprotonation of the phenolic groups and coordination of oxygen to the Ni(II) ion[8,12,27]. The complexes showed new bands at 3336, 3340 and 3340 cm^{-1} respectively assigned to ν(N−H) stretching vibrations of ammonia ($–NH_3$) groups, these indicated the presence of $–NH_3$ groups in the complexes[28]. The complexes displayed the aromatic ν(C−H) and ν(C=C) absorption bands around 3276-3016 and 1584-1400 cm^{-1} respectively. The aromatic ν(C−H) bending vibrations appeared around 875-647 cm^{-1}. The bands around 485-471 and 550-508 cm^{-1} in the complexes were assigned to the stretching vibrations of the nickel–oxygen, ν(Ni−O) and nickel–nitrogen, ν(Ni−N) respectively. These confirmed the attachment of the Schiff bases to the central nickel ion through the phenolic oxygen atoms and the azomethine nitrogen atoms[8,11,17].

Eclética Química Journal, vol. 45, n. 1, 2020, 18-43
ISSN: 1678-4618
DOI: 10.26850/1678-4618eqj.v45.1.2020.p18-43

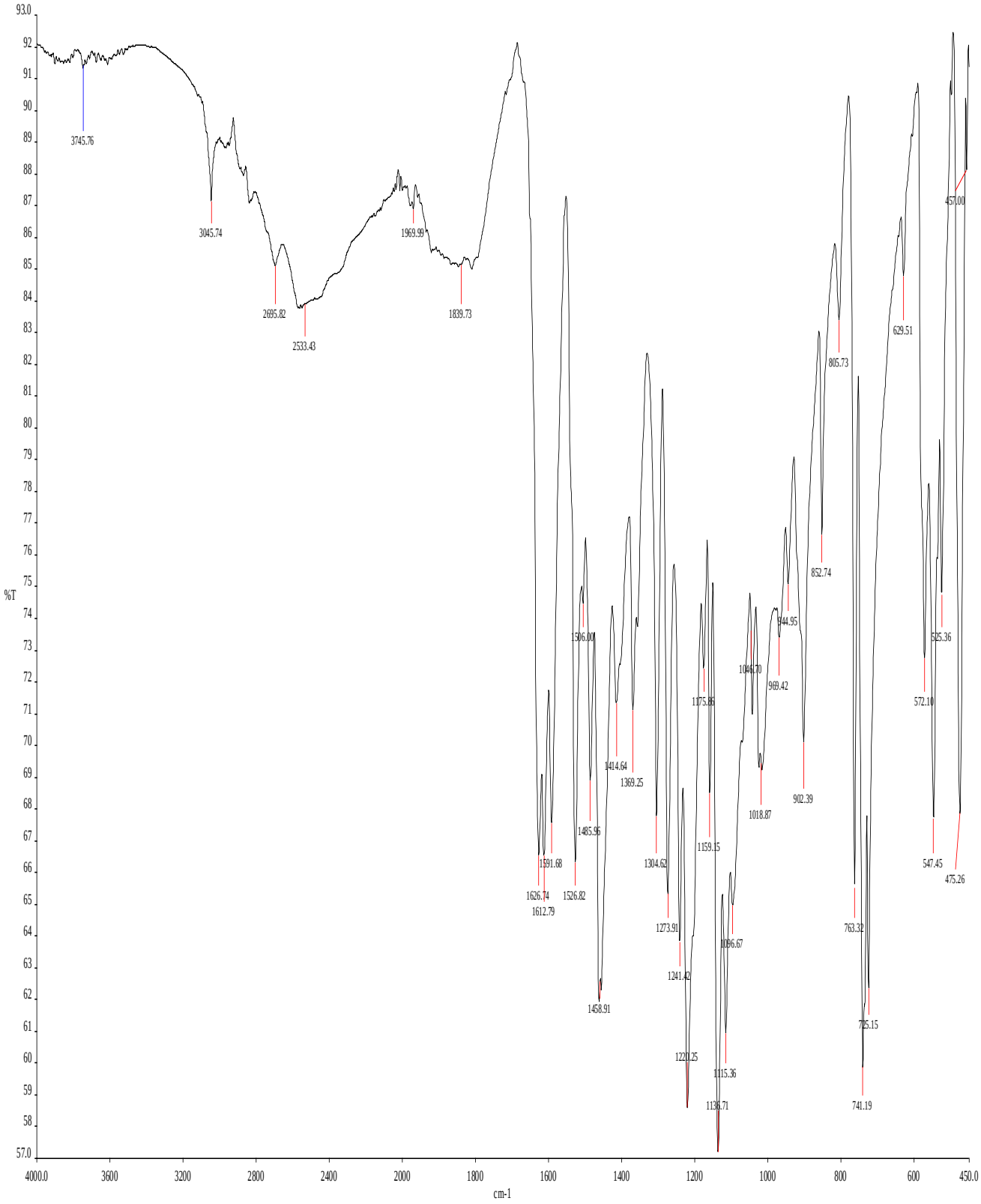

(A)

Eclética Química Journal, vol. 45, n. 1, 2020, 18-43
ISSN: 1678-4618
DOI: 10.26850/1678-4618eqj.v45.1.2020.p18-43

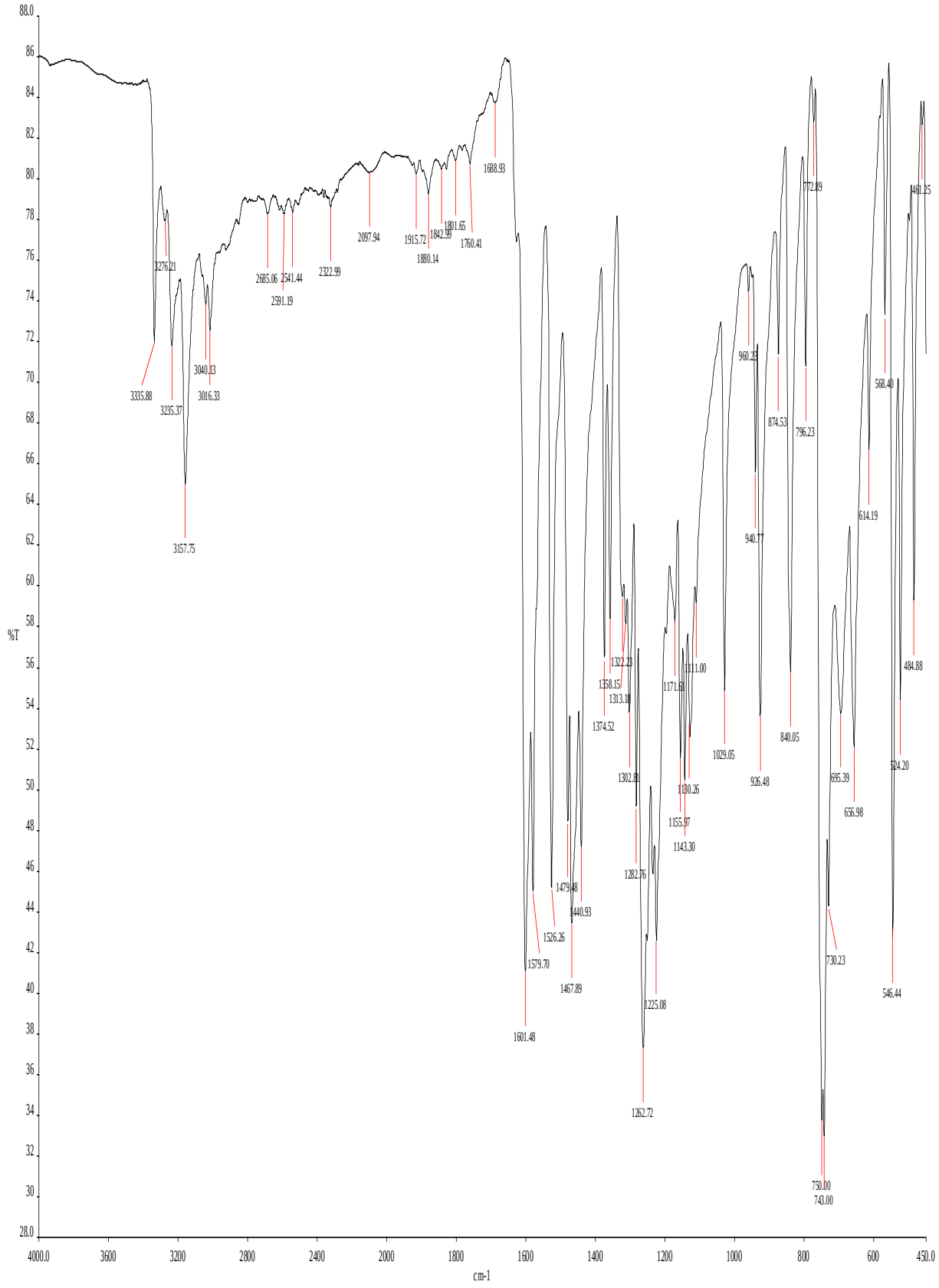

(B)

Figure 1. IR spectra of L_1 (A) and NiL_1NH_3 (B).

Eclética Química Journal, vol. 45, n. 1, 2020, 18-43
ISSN: 1678-4618
DOI: 10.26850/1678-4618eqj.v45.1.2020.p18-43

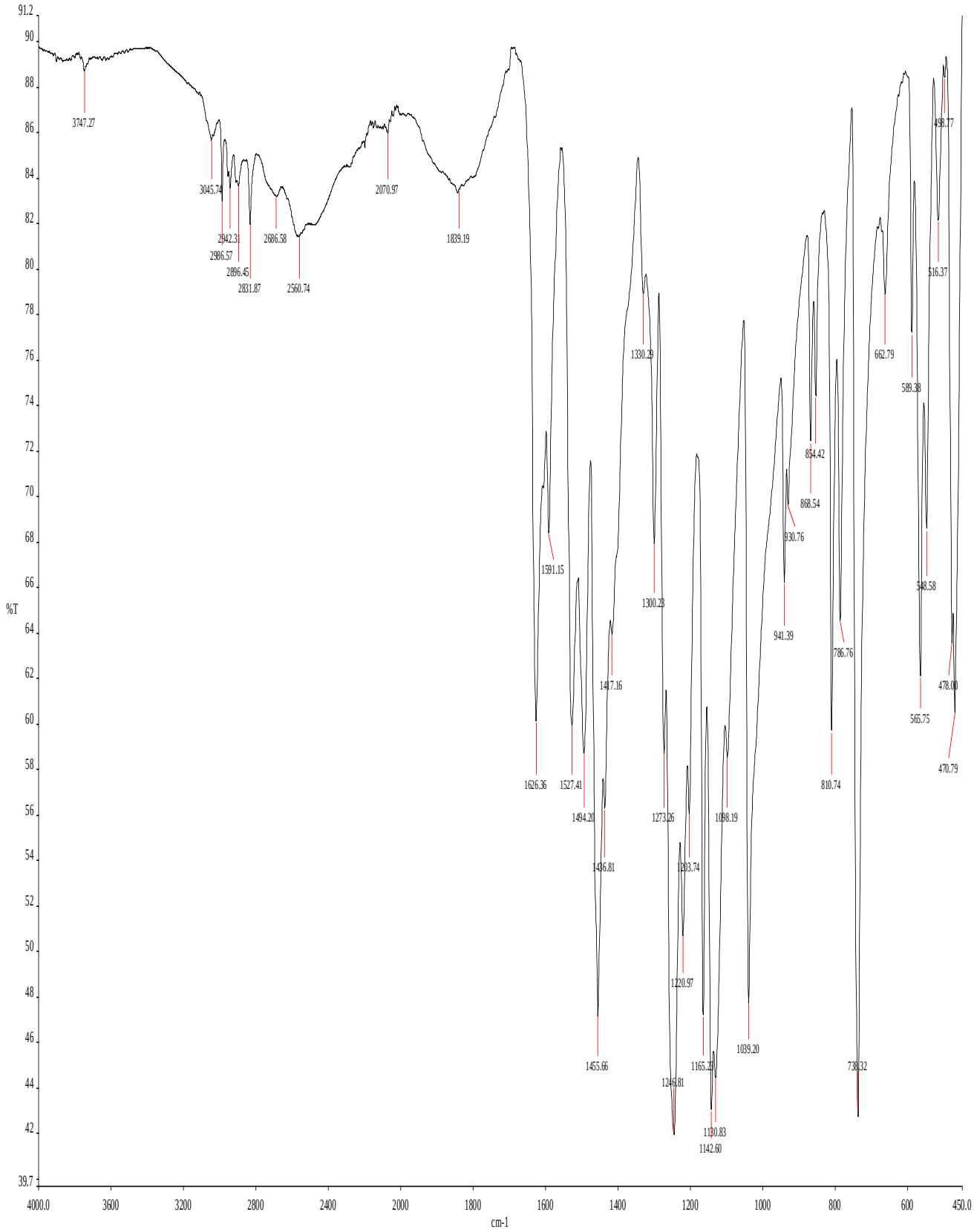

(A)

Eclética Química Journal, vol. 45, n. 1, 2020, 18-43
ISSN: 1678-4618
DOI: 10.26850/1678-4618eqj.v45.1.2020.p18-43

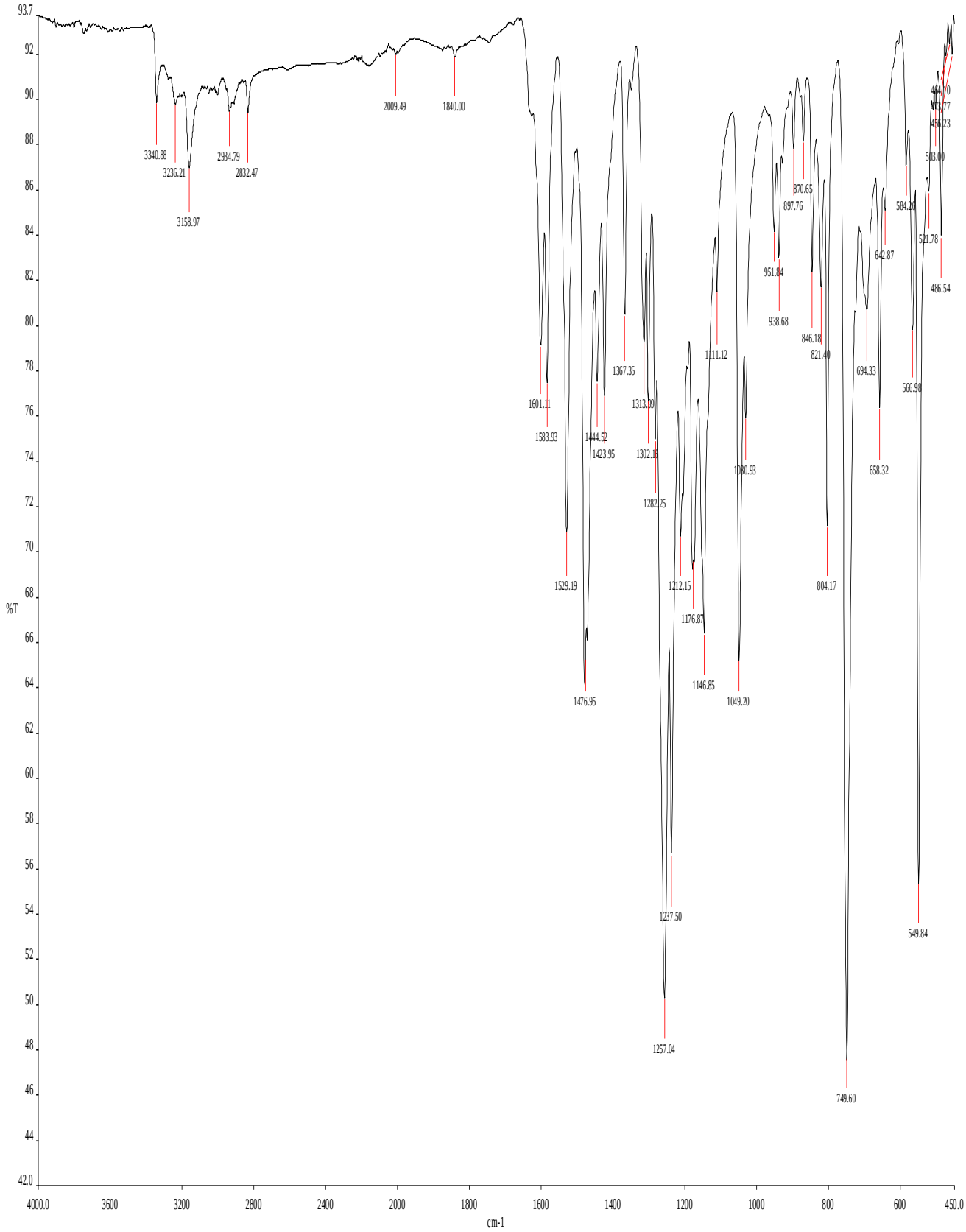

(B)

Figure 2. IR spectra of L_2 (A) and NiL_2NH_3 (B).

Eclética Química Journal, vol. 45, n. 1, 2020, 18-43
ISSN: 1678-4618
DOI: 10.26850/1678-4618eqj.v45.1.2020.p18-43

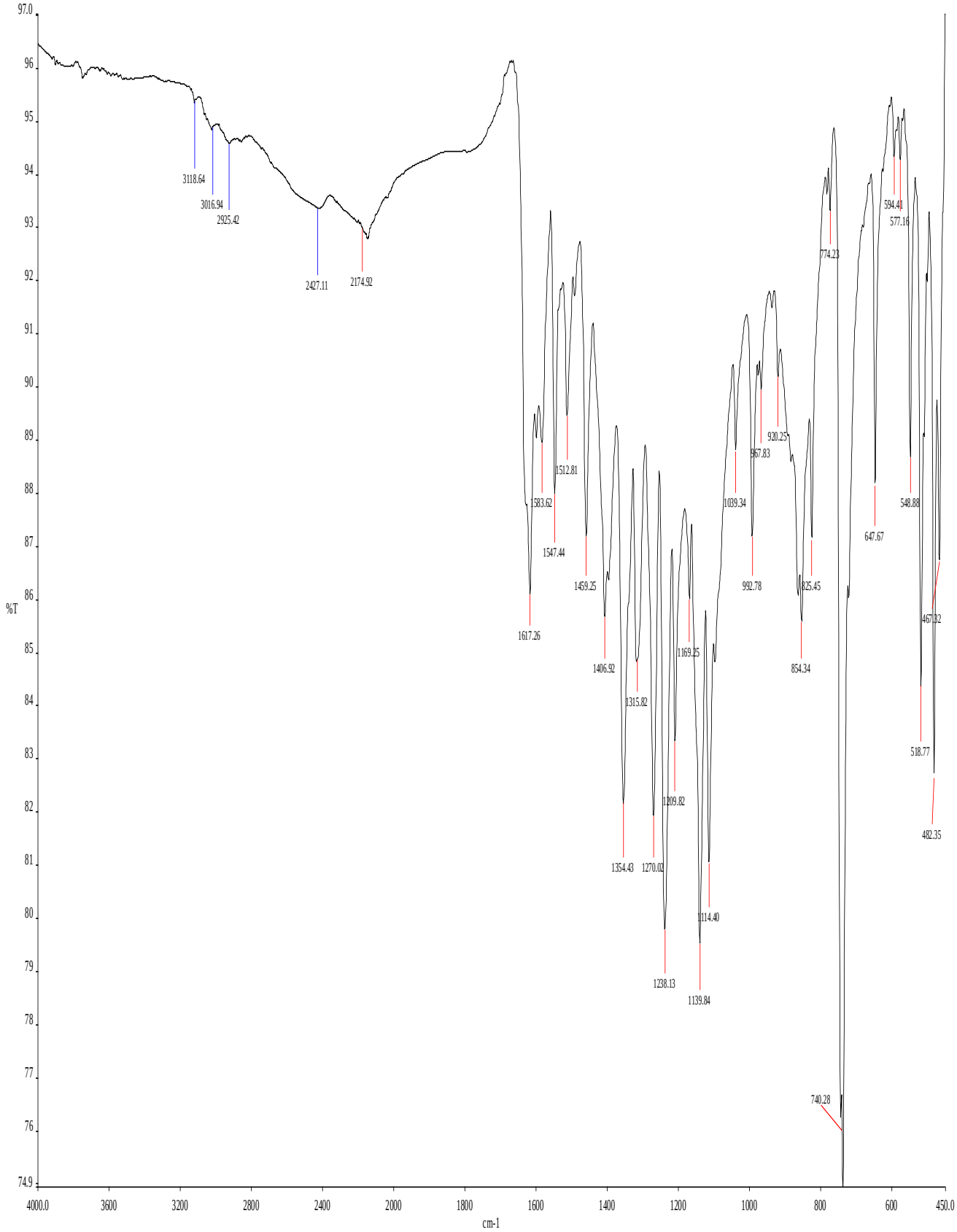

(A)

Eclética Química Journal, vol. 45, n. 1, 2020, 18-43
ISSN: 1678-4618
DOI: 10.26850/1678-4618eqj.v45.1.2020.p18-43

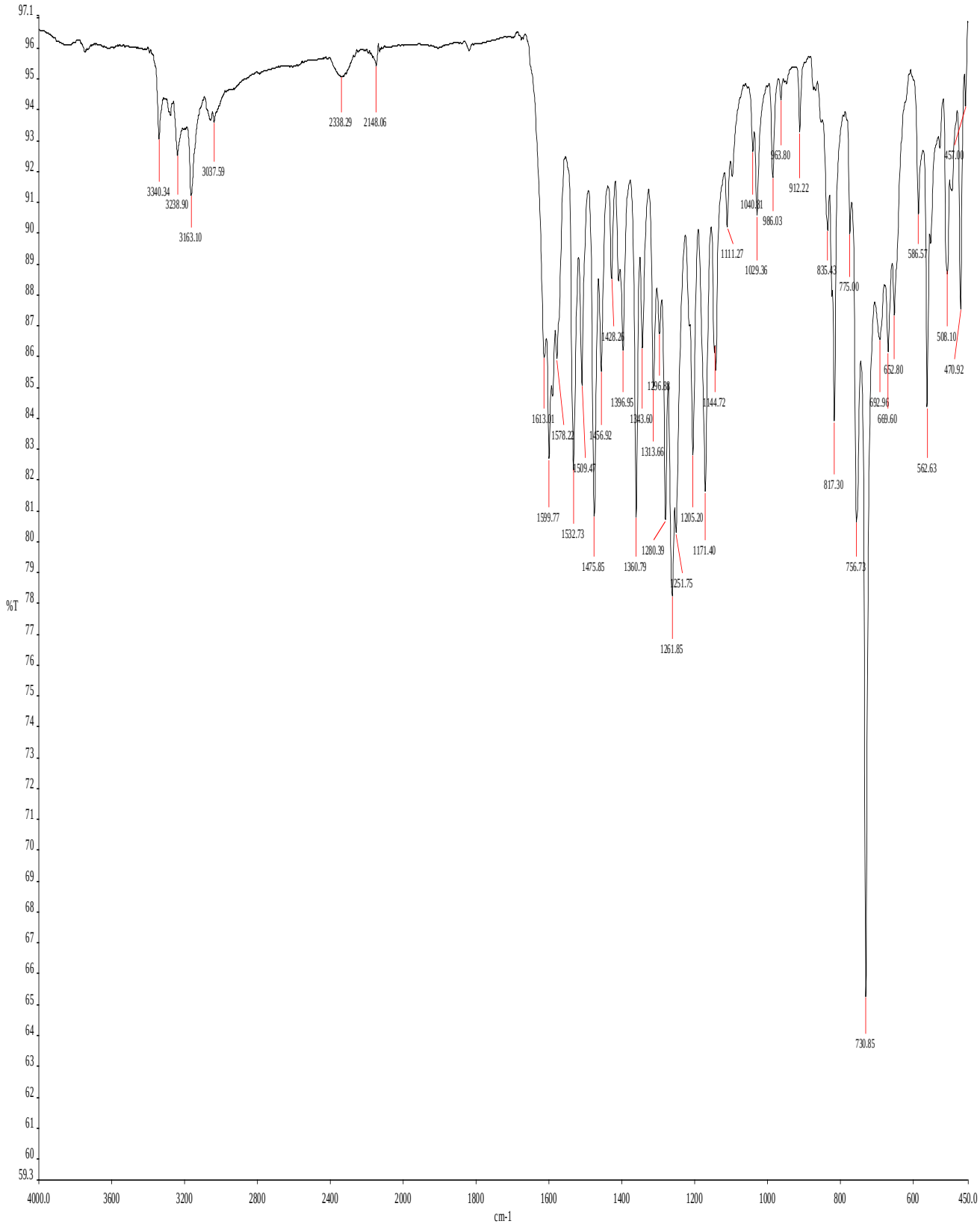

(B)

Figure 3. IR spectra of L_3 (A) and NiL_3NH_3 (B).

Eclética Química Journal, vol. 45, n. 1, 2020, 18-43
ISSN: 1678-4618
DOI: 10.26850/1678-4618eqj.v45.1.2020.p18-43

3.1.2. NMR spectra

The ^{1}H NMR spectra of the free Schiff bases showed two singlet signals at δ 13.78-13.07 and δ 10.31-9.68 ppm which were assigned to the two phenolic –OH protons. The spectra showed singlet signals at δ 8.92 (L_1), 8.89 (L_2) and 9.47 ppm (L_3) attributed to the azomethine (−HC=N) protons. The aromatic protons appeared as multiplets around δ 8.34-6.70 ppm[8,11,27]. The three protons of the methoxy (–OCH_3) groups in 'L_2' appeared as a sharp singlet signal at δ 3.71 ppm[29,30]. A comparison of the ^{1}H NMR spectra of the free Schiff base ligands with the Ni(II) mixed-ligand complexes (Figs. 4-6) showed that the chemical shifts for the –OH protons in the free Schiff bases were not observed in the spectra of the complexes. The absence of the –OH signals indicated the deprotonation of the hydroxyl groups of the Schiff bases prior to coordination with Ni(II) ion. It also confirmed the bonding of oxygen to the Ni(II) ions. Moreover, the coordination of the azomethine nitrogen atoms of the Schiff bases to Ni(II) ion were indicated by the displacements of the chemical shifts of the azomethine hydrogen to upfield region at δ 9.25-8.65 ppm. The aromatic protons appeared as multiplets around δ 8.49-6.30 ppm for the complexes[8,11,27]. The new singlet signals at δ 2.37 and δ 2.25 ppm in the Ni(II) complexes were assigned to the three hydrogen atoms of –NH_3 groups[28]. The appearance of these new singlet signals confirmed the presence of ammonia in the complexes as they are not present in the free Schiff base ligands. Furthermore, the three hydrogen atoms of the new singlet signals in the complexes spectra showed that the complex containing NH_3 is not in the form of ammonium ion (NH_4^+). The three –OCH_3 group protons of 'L_2' in the Ni(II) complex appeared as sharp singlet signals at δ 3.69 ppm[29,31]. Signals at 3.33 ppm and 2.45-2.50 ppm are for H_2O/DMSO and DMSO respectively in all the spectra.

The ^{13}C NMR spectra (Figs. S1-S3, supplementary data) are consistent with the proton NMR of the complexes. The ^{13}C NMR spectrum of NiL_1NH_3 showed a peak at δ 167.43 ppm which confirmed the presence of azomethine carbon in the complex. The aromatic carbons peaks appeared in the range 162.96-114.75 ppm[8,11,27]. In NiL_2NH_3 ^{13}C NMR spectrum, the azomethine carbon appeared at 167.38 ppm and the aromatic carbons peaks appeared in the range 156.48-114.77 ppm while the carbon peak for –OCH_3 group appeared at δ 55.96 ppm[29,30]. NiL_3NH_3 ^{13}C NMR spectrum showed the azomethine carbon peak at 167.17 ppm and the aromatic carbons peaks in the range 163.59-111.70 ppm[17].

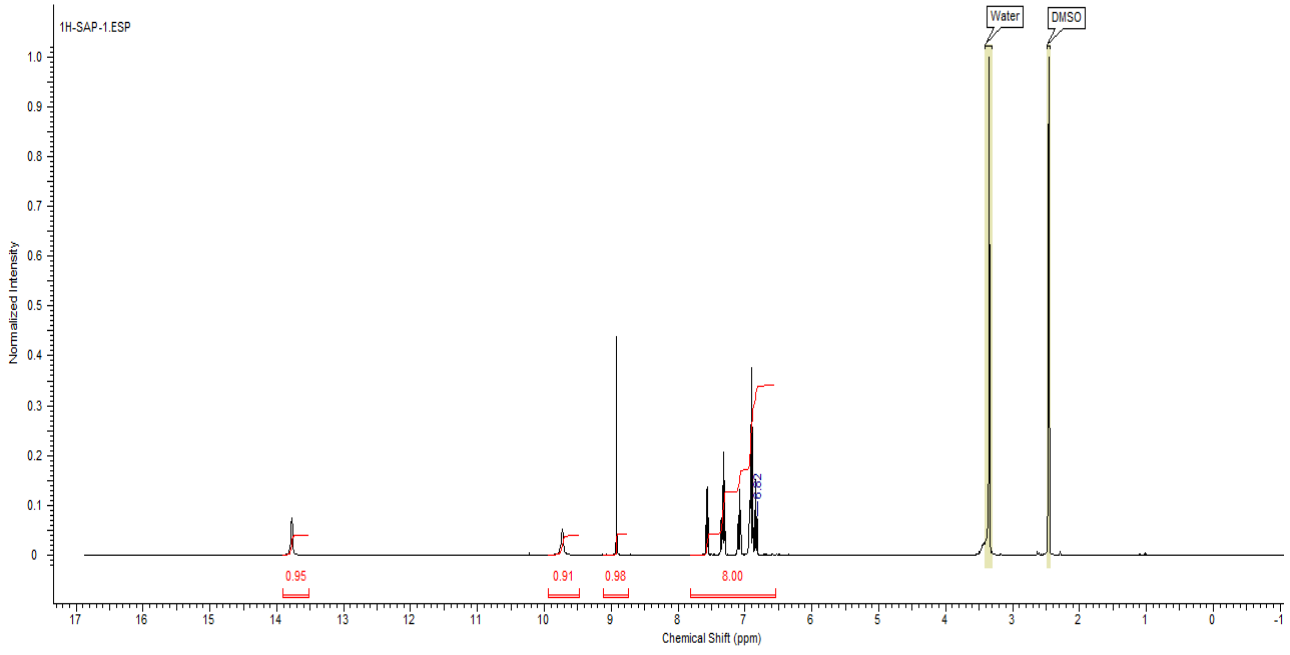

(A)

Eclética Química Journal, vol. 45, n. 1, 2020, 18-43
ISSN: 1678-4618
DOI: 10.26850/1678-4618eqj.v45.1.2020.p18-43

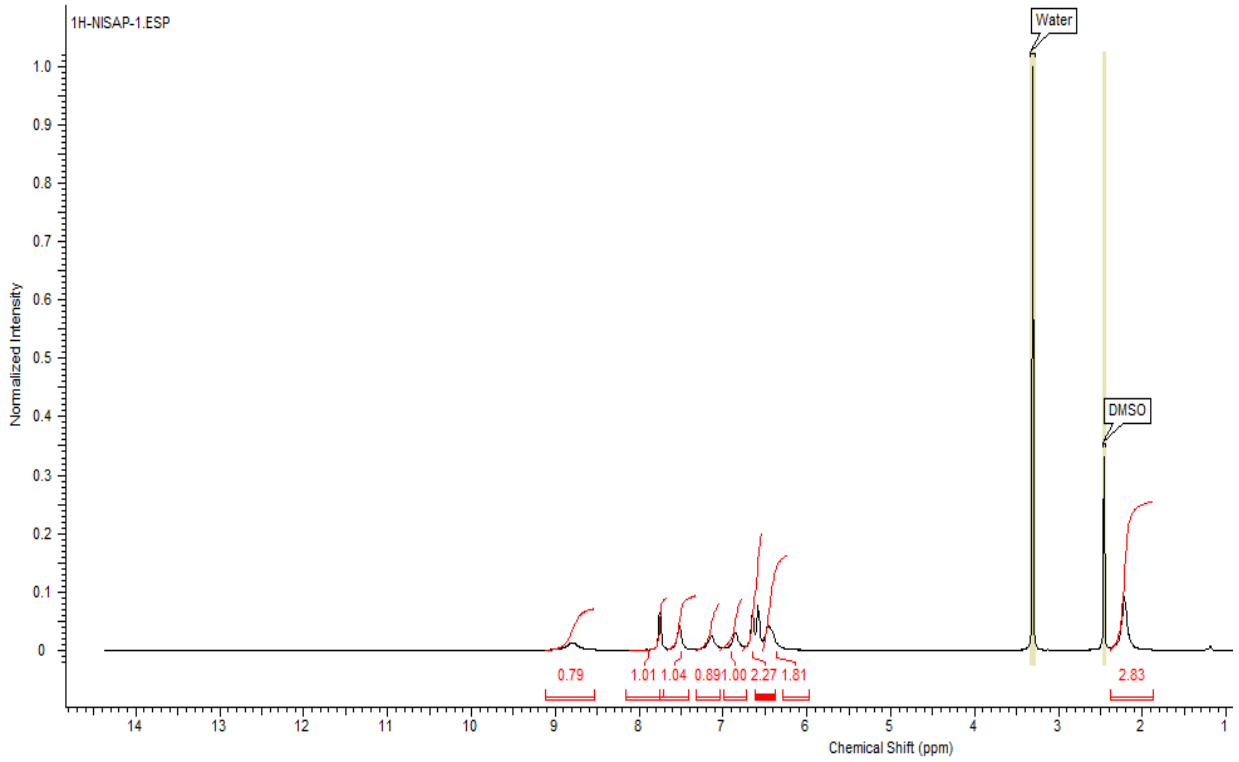

(B)

Figure 4. ^{1}H NMR spectra of L_1 (A), NiL_1NH_3 (B) in water and DMSO.

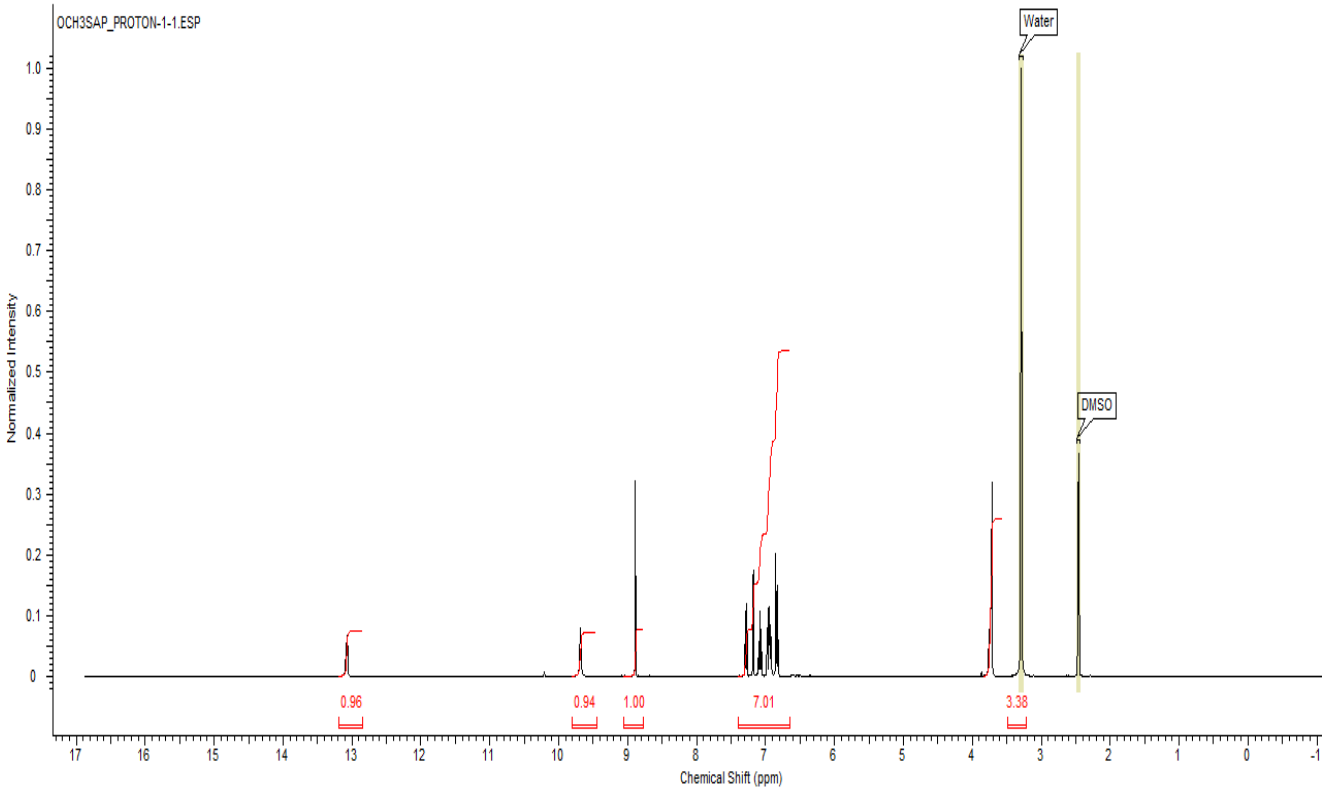

(A)

Eclética Química Journal, vol. 45, n. 1, 2020, 18-43
ISSN: 1678-4618
DOI: 10.26850/1678-4618eqj.v45.1.2020.p18-43

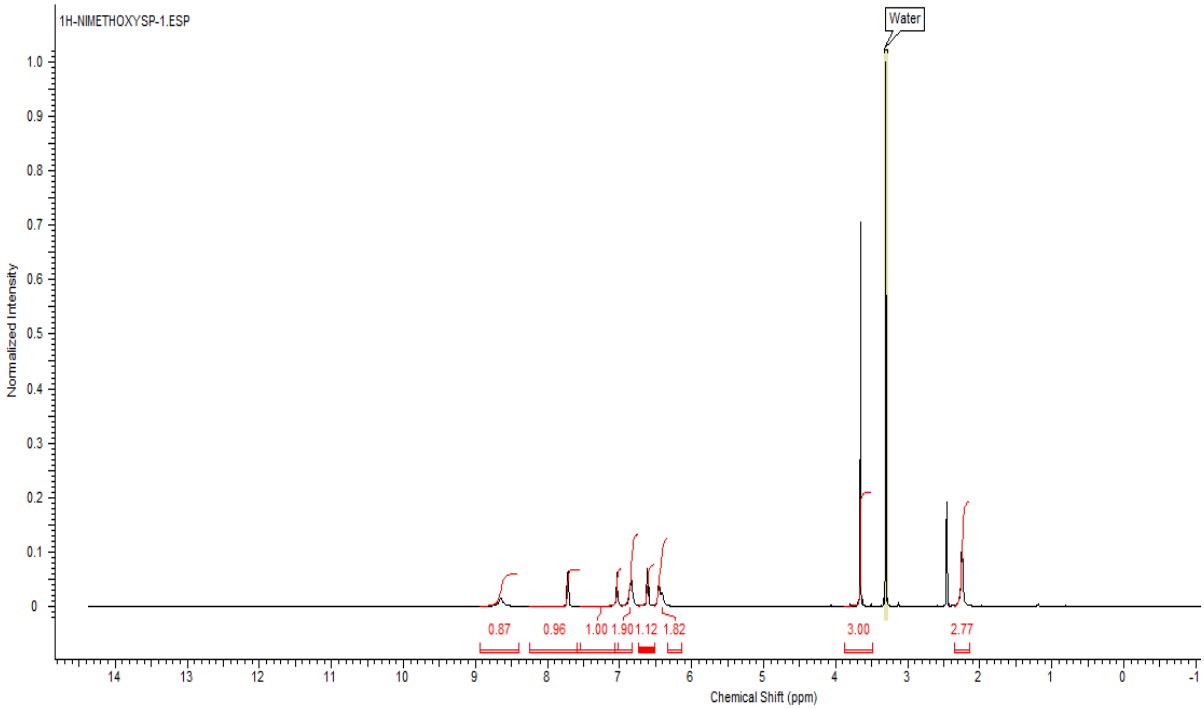

(B)

Figure 5. ^{1}H NMR spectra of L_2 (A), NiL_2NH_3 (B) in water and DMSO.

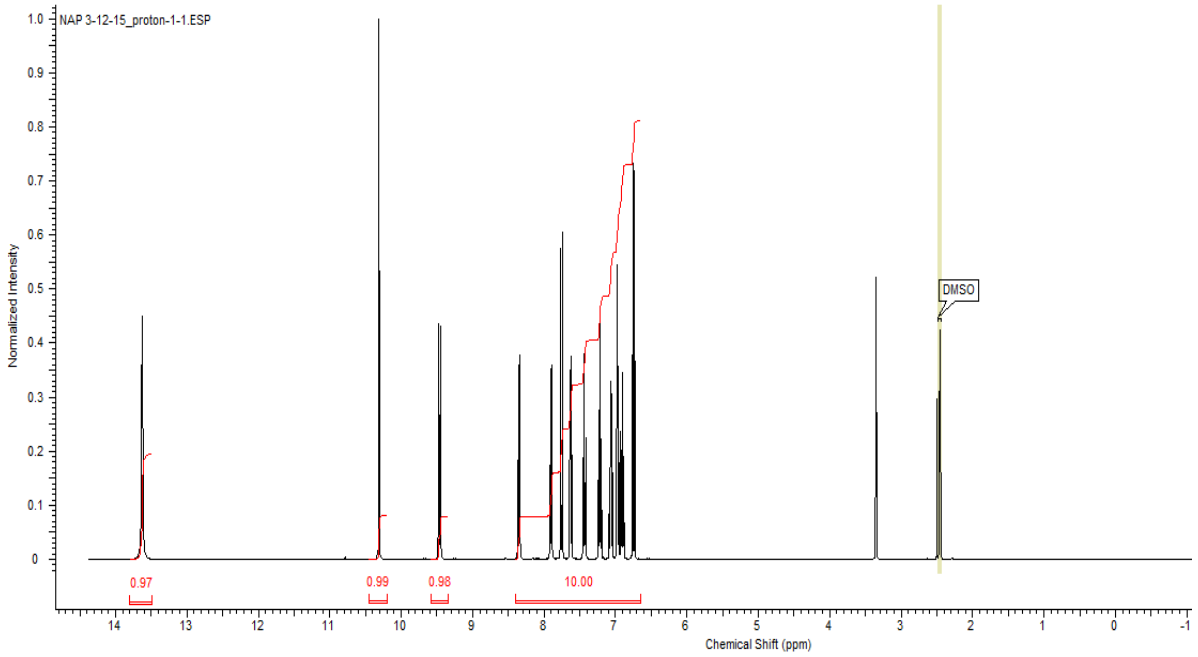

(A)

Eclética Química Journal, vol. 45, n. 1, 2020, 18-43
ISSN: 1678-4618
DOI: 10.26850/1678-4618eqj.v45.1.2020.p18-43

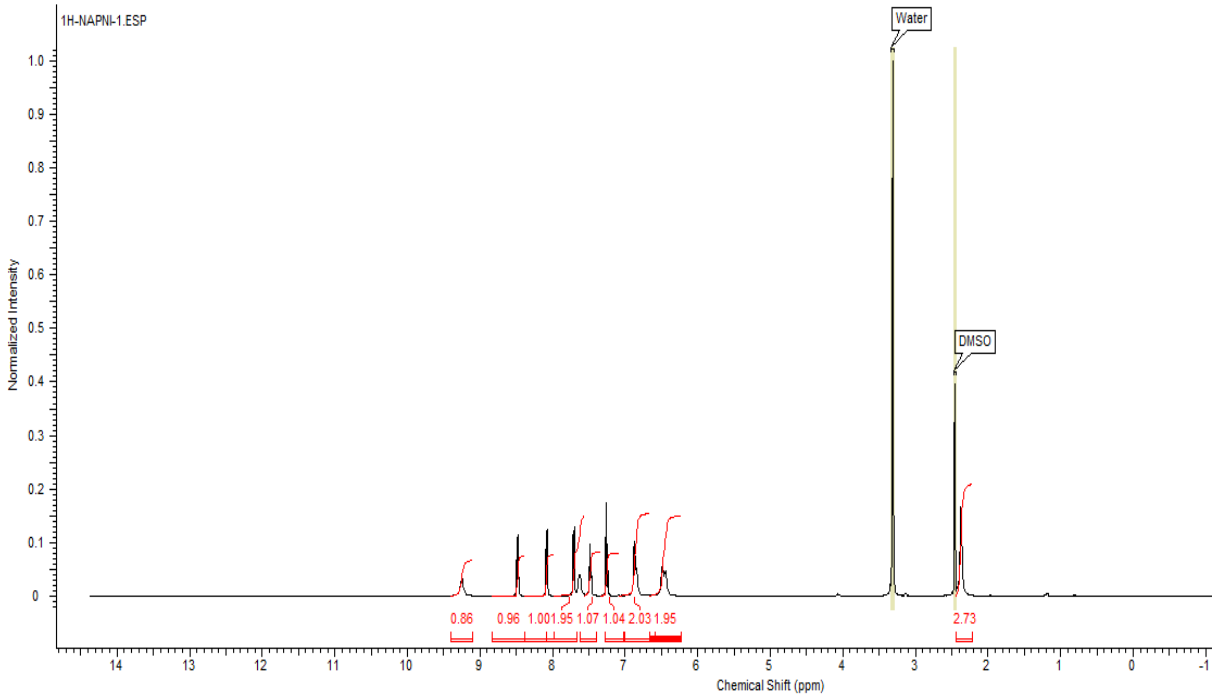

(B)

Figure 6. ^{1}H NMR spectra of L_3 (A) and NiL_3NH_3 (B) in water and DMSO**.**

3.1.3. Electronic spectra

The electronic spectra data of the Schiff bases and the Ni(II) mixed-ligand complexes are presented in Table 1. The spectra were recorded in 1.0×10^{-4} mol L^{-1} DMSO solution in the range 250-900 nm. The spectra of the Schiff bases showed absorption bands around 30769-27027 cm^{-1} and 22279-21186 cm^{-1} which were assigned to $\pi \rightarrow \pi^*$ and $n \rightarrow \pi^*$ transitions respectively[17,29,31]. These transitions were observed in the spectra of the mixed-ligand complexes (Figs. 7-9) but some shifted to longer wavelength, confirming the coordination of the Schiff base ligands to the Ni(II) ion. The electronic spectrum of NiL_1NH_3 displayed two absorption bands at 33113 and 23529 cm^{-1} which were assigned to $\pi \rightarrow \pi^*$ and $^{1}A_{1g} \rightarrow {}^{1}E_{1g}$ transitions respectively[8]. Similarly, NiL_2NH_3 spectrum showed two absorption bands at 32573 and 22779 cm^{-1} assigned to $\pi \rightarrow \pi^*$ and $^{1}A_{1g} \rightarrow {}^{1}E_{1g}$ transitions respectively[30]. However, NiL_3NH_3 showed three absorption bands at 31250, 22472 and 21186 cm^{-1} assigned to $\pi \rightarrow \pi^*$, $^{1}A_{1g} \rightarrow {}^{1}E_{1g}$, $^{1}A_{1g} \rightarrow {}^{1}B_{1g}$ transitions respectively[28]. The absence of any band below 10000 cm^{-1} eliminated the possibility of tetrahedral geometry[8]. Hence, this suggest a square planar geometry.

Eclética Química Journal, vol. 45, n. 1, 2020, 18-43
ISSN: 1678-4618
DOI: 10.26850/1678-4618eqj.v45.1.2020.p18-43

Table 1. Experimental and theoretical electronic spectra data of the compounds.

Compounds	Bands in cm^{-1}	Assignments
L_1	28329	$\pi \rightarrow \pi^*$
NiL_1NH_3 (Exp)	33113, 23529	$\pi \rightarrow \pi^*, {}^1A_{1g} \rightarrow {}^1E_{1g}$,
NiL_1NH_3 (B3LYP)	2317, 22422, 19377	
NiL_1NH_3 (EDF1)	22382, 15290	
L_2	27027	$\pi \rightarrow \pi^*$
NiL_2NH_3 (Exp)	32573, 22779	$\pi \rightarrow \pi^*, {}^1A_{1g} \rightarrow {}^1E_{1g}$,
NiL_2NH_3 (B3LYP)	24724, 23285, 22323, 19239	
NiL_2NH_3 (EDF1)	21685, 14794	
L_3	30769, 22272, 21186	$\pi \rightarrow \pi^*$, $n \rightarrow \pi^*$, $n \rightarrow \pi^*$
NiL_3NH_3 (Exp)	31250, 22472, 21186	$\pi \rightarrow \pi^*$, ${}^1A_{1g} \rightarrow {}^1E_{1g}$, ${}^1A_{1g} \rightarrow {}^1B_{1g}$
NiL_3NH_3 (B3LYP)	25454, 23552, 22339, 19642	
NiL_3NH_3 (EDF1)	22471, 21209, 15095	

Exp = Experimental.

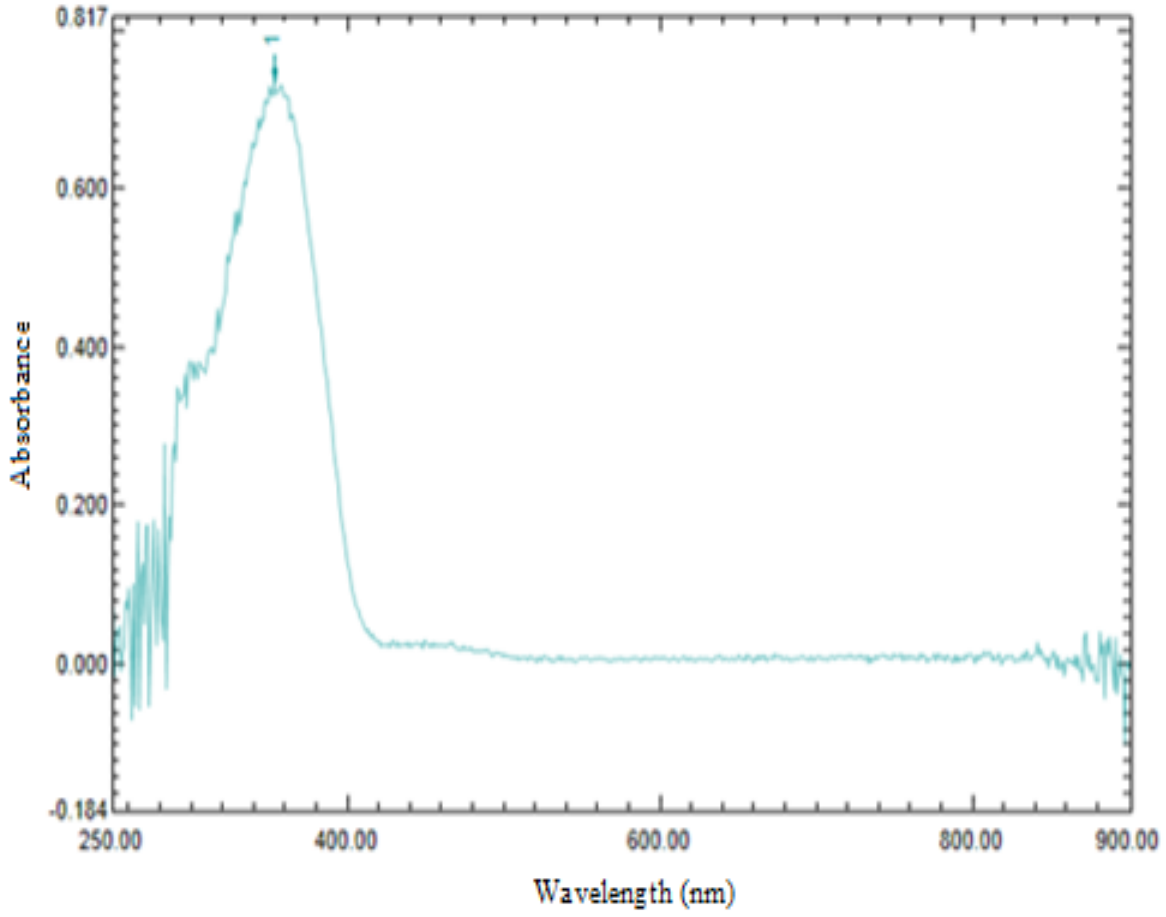

(A)

Eclética Química Journal, vol. 45, n. 1, 2020, 18-43
ISSN: 1678-4618
DOI: 10.26850/1678-4618eqj.v45.1.2020.p18-43

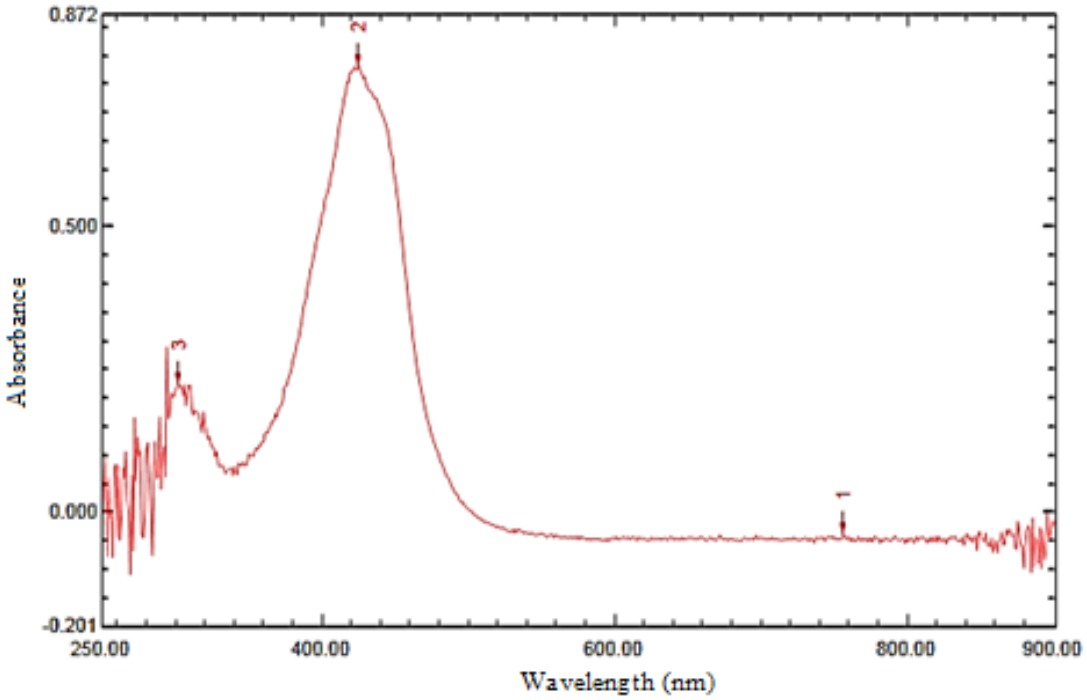

(B)

Figure 7. UV-Visible spectra of L_1 (A), NiL_1NH_3 (B)**.**

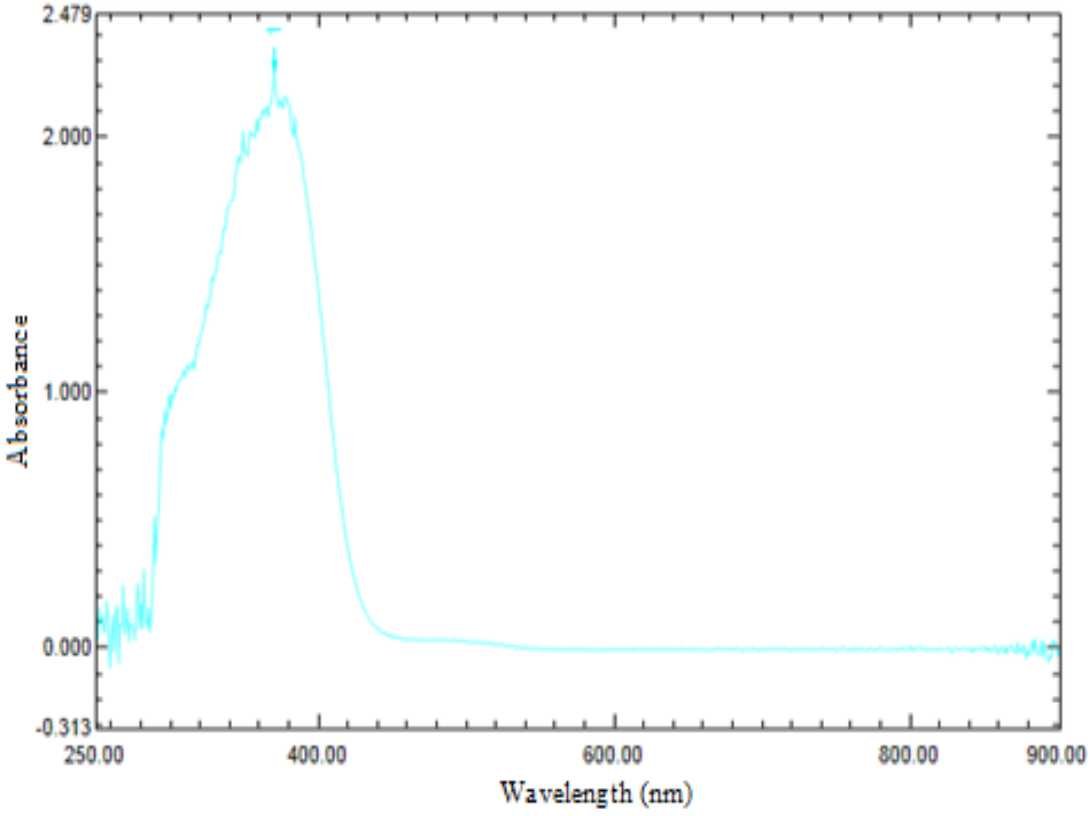

(A)

Eclética Química Journal, vol. 45, n. 1, 2020, 18-43
ISSN: 1678-4618
DOI: 10.26850/1678-4618eqj.v45.1.2020.p18-43

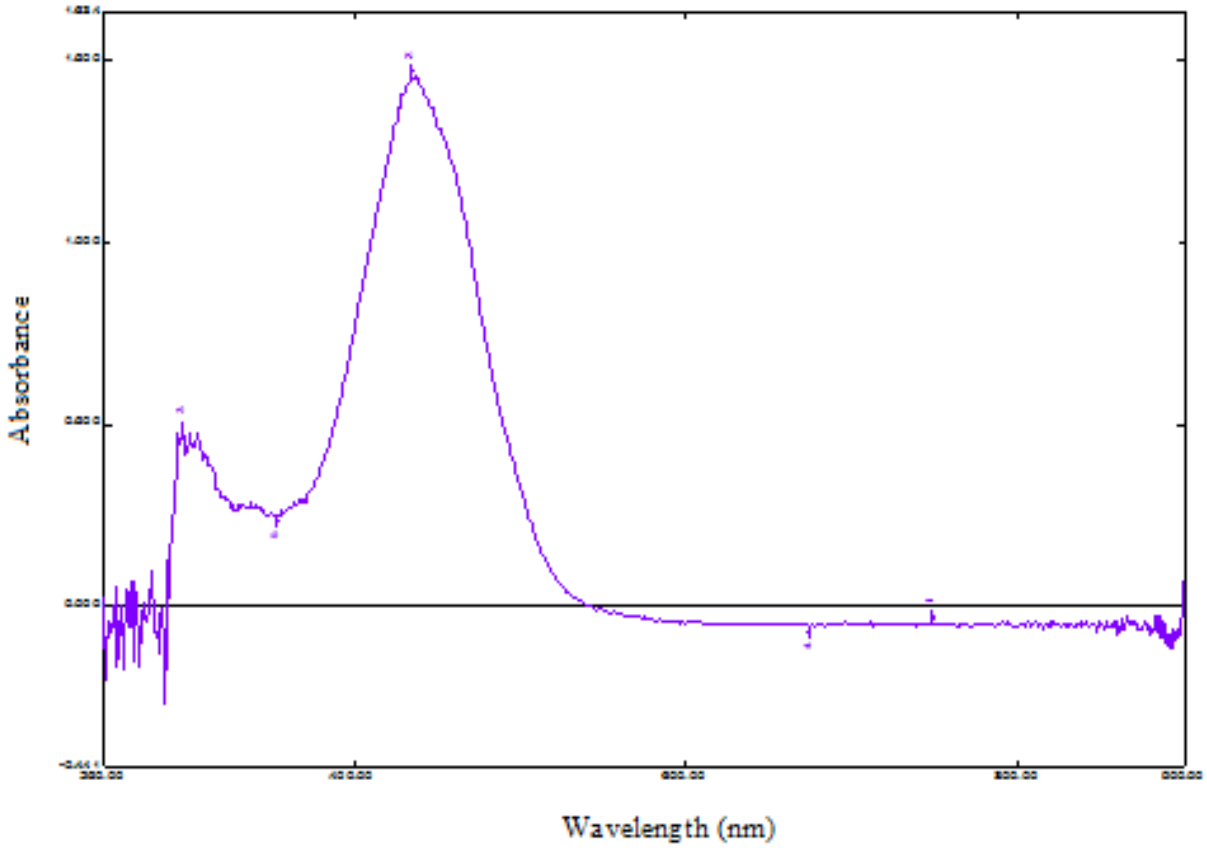

(B)

Figure 8. UV-Visible spectra of L_2 (A), NiL_2NH_3 (B).

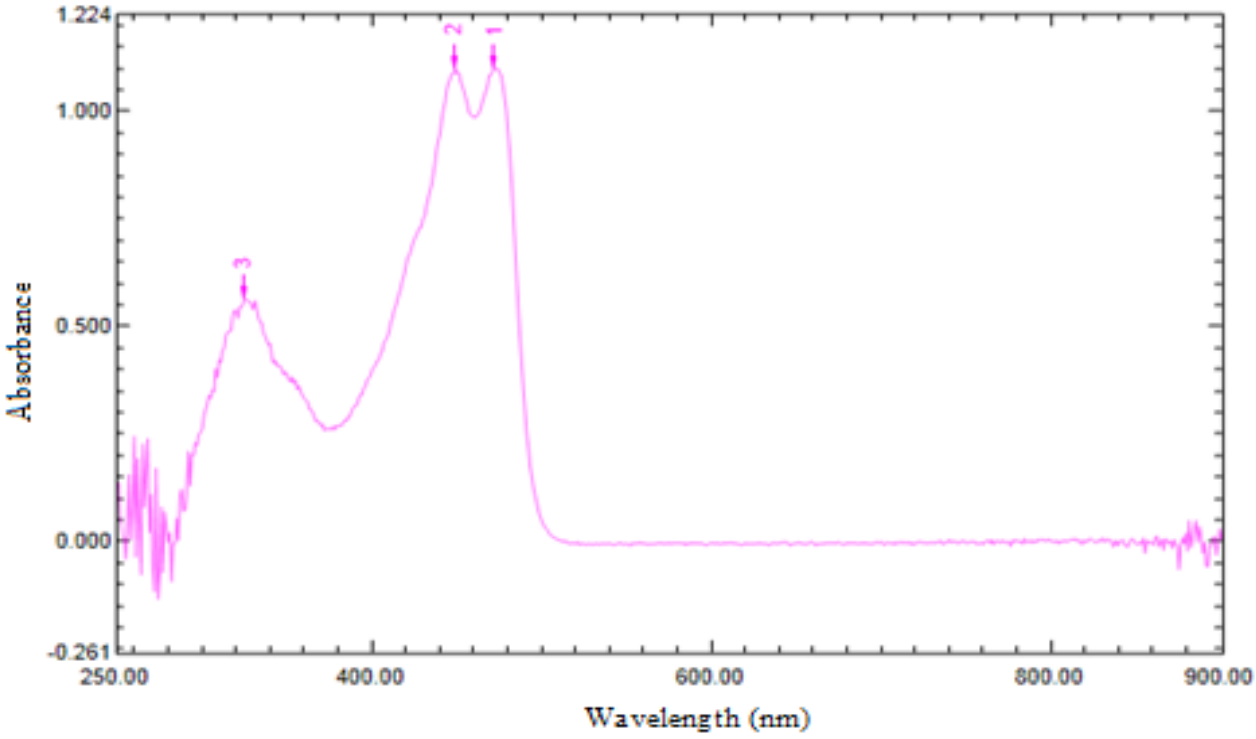

(A)

Eclética Química Journal, vol. 45, n. 1, 2020, 18-43
ISSN: 1678-4618
DOI: 10.26850/1678-4618eqj.v45.1.2020.p18-43

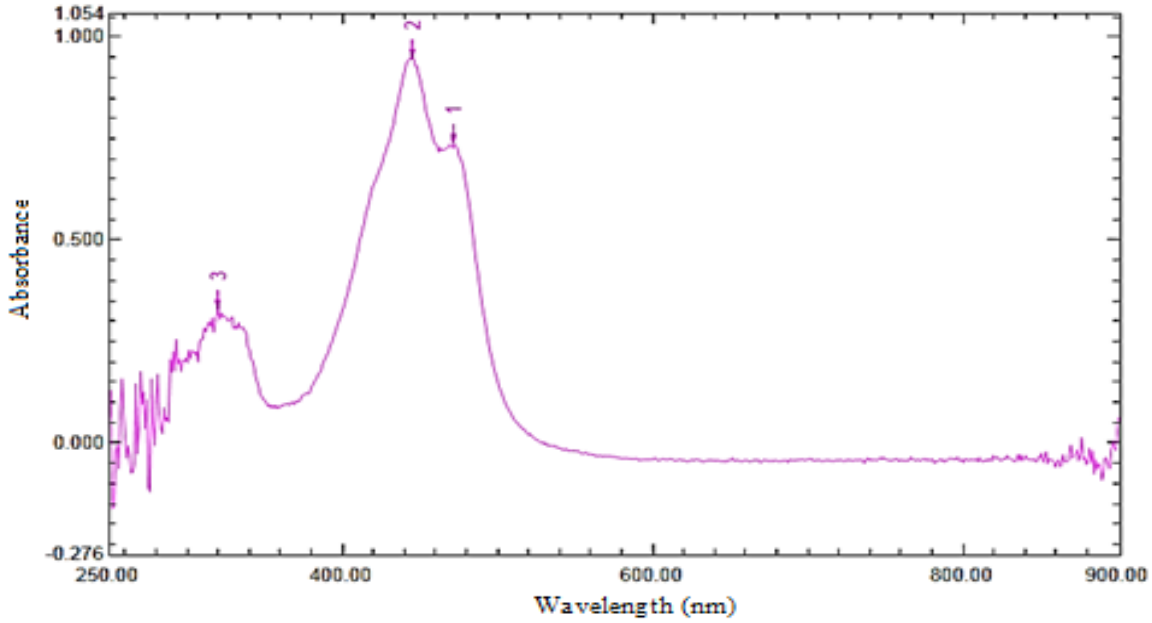

(B)

Figure 9. UV-Visible spectra of L_3 (A), NiL_3NH_3 (B)

3.1.4 Theoretical IR spectra

The theoretical IR vibrational frequency values of the Ni(II) complexes (Table 2) are in good agreement with the experimental values. The azomethine (−HC=N) absorption bands of the complexes appeared at 1654 cm^{-1} for both NiL_1NH_3 and NiL_2NH_3 while NiL_3NH_3 was at 1648 cm^{-1} at B3LYP/6-31G** level. Experimentally, these bands were observed at 1601 and 1600 cm^{-1} for the complexes. The phenolic C−O stretching vibrations of the complexes appeared around 1340-1334 cm^{-1} in the theoretical data while the experimental values were observed around 1301-1261 cm^{-1}. The experimental ν(N−H) stretching vibrations of $-NH_3$ groups in the complexes appeared around 3336-3340 cm^{-1} while it was observed at 3592-3466 cm^{-1} in the theoretical spectra. The aromatic ν(C−H) stretching frequencies in the complexes were observed at 3218-3062 cm^{-1} in the theoretical data while the experimental were 3259-3010 cm^{-1}. The characteristic ν(C=C) ring stretching vibrations of the complexes appeared at 1639-1400 cm^{-1} in the theoretical data, these bands appeared around 1584-1400 cm^{-1} in the experimental spectra. The ν(Ni−O) and ν(Ni−N) in the complexes were observed at 531-465 and 579-531 cm^{-1} in the theoretical spectra. These bands were observed at 485-471 and 550-508 cm^{-1} in the experimentally.

Table 2. Some selected theoretical IR data of the complexes.

IR bands / cm^{-1}	NiL_1NH_3	NiL_2NH_3	NiL_3NH_3
ν(N−H) (B3LYP) (EDF1)	3592-3463 3539-3408	3596-3467 3536-3403	3597-3466 3542-3407
ν(C−H) (B3LYP) (EDF1)	3212-3174 3171-3122	3200-3062 3182-3024	3218-3174 3176-3135
ν(C=N) (B3LYP) (EDF1)	1654 1608	1654 1591	1648 1615
ν(N−H) bending (B3LYP) (EDF1)	1662-1665 1640-1622	1680-1658 1636-1633	1670-1657 1639-1417
ν(C=C) (B3LYP) (EDF1)	1639-1404 1593-1452	1639-1413 1608-1429	1633-1400 1606-1417
ν(C−O) (B3LYP) (EDF1)	1340 1313	1339 1312	1334 1308
ν(C−H) bending (B3LYP) (EDF1)	891-666 889-666	871-663 894-669	886-666 895-650
ν(Ni−O) (B3LYP) (EDF1)	500 499	465 458	531 525
ν(Ni−N) (B3LYP) (EDF1)	538 532	531 525	579 566

Eclética Química Journal, vol. 45, n. 1, 2020, 18-43
ISSN: 1678-4618
DOI: 10.26850/1678-4618eqj.v45.1.2020.p18-43

3.1.5 Theoretical NMR spectra

The theoretical chemical shift values of the Ni(II) mixed-ligand complexes (Table 3) are in good agreement with the experimental values. The data obtained at B3LYP/6-31G** level showed the aromatic hydrogen in NiL_1NH_3: H17, H15, H14, H2, H11, H10, H6, H13 at 8.65, 7.94, 7.84, 7.66, 8.12, 7.57, 8.26, 7.53 ppm respectively. These were experimentally observed around 7.75-6.46 ppm. The azomethine (−HC=N) hydrogen and the three hydrogen in the $-NH_3$ group were observed at 10.07 and 2.60 ppm respectively in the theoretical spectra while they appeared at 8.79 and 2.37 ppm respectively in the experimental spectra. The aromatic carbon in the complex appeared in the range 157.40-108.56 ppm, these were observed experimentally in the range 162.96-114.75 ppm. The azomethine carbon signal appeared at 158.82 ppm in the theoretical calculations while it was experimentally observed at 167.43 ppm. Moreover, the aromatic hydrogen in NiL_2NH_3: H10, H13, H15, H17, H17, H14, H11, H6 were observed at 7.54, 7.51, 7.94, 8.64, 7.77, 7.62, 7.79 ppm in the theoretical spectra, these appeared in the range 7.71-6.45 ppm in the experimental study. The azomethine (−HC=N) hydrogen and the three hydrogen in the $-NH_3$ group appeared at 10.04 and 2.52 ppm respectively in the theoretical calculations while they were experimentally observed at 8.79 and 2.37 ppm respectively.

Table 3. Theoretical electronic spectra data of the complexes.

Positions of H & C	NiL_1NH_3 δ/ppm		NiL_2NH_3 δ/ppm		NiL_3NH_3 δ/ppm	
	B3LYP	EDF1	B3LYP	EDF1	B3LYP	EDF1
H1	2.60	-	2.52	3.07	8.33	8.45
C1	110.41	110.00	142.89	142.19	159.97	154.38
H2	7.66	7.84	4.63	4.84	8.58	8.65
C2	128.54	124.18	114.54	110.42	122.05	119.41
H3	2.60	-	2.52	3.07	9.26	9.37
C3	118.64	118.12	118.90	118.54	114.40	113.33
H4	10.07	9.86	10.04	9.86	2.59	3.09
C4	157.28	151.07	153.62	146.22	130.06	126.45
H5	2.60	-	2.52	3.07	8.80	8.91
C5	118.28	115.09	118.31	114.74	122.42	120.96
H6	8.26	8.38	7.79	7.91	8.50	8.68
C6	125.78	121.47	110.01	106.15	124.73	122.36
H7	-	-	4.63	4.84	11.19	10.97
C7	158.82	154.81	158.06	154.83	111.41	112.29
H8	-	-	4.63	4.84	-	-
C8	135.68	135.74	136.22	135.30	157.97	151.16
H9	-	-	-	-	7.96	8.14
C9	157.40	151.11	153.79	152.81	120.44	117.30
H10	7.57	7.83	7.54	7.84	8.40	8.45
C10	114.37	111.90	114.13	111.99	127.66	123.08
H11	8.12	8.20	7.62	7.70	761	7.88
C11	123.14	119.75	123.07	119.78	138.83	127.20
H12	-	-	-	-	7.60	8.14
C12	108.56	107.84	108.64	107.86	136.45	132.60
H13	7.53	7.71	7.51	7.72	7.97	8.14
C13	107.72	107.49	108.84	107.59	122.57	119.63
H14	7.84	8.03	7.77	7.95	2.59	3.09
C14	-	-	52.28	54.69	108.43	107.31
H15	7.94	8.09	7.94	8.09	-	-
C15	-	-	-	-	155.97	152.23
H16	-	-	-	-	-	-
C16	-	-	-	-	114.05	111.92
H17	8.65	8.72	8.64	7.70	-	-
C17	-	-	-	-	108.83	112.29
H18	-	-	-	-	2.59	3.09
C18	-	-	-	-	-	-

Eclética Química Journal, vol. 45, n. 1, 2020, 18-43
ISSN: 1678-4618
DOI: 10.26850/1678-4618eqj.v45.1.2020.p18-43

The chemical shift of the three hydrogen in the $-OCH_3$ group appeared at 4.63 ppm in the theoretical calculations and at 3.69 ppm in the experimental spectra. The aromatic carbon in the complex appeared in the range 153.79-108.64 ppm in the theoretical spectra, these were observed experimentally in the range 156.48-114.77 ppm. The carbon in the azomethine and $-OCH_3$ groups appeared at 158.06 and 52.28 ppm respectively in the theoretical calculations, these were experimentally observed at 167.38 and 55.96 ppm respectively.

However, in NiL_3NH_3, the hydrogen in the ring: H2, H9, H10, H6, H1, H3, H5, H11, H13, H12 were observed at 8.58, 7.96, 8.40, 8.50, 8.33, 9.26, 8.80, 7.61, 7.97, 7.60 ppm in the theoretical calculations. These were experimentally reported in the range 8.49-6.30 ppm. The azomethine (−HC=N) and $-NH_3$ group hydrogen were observed at 11.19 and 2.59 ppm respectively in the theoretical spectra while they were reported in the experimental study at 9.25 and 2.37 ppm respectively. The aromatic carbon in the complex appeared in the range 157.40-108.56 ppm in the theoretical data, these appeared experimentally in the range 162.96-114.75 ppm. The azomethine carbon was observed at 159.97 ppm in the theoretical data and at 167.17 ppm in the experimental spectra.

3.1.6 Theoretical UV-Vis spectra

Table 1 compared the experimental and theoretical electronic spectra of the complexes. The theoretical electronic spectra data agree with the experimental values. The agreement between the theoretical and experimental electronic spectra data corroborated the suggested structures. The theoretical spectra of NiL_1NH_3 as calculated at B3LYP/6-31G level showed three absorption bands at 23817, 224222, 19377 cm^{-1}. These bands were obtained when electrons were promoted from HOMO → LUMO, HOMO-6 → LUMO and HOMO-2 → LUMO+1 respectively. NiL_2NH_3 showed four absorption bands at 24724, 23285, 22323, 19239 cm^{-1}, these bands were related to the promotion of electrons from HOMO → LUMO, HOMO-1→ LUMO, HOMO-6 → LUMO+1, HOMO-2 → LUMO+1 respectively. Similarly, NiL_3NH_3 displayed four absorption bands at 25454, 23552, 22339, 19642 cm^{-1}. These bands were obtained when electrons were promoted from HOMO-1 → LUMO, HOMO → LUMO, HOMO-7 → LUMO+1 and HOMO-2 → LUMO+1 respectively.

3.2. Geometry of the Ni(II) mixed-ligand complexes

In the absence of available X-ray crystallographic data, the use of quantum chemical methods in determining the equilibrium geometries of the mixed-ligand complexes becomes an important tool. The B3LYP/6-31G** and EDF1/6-31G** methods were used to predict the geometries of the Ni(II) mixed-ligand complexes. The experimental and theoretical observations earlier discussed have confirmed the formation of the mixed-ligand complexes. Hence, the proposed and optimized structures of the mixed-ligand complexes are shown in Fig. 10. The geometry of the mixed-ligand complexes predicted by both methods of calculation was a distorted square planar. The angles N1−Ni1−N2, O1−Ni1−O2, N1−Ni1−O2, N1−Ni1−O1, N2−Ni1−O2, N2−Ni1−O1 (Table S1, supplementary data) indicated that the coordination geometry of the nickel atom is distorted from a square planar. The bond distances Ni1−N1, Ni1−N2, Ni1−O1, Ni1−O2 (Table S1, supplementary data) were in the ranges observed for the analogous compounds of nickel square planar complexes containing the tridentate Schiff bases and N-donor co-ligands[11,28,29].

In NiL_1NH_3, the HOMO which represents π-electrons of the system spread over the Ni(II) ion and N-(salicylidene)-*o*-aminophenol ligand with most of the electron density concentrated on the *o*-aminophenol subunit while the LUMO have most of the electron density concentrated on the salicylidene subunit. Similarly in NiL_2NH_3, the HOMO spread over the Ni(II) ion and N-(5-methoxysalicylidene)-*o*-aminophenol ligand with most of the electron density concentrated on the 5-methoxysalicylidene subunit while the LUMO have most of the electron density concentrated on the salicylidene subunit excluding the methoxy group. In NiL_3NH_3, the HOMO spread over the Ni(II) ion and N-(naphthalidene)-*o*-aminophenol with most of the electron density concentrated on the azomethine group and *o*-aminophenol subunit while the LUMO have most of the electron density concentrated on one of the benzene ring of the naphthalidene and the azomethine group.

Eclética Química Journal, vol. 45, n. 1, 2020, 18-43
ISSN: 1678-4618
DOI: 10.26850/1678-4618eqj.v45.1.2020.p18-43

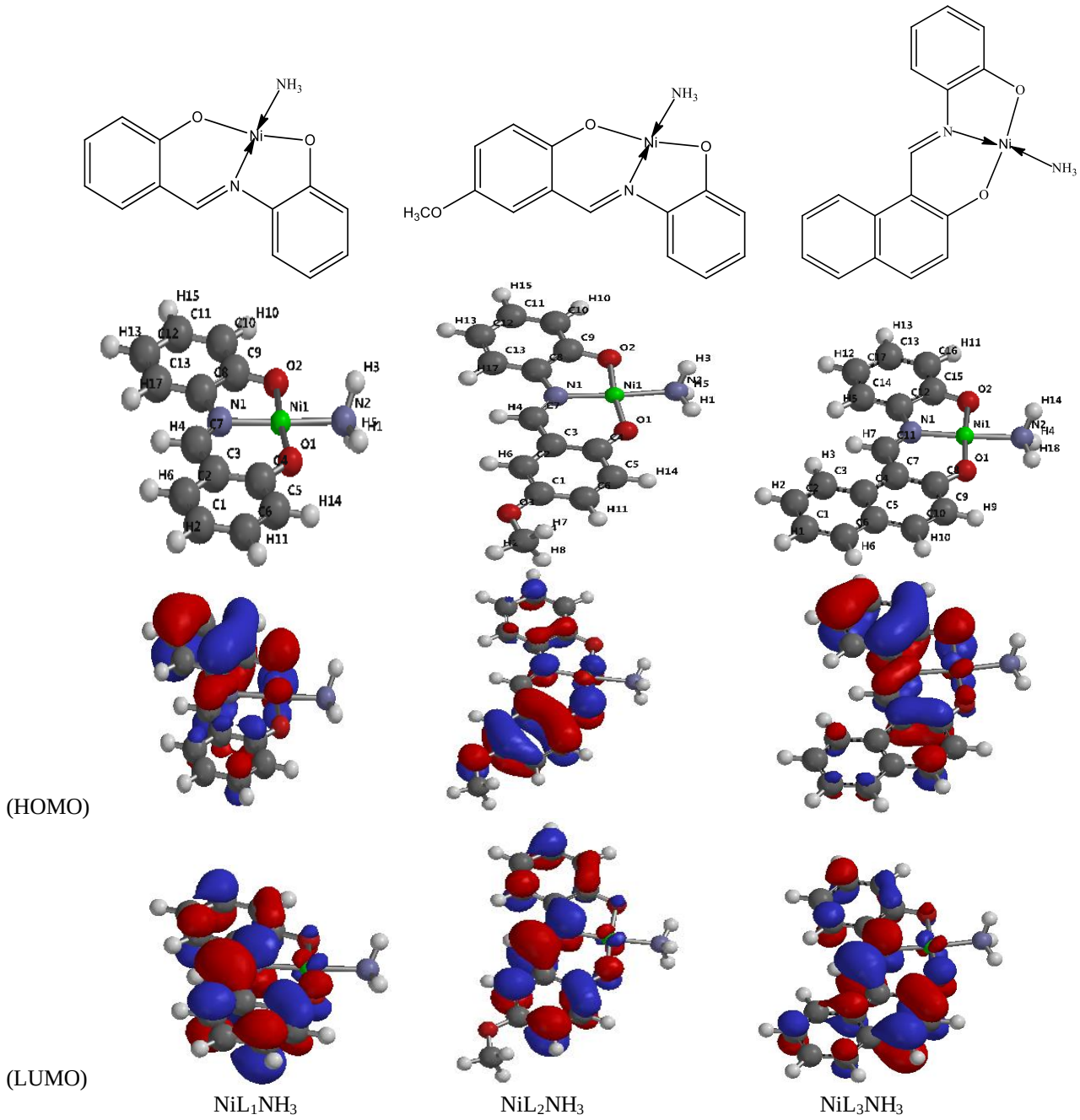

Figure. 10. Proposed and optimized structures of the complexes at B3LYP/6-31G** level.

3.3. Antibacterial activity

The results of the antibacterial activities of the Schiff bases and the mixed-ligand complexes are summarized in Table 4. The antibacterial results revealed that all the synthesized Schiff base ligands and the mixed-ligand complexes exhibited antibacterial activities. The mixed-ligand complexes exhibited better inhibitory effects compared to the parent Schiff bases. The enhancement in the antibacterial activities of the complexes can be explained based on chelation theory and probably the presence of ammonia molecules in the complexes. Chelation makes the ligands more powerful and potent bactericidal agents; consequently, killing more bacteria than the free ligands. It facilitates the ability of the complexes to cross the cell membrane. On chelation, the polarity of the metal ion reduces to a greater extent due to the overlap of the ligand orbital and partial sharing of the positive charge of the metal ion with donor groups. This process thus

Eclética Química Journal, vol. 45, n. 1, 2020, 18-43
ISSN: 1678-4618
DOI: 10.26850/1678-4618eqj.v45.1.2020.p18-43

increases the lipophilic nature of the compound which in turn favors penetration through the cell wall of the bacteria. These complexes also disturb the respiration process of the cell and thus block the synthesis of proteins, which restricts further growth of the organisms[12,29,31].

In comparison with standard Gentamycin, NiL_2NH_3 exhibited more inhibitory effects against the bacterial strains than standard Gentamycin. Moreover, all the complexes showed more potent activities against *S. agalactiae* than standard Gentamycin which was inactive against it. The methoxy-substituted Ni(II) complex (NiL_2NH_3) exhibited the most potent activity among the mixed-ligand complexes.

Table 4. Antibacterial activities of the Schiff bases and the mixed-ligand complexes.

Schiff bases/ Complexes		L_1	NiL_1NH_3	L_2	NiL_2NH_3	L_3	NiL_3NH_3	DMSO	Gentamycin Standard
E. coli	5 mg	16	25	22	28	14	17	-	20
	10 mg	16	25	22	28	14	17	-	
	15 mg	17	25	22	28	18	20	-	
K. pneumoniae	5 mg	15	18	20	25	14	17	-	18
	10 mg	16	20	20	25	14	17	-	
	15 mg	16	20	20	25	14	17	-	
P. aeruginosa	5 mg	17	20	30	34	14	16	-	20
	10 mg	17	20	30	34	14	16	-	
	15 mg	19	28	30	34	14	16	-	
S. agalactiae	5 mg	14	18	22	26	10	14	-	
	10 mg	14	20	22	26	10	14	-	
	15 mg	14	20	22	26	12	18	-	
S. aureus	5 mg	16	20	30	33	15	18	-	20
	10 mg	16	20	30	33	15	18	-	
	15 mg	17	24	30	33	17	19	-	
S. typhimurium	5 mg	15	20	18	24	17	19	-	17
	10 mg	16	20	18	24	17	19	-	
	15 mg	16	20	18	24	17	19	-	
P. mirabilis	5 mg	14	16	25	28	12	14	-	20
	10 mg	14	16	25	28	12	14	-	
	15 mg	14	16	25	28	13	15	-	

Resistant, not sensitive (< 8 mm), sensitive (9−14 mm), very sensitive (15−19 mm) and ultrasensitive (> 20 mm)[16].

3.4. Total antioxidant capacity

The results of the total antioxidant capacities of the Schiff bases and the NI(II) mixed-ligand complexes are presented in Table 5. The mixed-ligand complexes showed higher total antioxidant capacities than the Schiff base ligands. NiL_2NH_3 exhibited the highest TAC among the mixed-ligand complexes. The difference in the TAC of the Schiff bases and the mixed-ligand complexes could be due to the coordination of the metal ions and probably the presence of ammonia molecules in the complexes. The coordination of metal after complexation of the system increases its capacity to stabilize unpaired electrons and consequently, to scavenge free radicals[27]. Hence, the mixed-ligand complexes are better antioxidants than the free Schiff base ligands.

Eclética Química Journal, vol. 45, n. 1, 2020, 18-43
ISSN: 1678-4618
DOI: 10.26850/1678-4618eqj.v45.1.2020.p18-43

Table 5. Total antioxidant capacities of the Schiff bases and the mixed-ligand complexes.

Schiff bases/Complexes	TAC µg per mg AA
L_1	0.68
NiL_1NH_3	0.96
L_2	0.78
NiL_2NH_3	1.27
L_3	0.62
NiL_3NH_3	0.71

4. Conclusions

Nickel(II) mixed-ligand complexes containing ammonia, N-(salicylidene)-*o*-aminophenol, N-(5-methoxysalicylidene)-*o*-aminophenol and N-(2-hydroxy-1-naphthalidene)-*o*-aminophenol were synthesized and characterized by different techniques. The melting points, elemental analyses, IR, ^{1}H NMR, ^{13}C NMR and UV-Visible confirmed the formation of the mixed-ligand complexes. Theoretical calculations of the structures of the Ni(II) mixed-ligand complexes, their UV-Visible and IR and NMR spectra were performed to augment the experimental results. Based on the electronic spectra data, elemental analyses and the theoretical calculations, a distorted square planar geometry was proposed for the complexes. The antibacterial and total antioxidant activities of the complexes follow the order: NiL_2NH_3 > NiL_1NH_3 > NiL_3NH_3.

5. Acknowledgments

Abidemi Iyewumi Demehin appreciates the Organization of Women in Science in Developing World (OWSD), Trieste, Italy, for the research fellowship granted to her to study in the Department of Chemistry, University of Malaya, Kuala Lumpur, Malaysia. She is grateful to Prof. M. A. Hapipah of the Department of Chemistry, University of Malaya, for allowing the use of her laboratory for the research and providing the analyses.

6. References

[1] Kundu, S., Pramanik, A. K., Mondal, A. S., Mondal, T. K., Ni(II) and Pd(II) complexes with new N,O donor thiophene appended Schiff base ligand: Synthesis, electrochemistry, X-ray structure and DFT calculation, Journal of Molecular Structure 1116 (2016) 1-8. https://doi.org/10.1016/j.molstruc.2016.03.013.

[2] Schilf, W., Kamienski, B., Szady-Chełmieniecka, A., Kołodziej, B., Grech, E., Zarzeczanska, D., Wcisło, A., Ossowski, T., Structure investigation of intramolecular hydrogen bond in some substituted salicylaldehydes and 4-aminoantipyrine derivatives in solution and in the solid state, Spectrochimica Acta Part A: Molecular and Biomolecular Spectroscopy 109 (2013) 47-54. https://doi.org/10.1016/j.saa.2013.01.094.

[3] Grivani, G., Tahmasebi, V., Eskandari, K., Khalaji, A. D., Bruno, G., Rudbari, H. A., Synthesis, characterization, crystal structure determination and computational study of the two new bidentate O, N Schiff bases derived from bromosalicylaldehyde and amines containing alkyl halide pendant groups, Jounal of Molecular Structure 1054-1055 (2013) 100-106. https://doi.org/10.1016/j.molstruc.2013.09.026.

[4] Zayed, E. M., Zayed, M. A., Synthesis of novel Schiff's bases of highly potential biological activities and their structure investigation, Spectrochimica Acta Part A: Molecular and Biomolecular Spectroscopy 143 (2015) 81-90. https://doi.org/10.1016/j.saa.2015.02.024.

[5] Moosavi-Tekyeh, Z., Dastani, N., Intramolecular hydrogen bonding in N-salicylideneaniline: FT-IR spectrum and quantum chemical calculations, Journal of MolecularStructure 1102 (2015) 314-322. https://doi.org/10.1016/j.molstruc.2015.09.001.

[6] More, G., Raut, D., Aruna, K., Bootwala, S., Synthesis, spectroscopic characterization and antimicrobial activity evaluation of new tridentate Schiff bases and their Co(II) complexes, Journal of Saudi Chemical Society 21 (8) (2017) 954-964. https://doi.org/10.1016/j.jscs.2017.05.002.

[7] Schilf, W., Kamieński, B., Užarević, K., Nitrogen and carbon CPMAS NMR investigations of keto–enol tautomerism in asymmetric o-hydroxy Schiff bases, Journal of Molecular Structure 1031 (2013) 211-215. https://doi.org/10.1016/j.molstruc.2012.10.004.

[8] Aziz, A. A. A., Salaem, A. N. M., Sayed, M. A., Abo-Aly, M. M., Synthesis, structural characterization, thermal studies, catalytic efficiency and antimicrobial activity of some M(II) complexes with ONO tridentate Schiff base N-salicylidene-o-aminophenol ($saphH_2$), Journal of Molecular Structure 1010 (2015) 130-138. https://doi.org/10.1016/j.molstruc.2011.11.043.

[9] Kianfar, A. H., Farrokhpour, H., Dehghani, P., Khavasi, H. R., Experimental and theorectical spectroscopic study and structural determination of nickel(II) tridentate Schiff base complexes, Spectrochimica Acta Part A: Molecular and Biomolecular Spectroscopy 150 (2015) 220-229. https://doi.org/10.1016/j.saa.2015.05.084.

[10] Köse, M., Purtas, S., Güngör, S. A., Ceyhan, G., Akgün, E., McKee, V., A novel Schiff base: Synthesis, structural characterisation and comparative sensor studies for metal ion detections, Spectrochimica Acta. Part A, Molecular and Biomolecular Spectroscopy 136 (C) (2014) 1388-1394. https://doi.org/10.1016/j.saa.2014.10.025.

[11] Saha, S., Jana, S., Gupta, S., Ghosh, A., Nayek, H. P., Syntheses, structures and biological activities of square planar Ni(II), Cu(II) complexes, Polyhedron 107 (2016) 183-189. https://doi.org/10.1016/j.poly.2016.01.034.

[12] Ghosh, A. K., Mitra, M., Fathima, A., Yadav, H., Choudhury, A. R., Nair, B. U., Ghosh, R., Antibacterial and catecholase activities of Co(III) and Ni(II) Schiff base complexes, Polyhedron 107 (2016) 1-8. https://doi.org/10.1016/j.poly.2016.01.015.

[13] Chandra, S., Vandana, V. P., Synthesis, spectroscopic, anticancer, and antibacterial studies of Ni(II) and Cu(II) complex with 2-carboxybenzalaldehyde thiosemicarbazone, Spectrochimica Acta Part A: Molecular Biomolecular Spectroscopy 129 (2014) 333-338. https://doi.org/10.1016/j.saa.2014.02.141.

[14] Refat, M. S., El-Sayed, M. Y., Adam, A. M. A., Structural, Electronic and Thermal Studies of ChargeTransfer Complexes from the Schiff Base; *N,N´*-Disalicylidene-l,2-Phenylenediamine with Chloranilic Acid, *p*-Chloranil, TCNQ and DDQ, Canadian Chemical Transactions 2 (2014) 149-159. https://doi.org/10.13179/canchemtrans.2014.02.02.0086.

[15] Maihub, A. A., Alassbaly, F. S., El-Ajaily, M. M., Etorki, A. M., Modification on Synthesis of Mixed Ligand Chelates by Using Di- and Trivalent Transition Metal Ions with Schiff Base as Primary Ligand, Green and Sustainable Chemistry 4 (3) (2014) 103-110. https://doi.org/10.4236/gsc.2014.43015.

[16] Yousif, E., Majeed, A., Al-Sammarrae, K., Salih, N., Salimon, J., Abdullah, B., Metal complexes of Schiff base: Preparation, characterization and antibacterial activity, Arabian Journal of Chemistry 10 (Supp. 2) (2017) S1639-S1644. https://doi.org/10.1016/j.arabjc.2013.06.006.

[17] Kiran, T., Prasanth, V. G., Balamurali, M. M., Vasavi, C. S., Munusami, P., Sathiyanarayanan, K. I., Pathak, M., Synthesis, spectroscopic characterization and *in vitro* studies of new heteroleptic copper (II) complexes derived from 2-hydroxy napthaldehyde Schiff's bases and N, N donor ligands: Antimicrobial, DNA binding and cytotoxic investigations, Inorganica Chimica Acta 433 (2015) 26-34. https://doi.org/10.1016/j.ica.2015.04.033.

[18] Mazlan, N. A., Ravoof, T. B. S. A., Tiekink, E. R. T., Tahir, M. I. M., Veerakumarasivam, A., Crouse, K. A., Mixed-ligand metal complexes containing an ONS Schiff base and imidazole/benzimidazole ligands: synthesis, characterization, crystallography and biological activity, Transition Metal Chemistry 39 (6) (2014) 633-639. https://doi.org/10.1007/s11243-014-9842-9.

[19] Naik, K. H. K., Selvaraj, S., Naik, N., Metal complexes of ONO donor Schiff base ligand as a new class of bioactive compounds: Synthesis, characterization and biological evolution, Spectrochimica Acta Part A: Molecular and Biomolecular Spectroscopy 131 (2014) 599-605. https://doi.org/10.1016/.j.saa.2014.03.038.

[20] Ali, H. A., Fares, H., Darawsheh, M., Rappocciolo, E., Akkawi, M., Jaber, S., Synthesis, characterization and biological activity of new mixed ligand complexes of Zn(II) naproxen with nitrogen based ligands, European Journal of Medicinal Chemistry 89 (2015) 67-76. https://doi.org/10.1016/j.ejmech.2014.10.032.

[21] Ololade, Z. S., Olawore, N. O., Olasoji, S. O., Anosike, S. O., Chemical Composition and Bactericidal Activities of the Leaf Essential Oil of Eucalyptus maculata Hook, Natural Products Chemistry & Research 5 (2) (2017) 257. https://doi.org/10.4172/2329-6836.1000257.

[22] Pierre, B. K., Pierre, S. H., Tatjana, S., Study of Polyphenol Content and Antioxidant Capacity of Myrianthus Arboreus (Cecropiaceae) Root Bark Extracts, Antioxidants 4 (2) (2015) 410-426. https://doi.org/10.3390/antiox4020410.

[23] Ikram, M., Rehman, S., Khan, A., Baker, R. J., Hofer, T. S., Subhan, F., Qayum, F., Faridoon, M., Schulze, C., Sythesis, characterization, antioxidant and selective xanthine oxidase inhibitory studies of transition metal complexes of novel amino acid bearing Schiff base ligand, Inorganica Chimica Acta 428 (2015) 117-126. https://doi.org/10.1016/j.ica.2015.01.021.

[24] Adekunle, F. A. O., Semire, B., Odunola, O. A., Synthesis, Characterization and Quantum Chemical Studies of $Ru(phen)_2Cl_2.2H_2O$ and $Ru(bipy)_2Cl_2.2H_2O$

with 2,6- Diacetylpyridinedihydrazone, Synthesis and Reactivity in Inorganic, Metal-Organic, and Nano-Metal Chemistry 45 (8) (2015) 210-224. https://doi.org/10.1080/15533174.2013.862662.

[25] Annaraj, B., Pan, S., Neelakantan, M. A., Chattaraj, P. K., DFT study on the ground state and excited state intramolecular proton transfer of propargyl arm containing Schiff bases in solution and gas Phases, Computational and Theoretical Chemistry 1028 (2014) 19-26. https://doi.org/10.1016/j.comptc.2013.11.018.

[26] Paul, M. K., Singh, Y. D., Singh, N. B., Sarkar, U., Emissive bis-salicylaldiminato Schiff base ligands and their zinc(II) complexes: Synthesis, photophysical properties, mesomorphism and DFT studies, Jounal of Molecular Structure 1081 (2015) 316-328. https://doi.org/10.1016/j.molstruc.2014.10.031.

[27] Shabbir, M., Akhter, Z., Ahmad, I., Ahmed, S., Shafiq, M., Mirza, B., Mckee, V., Munawar, K. S., Ashraf, A. R., Schiff base triphenylphoshine palladium(II) complexes: Synthesis, structural elucidation, electrochemical and biological evaluation, Journal of Molecular Structure 1118 (2016) 250-258. https://doi.org/10.1016/j.moistruc.2016.04.003.

[28] Belal, A. A. M., El-Deen, I. M., Farid, N. Y., Rosan, Z., Refat, M. S., Synthesis, spectroscopic, coordination and biological activities of some transition metal complexes containing ONO tridentate Schiff base ligand, Spectrochimica Acta Part A: Molecular and Biomolecular Spectroscopy 149 (2015) 771-789. https://doi.org/10.1016/j.saa.2015.05.005.

[29] Salehi, M., Rahimifar, F., Kubicki, M., Asadi, A., Structural, spectrocsopic, electrochemical and antibacterial studies of some new nickel(II) Schiff base complexes, Inorganica Chimica Acta 443 (2016) 28-35. https://doi.org/10.1016/j.ica.2015.12.016.

[30] Barauah, J., Borah, G., Kardong, D., Ni(II), Cu(II) and Pd(II) Complexes of Anisaldehyde-4-phenyl-thiosemicarbazone: synthesis, spectral characterization and biological study, Asian Journal of Chemistry 28 (11) (2016) 2446-2452. https://doi.org/10.14233/ajchem.2016.20013.

[31] Abo-Aly, M. M., Salem, A. M., Sayed, M. A., Aziz, A. A. A., Spectroscopic and structural studies of the Schiff base 3-methoxy-N-salicylidene-o-amino phenol complexes with some transition metal ions and their antibacterial, antifungal activities, Spectrochimica Acta Part A: Molecular and Biomolecular Spectroscopy 136 (B) (2015) 993-1000. https://doi.org/10.1016/j.saa.2014.09.122.

Eclética Química Journal, vol. 45, n. 1, 2020, 18-43
ISSN: 1678-4618
DOI: 10.26850/1678-4618eqj.v45.1.2020.p18-43

Eclética Química Journal

Supplementary Information
iq.unesp.br/ecletica

| Vol. 45 | n. 1 | 2020 |

Supplementary information

Synthesis, spectroscopic, biological activities and DFT calculations of nickel(II) mixed-ligand complexes of tridentate Schiff bases

Abidemi Iyewumi Demehin[1], Mary Adelaide Oladipo[2+], Banjo Semire[2]

1 Adeyemi College of Education, Department of Chemistry, Ondo, Ondo State, Nigeria.
2 Ladoke Akintola University of Technology, Department of Pure and Applied Chemistry, Ogbomoso, Oyo State, Nigeria.

+Corresponding author: Mary Adelaide Oladipo, Phone: +234 803 3817017 email address: mooladipo@lautech.edu.ng

ARTICLE INFO

Article history:
Received: March 02, 2019
Accepted: November 11, 2019
Published: January 1, 2020

Keywords:
1. Schiff bases
2. antibacterial
3. antioxidant
4. nickel(II) ion
5. mixed-ligand complex

^{13}C-NMR DATA

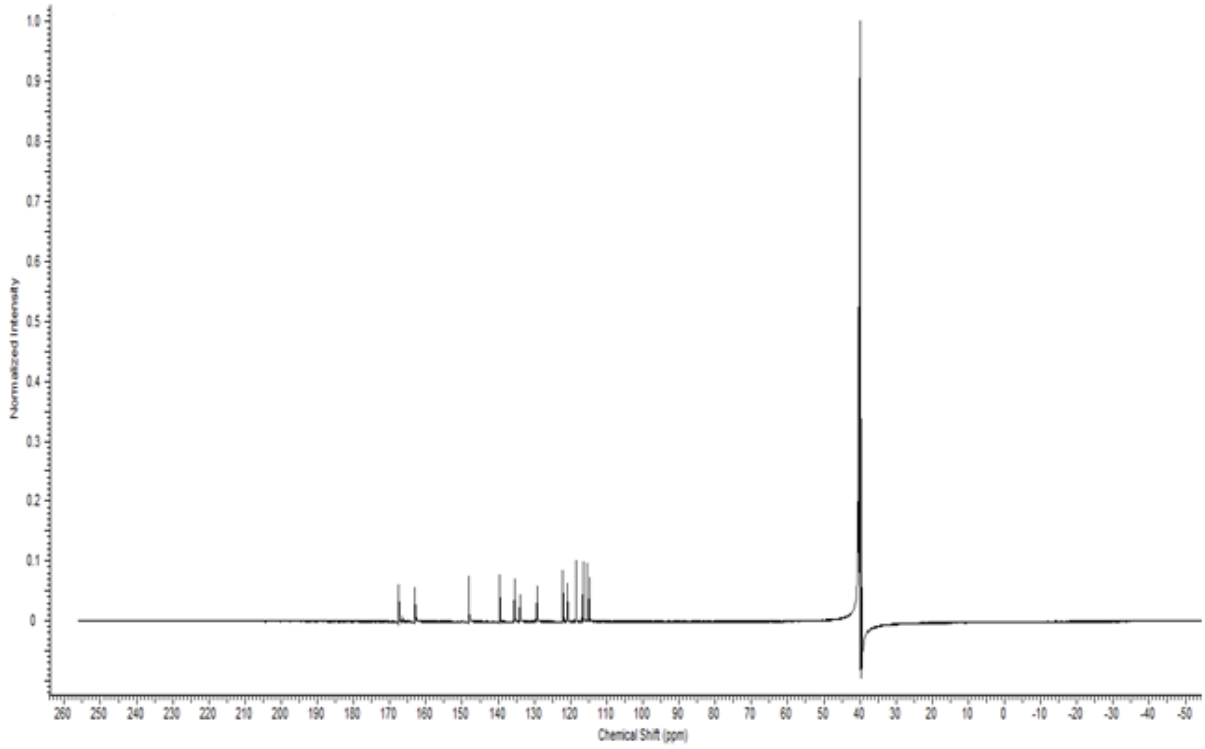

Figure S1. ^{13}C NMR of NiL_1NH_3 complex.

Eclética Química Journal, vol. 45, n. 1, 2020, 44-46
ISSN: 1678-4618
DOI: 10.26850/1678-4618eqj.v45.1.2020.p44-46

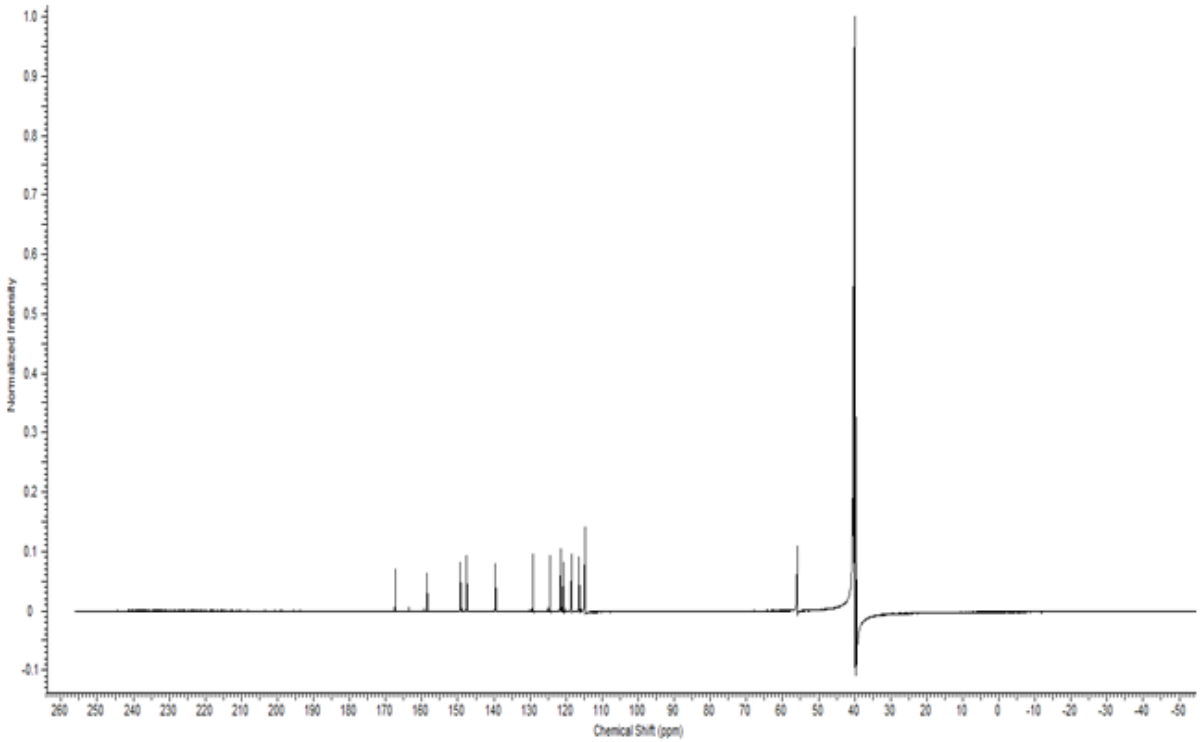

Figure S2. ^{13}C NMR of NiL_2NH_3 complex.

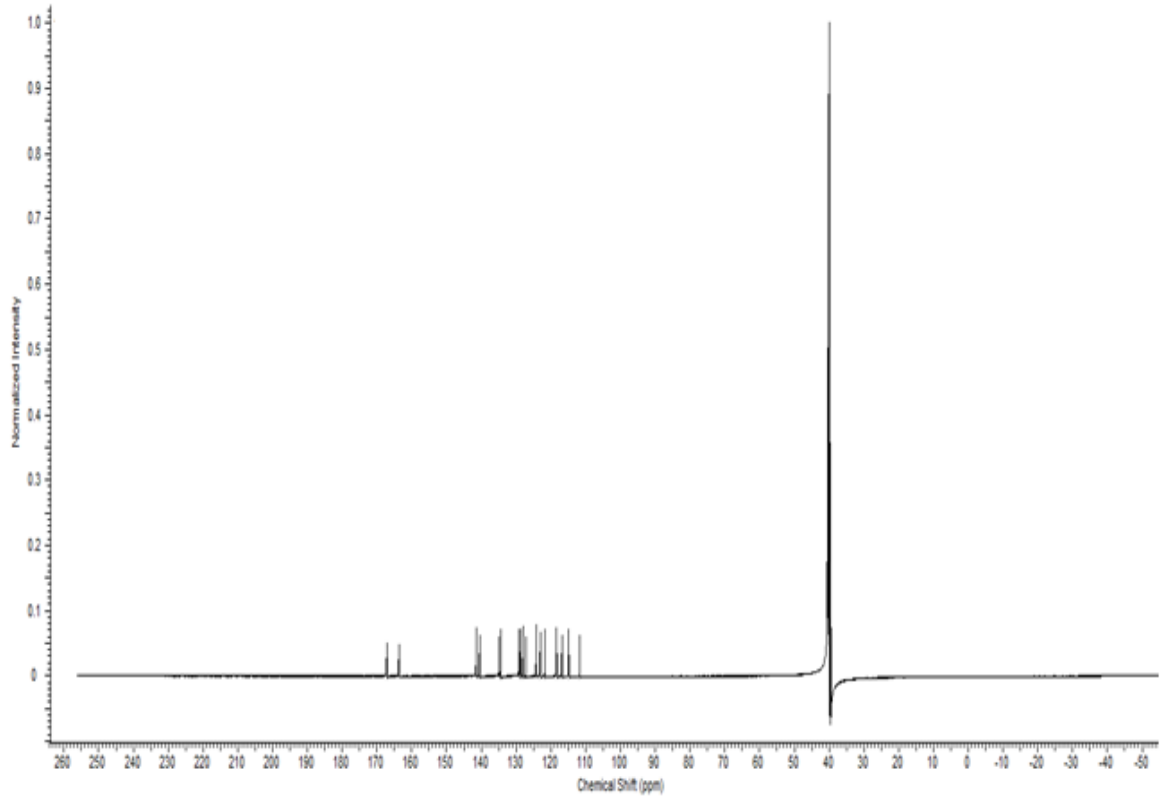

Figure S3. ^{13}C NMR of NiL_3NH_3.

Eclética Química Journal, vol. 45, n. 1, 2020, 44-46
ISSN: 1678-4618
DOI: 10.26850/1678-4618eqj.v45.1.2020.p44-46

Table S1. Selected bond distances and bond angles.

NiL_1NH_3			NiL_2NH_3			NiL_3NH_3		
Bond (Å)	**B3LYP**	**EDF1**	**Bond (Å)**	**B3LYP**	**EDF1**	**Bond (Å)**	**B3LYP**	**EDF1**
Ni1−N1	1.844	1.818	Ni1−N1	1.845	1.817	Ni1−N1	1.834	1.811
Ni1−N2	1.936	1.944	Ni1−N2	1.938	1.940	Ni1−N2	1.939	1.943
Ni1−O1	1.818	1.807	Ni1−O1	1.814	1.807	Ni1−O1	1.813	1.801
Ni1−O2	1.825	1.825	Ni1−O2	1.827	1.825	Ni1−O2	1.823	1.823
O2−C9	1.327	1.332	O2−C9	1.327	1.331	O2−C15	1.328	1.333
O1−C4	1.310	1.317	O1−C4	1.314	1.322	O1−C8	1.306	1.315
N1−C7	1.307	1.322	N1−C7	1.307	1.322	N1−C11	1.312	1.326
N1−C8	1.418	1.418	N1−C8	1.417	1.417	N1−C12	1.418	1.417
C3−C4	1.432	1.338	C3−C4	1.432	1.437	C12−C15	1.416	1.419
C3−C7	1.427	1.423	C3−C7	1.428	1.425	C7−C11	1.424	1.424
C8−C9	1.415	1.418	C8−C9	1.416	1.419	C7−C8	1.424	1.430
Bond angles (o)								
N1−Ni1−N2	176.19	174.63	N1−Ni1−N2	174.83	175.69	N1−Ni1−N2	176.37	175.97
O1−Ni1−O2	174.78	173.60	O1−Ni1−O2	174.62	173.34	O1−Ni1−O2	175.35	174.06
N1−Ni1−O2	88.21	88.40	N1−Ni1−O2	88.04	88.51	N2−Ni1−O2	87.85	87.22
N1−Ni1−O1	97.00	94.60	N1−Ni1−O1	97.33	98.15	N2−Ni1−O1	87.60	87.02
N2−Ni1−O2	87.98	86.23	N2−Ni1−O2	86.80	87.18	N1−Ni1−O1	96.02	96.98
N2−Ni1−O1	86.81	87.37	N2−Ni1−O1	87.83	86.16	N1−Ni1−O2	88.52	88.79
Ni1−N1−C8	111.00	111.76	Ni1−N1−C8	111.12	111.73	Ni1−O2−C15	111.44	111.26
Ni1−N1−C7	125.23	124.98	Ni1−N1−C7	125.21	125.05	Ni1−O1−C8	127.74	127.39
Ni1−O2−C9	111.66	111.69	Ni1−O2−C9	111.81	111.44	Ni1−N1−C11	125.61	125.30
Ni1−O1−C4	127.14	126.68	Ni1−O1−C4	126.63	126.40	Ni1−N1−C12	111.00	111.64
N1−C8−C9	111.24	111.00	N1−C8−C9	111.28	110.99	N1−C12−C15	111.28	111.03
N1−C7−C3	125.10	125.14	N1−C7−C3	124.97	125.06	N1−C11−C7	125.84	125.89
O1−C4−C3	123.56	123.52	O1−C4−C3	123.96	123.67	O2−C15−C12	117.75	117.25
O2−C9−C8	117.88	117.23	O2−C9−C8	117.74	117.34	O1−C8−C7	124.46	124.21
C4−C3−C7	121.96	121.68	C4−C3−C7	121.89	121.67	C8−C7−C11	120.28	120.10

Eclética Química Journal, vol. 45, n. 1, 2020, 44-46
ISSN: 1678-4618
DOI: 10.26850/1678-4618eqj.v45.1.2020.p44-46

Eclética Química Journal

Original article
iq.unesp.br/ecletica

| Vol. 45 | n. 1 | 2020 |

Determination of harpagoside in *Harpagophytum procumbens* DC tablet's using analytical method by High Performance Liquid Chromatography

Gislane dos Santos Ribeiro, Amanda de Assis Carneiro, Diegue Henrique Nascimento Martins, Luiz Alberto Simeoni, Dâmaris Silveira, Pérola Oliveira Magalhães, Yris Maria Fonseca-Bazzo+

University of Brasília (UnB), Health Sciences School, Department of Pharmaceutical Sciences, Laboratory of Natural Products (LaProNat), Brasília, DF, Brazil

+Corresponding author: Yris Maria Fonseca-Bazzo, Phone: +55 61 3107 1806 email address: yrisfonseca@unb.br

ARTICLE INFO

Article history:
Received: March 02, 2019
Accepted: November 11, 2019
Published: January 01, 2020.

Keywords:
1. herbal medicines
2. quality control
3. *Harpagophytum procumbens*
4. devil's claw

ABSTRACT: The species *Harpagophytum procumbens* DC. is popularly known as devil's claw and is widely used because of its anti-inflammatory properties that are attributed to an iridoid glycoside, the harpagoside. This medicinal plant is part of the Brazilian List of Essential Medicines, that is, it was selected and standardized for the resolution of diseases in the Brazilian public health system (*Sistema Único de Saúde* – SUS) and can be found in several brands. Due to the importance of quality monitoring, the objective of this study was to create and validate a method for identification and quantification of harpagoside in tablets of the devil's claw, as well as to evaluate the content of this iridoid glycoside in three commercially available brands in Brasília/DF, Brazil. The evaluated parameters in the validation by high performance liquid chromatography were linearity, limits of detection and quantification, precision, selectivity, accuracy and robustness, as required by the Brazilian regulation. The developed and validated method proved satisfactory for the quality control of commercial products that present in this composition the medicinal plant. All the devil's claw brands presented divergences regarding the quality that can interfere with therapeutics and with safety and efficacy.

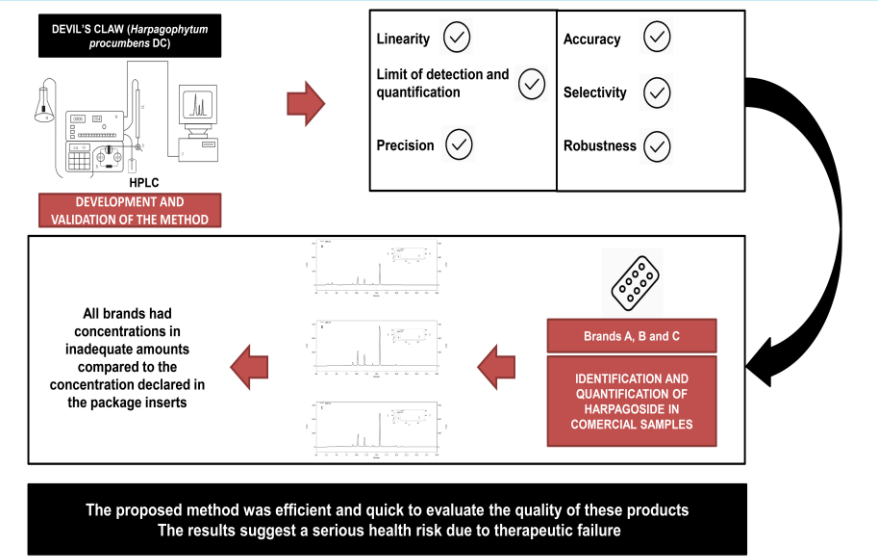

1. Introduction

The consumption of herbal medicines grows markedly in developed and developing countries[1]. In Brazil, for example, about 85% of the population uses some herbal medicine or medicinal plant[2,3].

Harpagophytum procumbens DC. belongs to the family Pedaliaceae and it is known as devil's claw[4]. The secondary roots of this medicinal plant have been used for centuries for a variety of diseases. From ethnological data, this plant is used in folk medicine to treat fever, arthritis, skin problems, diseases of the digestive tract and as an appetite stimulant[5]. From various studies and clinical evidence, devil's claw is indicated as an anti-inflammatory and analgesic in the treatment of rheumatic diseases, such as osteoarthritis, in

Eclética Química Journal, vol. 45, n. 1, 2020, 47-55
ISSN: 1678-4618
DOI: 10.26850/1678-4618eqj.v45.1.2020.p47-55

addition to alleviating the symptoms of acute low back pain, myalgias and other osteoarticular and muscular pathologies[5,6].

The harpagoside is an iridoid glycoside considered to be responsible for the pharmacological activity of *H. procumbens* DC. This compound is considered the chemical marker of this species. Therefore, it is used as a control to standardize commercial products[7].

Some factors can compromise the quality of herbal products from the cultivation of the raw material to the final product, such as contamination, the presence of foreign materials, botanical identification errors, among others. These factors result from the lack of care in the collection and identification of the species. Also, adulterations are common to increase the yield of the product. All these factors affect the quality, safety and efficacy of herbal medicines and emphasize the importance of quality control from the cultivation of the raw material to the finished product, as well as phytochemical, pharmacological and toxicological studies[8,9].

Chromatographic and analytical techniques are used in recognition of the chemical composition, including active principle or toxic compound. These techniques allow the separation and isolation of the substances thus allowing both qualitative and quantitative control of the compounds considered marker of the species. High performance liquid chromatography (HPLC) is one of those techniques widely used for the complete characterization of plant and herbal products, being an important tool in the control of the quality of these products[9,10].

Pharmacopoeias and monographs are relevant to establish quality standards in addition to standardizing and systematizing knowledge of medicinal plants. These tools present characteristics and properties of plants such as macroscopic and microscopic description, general aspects of the vegetal drug besides identification, purity and assay tests that help in the quality control[11].

Pharmacopeial methods (for example, in the Brazilian Pharmacopoeia) for the quality control of the plant drug *Harpagophytum procumbens* (meaning dried roots of devil's claw) are available. However, there isn't specific monograph for herbal medicines/dosage forms containing it[12]. In the Brazilian Pharmacopeia the described method uses flow rate 1.5 mL in an isocratic system with water and methanol (50:50). In addition, the method refers to the dosage in plant drug and not to the finished product[12].

According to the Brazilian regulatory agency (*Agência Nacional de Vigilância Sanitária – Anvisa*) when a monograph contemplates only analytical method for identification and quantification of markers for the vegetal drug, it is necessary to make adaptations and validate the method for the finished product[13].

In the literature there are other published methods for harpagoside determination using isocratic or gradient elution with flow rate above 1 mL min^{-1} and analysis time around 60 min[14,15]. The proposed method utilizes a flow rate of 0.6 mL min^{-1} with gradient mode over 30 min of analysis. A quick method with greater solvent savings.

Therefore, this study aimed to develop and validate an analytical method using HPLC to contribute to the establishment of quality parameters for the finished product of this widely used medicinal plant, as well as to identify and quantify the harpagoside in commercial samples.

2. Materials and methods

2.1 Standard, samples and reagents

Harpagoside, considered chemical marker of the species and used for standardization of commercial products, was provided by Sigma-Aldrich. Three different brands of devil's claw tablets were obtained from pharmacies in Brasília, Brazil, named as brand A, B and C. About the concentration of dry extract of the roots of *H. procumbens*, the brands A, B, and C presented, respectively, 200, 400 and 450 mg. Regarding the total iridoid equivalents calculated as harpagoside, each tablet of the A, B and C brands had declared 10, 20 and 18 mg, respectively. The solvents (HPLC grade) used in the assay were phosphoric acid (Sigma), acetonitrile (Tedia) and methanol (Tedia). The mobile phase was prepared with purified water produced in the Milli-Q system (Millipore).

2.2 Sample and standard preparation

Twenty tablets of each brand were macerated using mortar and pestle. A portion equivalent to 40 mg of dry extract of the roots of *H. procumbens* was weighed, solubilized in methanol and prepared at the concentration of 4 mg mL^{-1}

Eclética Química Journal, vol. 45, n. 1, 2020,47-55
ISSN: 1678-4618
DOI: 10.26850/1678-4618eqj.v45.1.2020.p47-55

(this concentration is equivalent to 530 µg mL^{-1} of harpagoside). The resulting solution was filtered through a 0.45 µm porosity disposable filter unit (Millipore Millex). The harpagoside standard was weighed and solubilized in methanol resulting in a concentration of 100 µg mL^{-1}.

2.3 Chromatographic conditions

The LaChrom Elite chromatograph (Hitachi, Tokyo, Japan) was used for the analysis, contains an L2130 pump, L2200 injector, L2455 detector and L2300 column oven. The column used was the reverse phase C18e Purospher Star (150 × 4.6 mm, 5 µm, Merck, Germany). The temperature conditions, flow, injection volume and detection wavelength were 25 °C, 0.6 mL min^{-1}, 10 µL and 280 nm, respectively. A gradient of 1% phosphoric acid and acetonitrile (Table 1) was used in the mobile phase. The total analysis time was 30 min.

Table 1. Chromatographic conditions of the mobile phase gradient.

Time / min	Phosphoric acid 1% / %	Acetonitrile / %
0 - 20	80	20
20 - 21	50	50
21 - 25	80	20
25 - 30	80	20

2.4 Development and validation of the method by HPLC-DAD

Leite *et al.*'s method (2014)[16] was used with alterations to evaluate the finished product referring to devil's claw. The validation was carried out in accordance to the requirements of the Brazilian legislation, evaluating the parameters of linearity, limits of detection and quantification, precision, accuracy, selectivity and robustness[17] and international guidelines for the industrial sector (International Conference on Harmonization)[18].

2.4.1 Linearity

Linearity was determined from three analytical curves with six concentrations of the harpagoside standard: 100.0, 200.0, 300.0, 500.0, 700.0 and 800.0 µg mL^{-1}. From these curves, linearity equations were obtained by linear regression. The software used to obtain these equations was GraphPad Prism Version 6.01 2012. The proportional linear relation to the concentration and correlation coefficient should be higher than 0.9900.

2.4.2 Limit of Detection (LOD) and Quantification (LOQ)

The slope (s) of the calibration curve and the standard deviation (SD) of the three calibration curves were considered, taking into account the intercept with the Y-axis. These data are used in the equations to obtain LOD values and LOQ, that is, the smallest amount of marker that can be detected and quantified, respectively:

$$LOD = (SD \times 3.3)/s; \quad LOQ = (SD \times 10)/s \quad (1)$$

2.4.3 Precision

According to the Brazilian legislation, precision must be expressed by repeatability, intermediate precision or reproducibility[17]. The repeatability determination was performed with six replicates with at 100% of the test concentration (4 mg mL^{-1}, this concentration is equivalent to 530 µg mL^{-1} of harpagoside) and were analyzed on the same day. In the interday precision, three replicates with the same concentration (4 mg mL^{-1}) were evaluated on three consecutive days.

2.4.4 Accuracy

In this study, the accuracy evaluation was done using the standard addition method, using nine determinations with three levels of theoretical concentration (low, medium and high) in triplicate for each level. In the case of finished product, according to the Brazilian legislation, if samples of all drug components are unavailable, analysis by the standard chemical addition method may be performed, in which know quantities of reference chemical are added to the solution of the finished prduct[17]. The theoretical concentrations used were calculated at 80, 100 and 120%; these concentrations were achieved using 500 µL of the commercial *H. procumbens* sample with 500 µL of the harpagoside standard. The harpagoside recovery percentage added to the sample was evaluated by the relation between the experimentally determined concentration and the corresponding theoretical concentration.

Eclética Química Journal, vol. 45, n. 1, 2020,47-55
ISSN: 1678-4618
DOI: 10.26850/1678-4618eqj.v45.1.2020.p47-55

2.4.5 Selectivity

The method ability to identify the harpagoside in the presence of impurities, degradation compounds or other components in the sample was assessed from induction of acidic and basic hydrolysis. The assay was done in triplicate, and the samples were solubilized using 1 mol L^{-1} HCl for acid hydrolysis and 1 mol L^{-1} NaOH for basic hydrolysis. After solubilization, the samples were placed in a water bath for 1 h at 60 °C. After 1 h, the samples were taken from the water bath and expected to reach room temperature to be neutralized with 1 mol L^{-1} HCl or 1 mol L^{-1} NaOH solution, regarding the sample, and diluted in methanol. The final concentration was 4 mg mL^{-1}. The selectivity was evaluated by comparing the retention times and peak areas in the samples without hydrolysis and the samples submitted to the induction of acid and basic hydrolysis.

2.4.6 Robustness

The parameters chosen for the variation were temperature (23-27 °C), wavelength (270-290 nm) and flow of the mobile phase (0.4-0.8 mL min^{-1}). From these variations, the effects on the retention time and peak area were observed to evaluate if the method was robust.

2.5 Identification and quantification of harpagoside in commercial samples

The validated method was used to evaluate the presence of harpagoside, used to standardize commercial products, in the three brands of *H. procumbens*. The harpagoside identification in the samples was made comparing the peaks retention time and UV spectrum presented by the harpagoside standard with the standard peak of the samples. The harpagoside quantification was made from the linearity curve, in which the quantity of this marker could be calculated in the samples.

2.6 Statistical analysis of data

The GraphPad Prism 6.01 software. Data was used for the statistical analyzes of the data obtained in this study, and the results were expressed as the mean ± standard deviation (SD).

3. Results and discussion

3.1 Method validation

The method was optimized for a 30 min analysis time (while the original method was 55 min) using a C18e Purospher Star reverse phase column (150 × 4.6 mm, 5 µm). The mobile phase used was a gradient of 1% phosphoric acid and acetonitrile using a flow rate of 0.6 mL min^{-1}, injection volume of 10 µL and the chromatograms extracted at 280 nm wavelength.

Some parameters were evaluated for system suitability such as resolution (3.90 ± 0.03), retention time (15.85 ± 0.01), repeatability (14,600,558 ± 629,334), plate number (13713 ± 379) and tailing factor (1.2 ± 0.1).

3.1.1 Linearity, limit of detection (LOD) and limit of quantification (LOQ)

The method presented a linear response in the range of 100 to 800 µg mL^{-1} of concentrations. This correlation was made between the area of the peaks and their respective concentrations in triplicate. According to the Brazilian legislation, the correlation coefficient should be higher than 0.9900, and the method under study had a correlation coefficient of 0.9992, according to the requirements, demonstrating the linearity of the method[15]. From the linearity curve, LOD and LOQ were obtained: 1.12 µg mL^{-1} and 3.39 µg mL^{-1}, respectively. The linearity and dispersion of residues graph are shown in Fig. 1.

Eclética Química Journal, vol. 45, n. 1, 2020,47-55
ISSN: 1678-4618
DOI: 10.26850/1678-4618eqj.v45.1.2020.p47-55

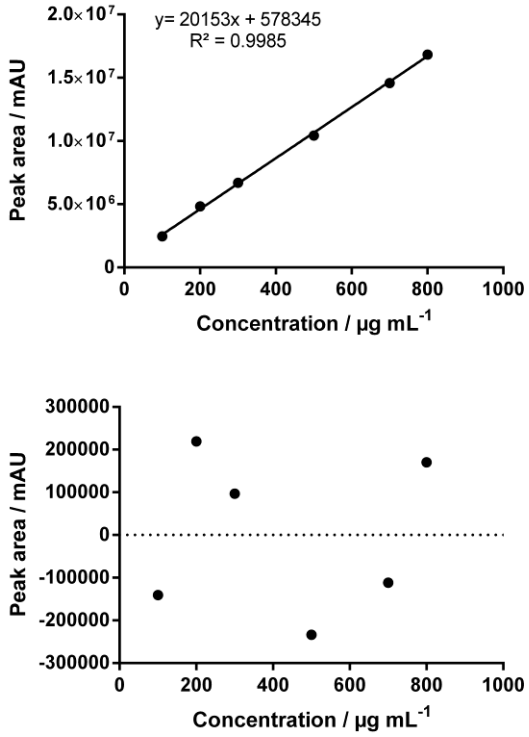

Figure 1. Linearity and dispersion of residues graph.

3.1.2 Precision

Regarding the precision of the results, the method demonstrated repeatability when presenting a standard deviation between the replicates of 4.31% for the intraday precision and 4.06% for the interday precision, not higher than 5% as recommended by the legislation[17].

3.1.3 Accuracy

The accuracy of the method was evaluated by the standard addition method to the samples of known concentration. The objective of this method is to identify and quantify the harpagoside in commercial samples for that reason, the percentage of recovery the closer to 100%, more accurate the method will be for this quantification. The obtained results showed this proximity, confirming that the method is accurate for the proposed objective, presenting a relative standard error of less than 5% (Table 2).

Table 2. Harpagoside recovery analysis after standard addition method.

Theoretical concentration / µg mL^{-1}	Discovered concentration / µg mL^{-1} ± SD	Recovery / %	E / %
100.869 (80%)	97.2 ± 0.1	96.33	3.67
126.087 (100%)	120.0 ± 0.3	95.20	4.80
151.304 (120%)	150 ± 1	99.02	0.98

E: relative standard error

3.1.4 Selectivity

The purity of the peak of interest in the sample without acid or basic hydrolysis was pure = 1.00 ± 0.00. The method was selective to demonstrate that after induction of acidic and basic hydrolysis there was a complete degradation of the harpagoside peak and formation of degradation compounds (a degradation product peak formed with a purity of 0.995 ± 0.005 with retention time 19.870 ± 0.007 min in basic hydrolysis and 0.94 ± 0.04 with retention time 19.890 ± 0.003 min in acid hydrolysis), and there was no co-elution of these with the peak of the marker. In this way, the method can identify and quantify the harpagoside in the presence of other substances.

3.1.5 Robustness

After the variations in wavelength and temperature parameters, no significant changes in the retention time and area of the harpagoside peak was observed. These results demonstrate that the proposed method is robust. However, regarding the flow variation, considerable changes in the retention time and area of the peak were observed, as can be seen in Table 3. From these results, the flow is a parameter that must be very well accompanied because the notorious influence on the separation of substances and especially on the purity of the harpagoside marker peak.

Eclética Química Journal, vol. 45, n. 1, 2020,47-55
ISSN: 1678-4618
DOI: 10.26850/1678-4618eqj.v45.1.2020.p47-55

Table 3. Parameters for analysis for robustness of the HPLC analytical method.

Wavelength / nm	Peak area / mAU	Retention time / min
270	12,578,713 ± 512,794	15.82 ± 0.01
280	14,070,719 ± 585,792	15.82 ± 0.01
290	12,045,012 ± 494,637	15.82 ± 0.01
Temperature / °C	**Peak area / mAU**	**Retention time / min**
23	14,795,700 ± 87,333	15.802 ± 0.01
25	14,853,562 ± 133,593	15.811 ± 0.01
27	15,183,982 ± 120,467	15.804 ± 0.01
Flow / mL min^{-1}	**Peak area (mAU)**	**Retention time (min.)**
0.4	20,944,078 ± 211,746	20.19 ± 0.01
0.6	14,122,976 ± 174,969	15.807 ± 0.01
0.8	10,859,776 ± 27,804	13.445 ± 0.01

3.2 Identification and quantification of harpagoside in commercial samples

The method developed and duly validated according to the legislation was used to identify and quantify harpagoside in the three commercial brands of *H. procumbens* available in Brasília/DF, Brazil. The chromatographic profiles were obtained using the proposed analytical method, and harpagoside was identified in the samples from the retention time and UV spectrum (Fig. 2).

All brands presented the harpagoside in its composition. The harpagoside was possible to quantify from the peak area of the marker, and all the brands had concentrations in inadequate amounts compared to the concentration declared in the package inserts (Table 4). The declared values compared to the amount found experimentally presented a variation in disagreement with the allowed of ± 15% [17] (Table 4).

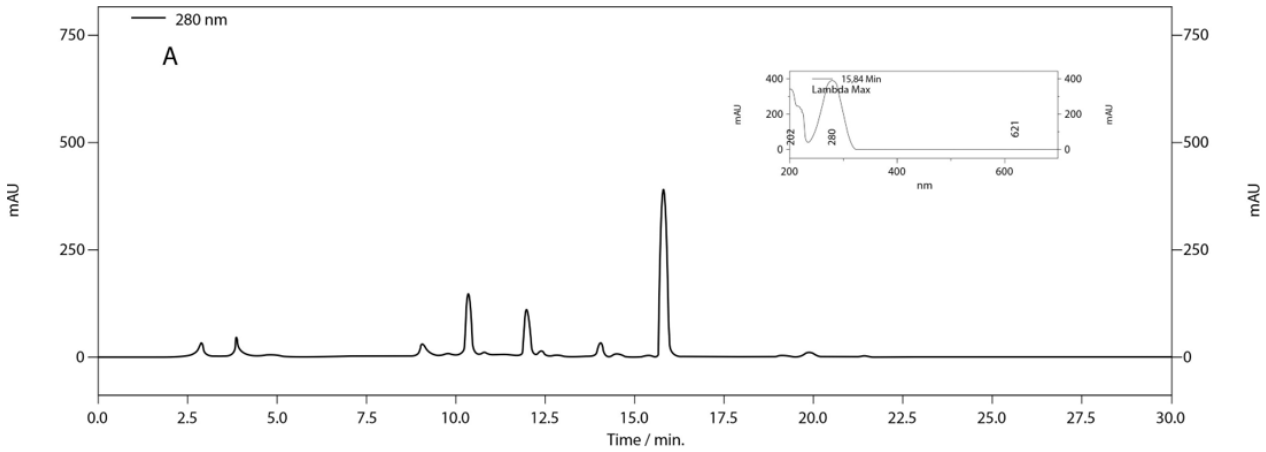

Eclética Química Journal, vol. 45, n. 1, 2020,47-55
ISSN: 1678-4618
DOI: 10.26850/1678-4618eqj.v45.1.2020.p47-55

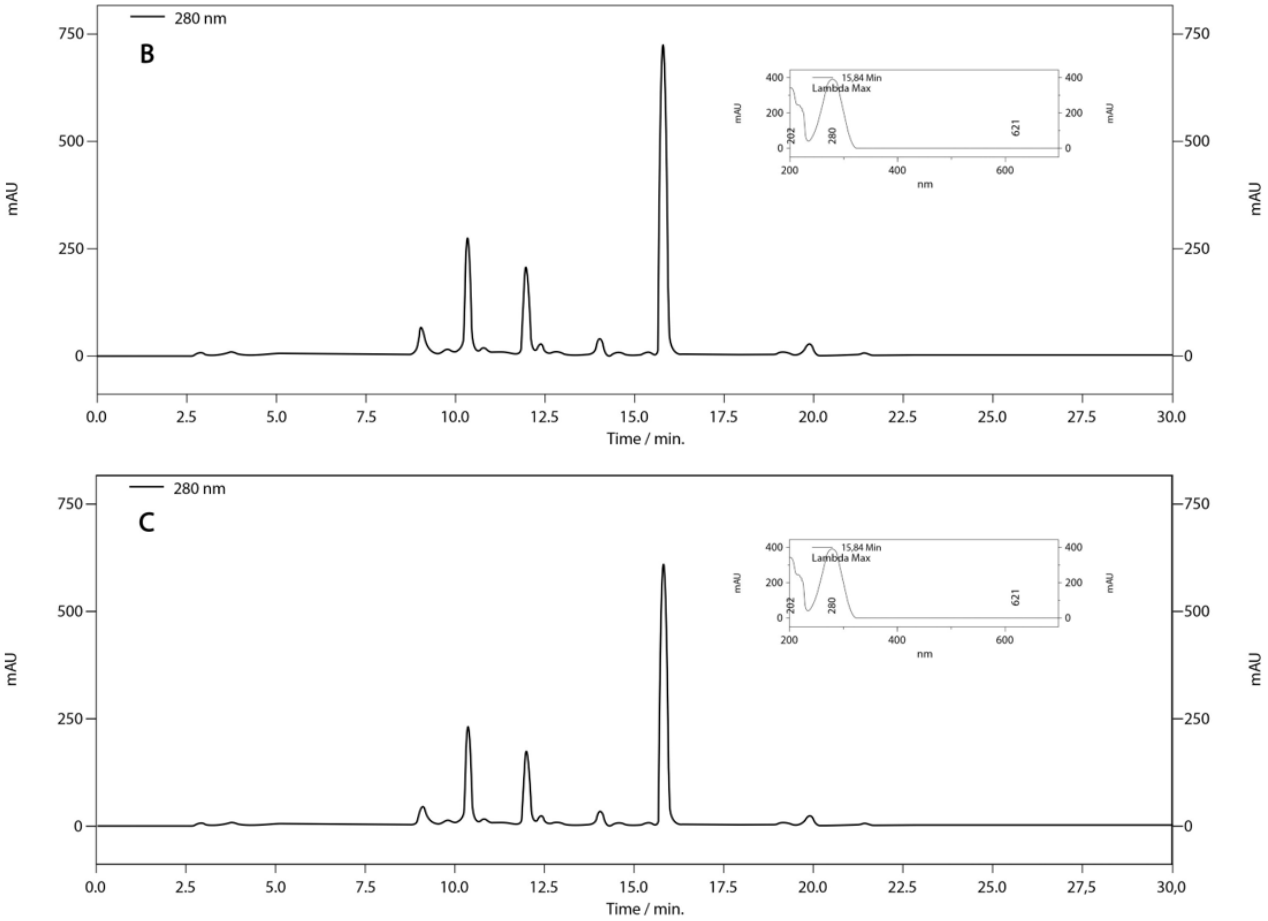

Figure 2. Chromatographic profiles of the brands A, B and C of the herbal medicine *Harpagophytum procumbens* obtained using HPLC-DAD with detection at 280 nm. 1: Harpagoside.

Table 4. Harpagoside concentration in *Harpagophytum procumbens* DC tablets and experimentally determined daily dose compared to the concentration stated in the package inserts.

Brand	Concentration of harpagoside / mg mL^{-1}		*Variation of harpagoside concentration / %	**Daily dose of harpagoside / mg
	Declarated	Determinated		
A	0.05	0.0290 ± 0.0009	- 42.00	17.40
B	0.05	0.064 ± 0.001	+ 28.00	76.80
C	0.04	0.0510 ± 0.0002	+ 27.50	68.70

* Variation allowed by the Brazilian legislation is ± 15%[13]

** Daily dose recommended by the Brazilian legislation is 30 to 100 mg[17]

For all brands, the suggested posology was one tablet three times a day. To find the daily doses, a relation between the declared value and the experimentally determined harpagoside content was done. The results showed that, regarding the daily posology, all brands were out the specifications determined by the Brazilian legislation (30 to 100 mg)[13] (Table 4). This fact can imply in possible toxic effects due to an overdosage, considering the active principle of herbal medicines presents pharmacological action[19]. Therefore, these results suggest a serious health risk due to therapeutic failure or toxicity. One study demonstrated that the majority of patients responded more to treatment using the highest daily dose of harpagoside (100 mg), as well as the adverse events are predictable and dose-dependent. The active principle is bitter and stimulates the production of gastrointestinal juice. Therefore, adverse events are mainly gastrointestinal[20].

Eclética Química Journal, vol. 45, n. 1, 2020,47-55
ISSN: 1678-4618
DOI: 10.26850/1678-4618eqj.v45.1.2020.p47-55

4. Conclusion

The proposed method in this study for the identification and quantification of harpagoside in the herbal medicine devil's claw was efficient and quick to evaluate the quality of these products to ensure authenticity, credibility, safety and therapeutic efficacy. The obtained results emphasize the importance of quality control since we observed, in all three medicinal products, significant variations in the quantity of harpagoside in comparison to the value declared in the registry of these products.

5. Acknowledgments

The authors greatly acknowledge Research program for the SUS: shared management in health PPSUS - FAP/DF/SESDF/MS/CNPQ (Grant number 193.000.860/2014), National Council for Scientific and Technological Development (CNPq), Foundation for Research Support of the Federal District (FAPDF), Coordination of Improvement of Higher Education Personnel (CAPES) and University of Brasília (DPP/UnB) for the financial support to carry out this research.

6. References

[1] Terra-Junior, O. N., Maldonado, J. V., Arnobio, A., Estudo do desempenho comercial dos insumos farmacêuticos vegetais sob a ótica do Comércio Exterior, Revista Fitos 9 (3) (2015) 233-246. https://www.arca.fiocruz.br/handle/icict/19237.

[2] Brasil, Ministério da Saúde. Política Nacional de Plantas Medicinais e Fitoterápicos, Brasília: Ministério da Saúde (2006). http://bvsms.saude.gov.br/bvs/publicacoes/politica_nacional_fitoterapicos.pdf.

[3] Moura, M. G., Lopes, L. C., Biavatti, M. W., Busse, J. W., Wang, L., Kennedy, S. A., Bhatnaga, N., Bergamaschi, C. C., Brazilian oral herbal medication of osteoarthritis: a systematic review protocol, Systematic Reviews 5 (86) (2016) 1-7. https://doi.org/10.1186/s13643-016-0261-1.

[4] Tropicos. Missouri Botanical Garden, *Harpagophytum procumbens*, Tropicos (2017). http://www.tropicos.org/Name/24300038.

[5] Grant, L., McBean, D. E., Fyfe, L., Warnock, A. M., A review of the biological and potencial therapeutic actions of *Harpagophytum procumbens*, Phytotherapy Research 21 (3) (2007) 199-209. https://doi.org/10.1002/ptr.2029.

[6] Mncwangi, N., Chen, W., Vermaak, I., Viljoen, A. M., Gericke, N., Devil's Claw - A review of the ethnobotany, phytochemistry and biological activity of *Harpagophytum procumbens*, Journal of Ethnopharmacology 143 (3) (2012) 755-771. https://doi.org/10.1016/j.jep.2012.08.013.

[7] Georgiev, M. I., Ivanovska, N., Alipieva, K., Dimitrova, P., Verpoorte, R., Harpagoside: from Kalahari Desert to pharmacy shelf, Phytochemistry 92 (2013) 8-15. https://doi.org/10.1016/j.phytochem.2013.04.009.

[8] Oliveira, E. M. A., Maywald, P. G., Rosa, G. A. A., Distribuição de plantas medicinais e fitoterápicos através do SUS, E-RAC 3 (1) (2013) 3-19. http://www.computacao.unitri.edu.br/erac/index.php/e-rac/article/view/141.

[9] Souza-Moreira, T. M., Salgado, H. R. N., Pietro, R. C. L. R., O Brasil no contexto de controle de qualidade e plantas medicinais, Revista Brasileira de Farmacognosia 20 (3) (2008) 435-440. https://doi.org/10.1590/S0102-695X2010000300023.

[10] Tistaert, C., Dejaegher, B., Heyden, Y. V., Chromatographic separation techniques and data handling methods for herbal fingerprints: A review, Analytica Chimica Acta 690 (2) (2011) 148-161. https://doi.org/10.1016/j.aca.2011.02.023.

[11] Veiga Junior, V. F., Mello, J. C. P., As monografias sobre plantas medicinais, Revista Brasileira de Farmacognosia 18 (3) (2008) 464-471. https://doi.org/10.1590/S0102-695X2008000300022.

[12] Brasil, Agência Nacional de Vigilância Sanitária, Farmacopeia Brasileira, Brasília: Agência Nacional de Vigilância Sanitária 5 (Suppl. 2) (2017) 1-1016. http://portal.anvisa.gov.br/documents/33832/259143/Segundo+Suplemento+FB+5/9cfb1239-875c-4a77-8741-b59416684d29.

[13] Brasil, Agência Nacional de Vigilância Sanitária, Instrução normativa nº 4, de 18 de junho de 2014, Determina a publicação do Guia de orientação para registro de medicamento fitoterápico e registro e notificação de produto tradicional fitoterápico, Diário Oficial da União (2014). http://portal.anvisa.gov.br/documents/33836/2501251/Guia%2Bfinal%2Bdicol%2B180614+%282%29.pdf/f400c535-e803-4911-9ef8-100c0c2bb3c6.

[14] Nalluri, B. N., Kumar, S., Characterization and estimation of harpagoside in dried root extract and oral powder formulations of *Harpagophytum procumbens* by validated RP-HPLC-PDA Method, Journal of Drug Delivery and Therapeutics 9 (2) (2019) 38-46. http://jddtonline.info/index.php/jddt/article/view/2459/1788.

[15] Avato, P., Argentieri, M. P., Quality Assessment of Comercial Spagyric Tinctures of *Harpagophytum procumbens* and Their antioxidant properties, Molecules, 24 (12) (2019) 2-15. https://doi.org/10.3390/molecules24122251.

[16] Leite, C. F. M., Leite, B. H. M., Barros, I. M. C., Gomes, S. M., Fagg, C. W., Simeoni, L. A., Silveira, D., Fonseca, Y. M., Determination of rutin in *Erythroxylum suberosum* extract by liquid chromatography: applicability instandardization of herbs and stability studies, Boletín Latinoamericano y del Caribe de Plantas Medicinales y Aromáticas 13 (2) (2014) 135-143.

[17] Brasil, Agência Nacional de Vigilância Sanitária. Resolução da Diretoria Colegiada nº 166, de 24 de julho de 2017, Dispõe sobre a validação de métodos analíticos e dá outras providências, Diário Oficial da União (2017). http://www.in.gov.br/materia/-/asset_publisher/Kujrw0TZC2Mb/content/id/19194581/do1-2017-07-25-resolucao-rdc-n-166-de-24-de-julho-de-2017-19194412.

[18] European Medicines Agency. ICH Topic Q2B; Note for guidelines on Validation of Analytical Procedures: Text and Methodology, European Medicines Agency (1995). https://www.ema.europa.eu/en/documents/scientific-guideline/ich-q-2-r1-validation-analytical-procedures-text-methodology-step-5_en.pdf.

[19] Bettega, P. V. C., Czlusniak, G. R., Piva, R., Namba, E. L., Ribas, C. R., Grégio, A. M. T., Rosa, E. A. R., Fitoterapia: dos canteiros ao balcão da farmácia, Archives of Oral Research 7 (1) (2011) 89-97. https://periodicos.pucpr.br/index.php/oralresearch/article/view/23149/22243.

[20] Vlachojannis, J., Roufogalis, B. D., Chrubasik, S., Systematic review on the safety of *Harpagophytum* preparations for osteoarthritic and low back pain, Phytotherapy Research 22 (2) (2008) 149-152. https://doi.org/10.1002/ptr.2314.

Eclética Química Journal, vol. 45, n. 1, 2020,47-55
ISSN: 1678-4618
DOI: 10.26850/1678-4618eqj.v45.1.2020.p47-55

Eclética Química Journal

Original article
iq.unesp.br/ecletica

| Vol. 45 | n. 1 | 2020 |

Grain-size mineral analysis of verdete rock coarse and fine aggregates and adjustment to two granulometric distribution models

Aline Amaral Madeira*

Pontifical Catholic University of Minas Gerais (PUC-MG), 500 Dom José Gaspar Av, Belo Horizonte, Minas Gerais, Brazil

*Corresponding author: Aline Amaral Madeira, phone number +55 31 991807451 email address: madeira.alineamaral@gmail.com

ARTICLE INFO

Article history:
Received: July 21, 2019
Accepted: September 17, 2019
Published: January 1, 2020

Keywords:
1. verdete rock
2. grain-size analysis
3. particle size distribution
4. Rosin-Rammler-Bennet model
5. Gates-Gaudin-Schuhmann model

ABSTRACT: The supremacy of the mineral industry added to the necessity to supply the world market demand justifies the continuous research efforts for optimizing of the activities of mineral resource utilization. In an approach of mineral characterization, a grain-size analysis study of coarse and fine aggregates of verdete rock was presented in this work. The particle size distribution (PSD) of two samples of aggregates with granulometry < 2.36 mm was experimentally obtained using sieving techniques and adjustment to Rosin-Rammler-Bennet (RRB) and Gates-Gaudin-Schuhmann (GGS) granulometric distribution models. Both RRB and GGS models regressed well to the experimental data, presenting correlation coefficient values were extremely close between them approximately 0.99. The PSD results indicated that 65.97% dry aggregates and 67.68% wet aggregates had a particle size with mean diameter > 0.0050 mm; a similar behavior of the grain-size distributions presented by dry and wet aggregates; and a tiny presence of fine particles natural in the analyzed ore sample. The results suggested the suitability of the methodology to predict the grain-size performance the verdete ore beyond to show itself as a contribution to the enriching of the mineral characterization of the studied rock, as a potassium potential source for the mineral processing Brazilian industry.

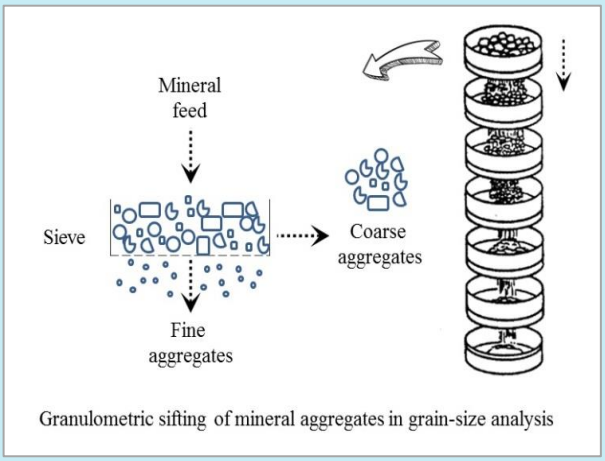

Granulometric sifting of mineral aggregates in grain-size analysis

1. Introduction

Technological advancements in mineral processing operations suggest that continuous research efforts are required to minimize energy consumption, optimize resource utilization, and acquire products with the desired size distribution. Size reduction is probably one of the most fundamental and energy-intensive operations in the mineral processing industry, consuming up until 4% of the electrical energy generated worldwide. Comminution operations and grinding fineness determination are important processes employed to fracture coarse mineral aggregates and liberate value-added materials. Estimations on energy consumption in mining operations in the USA indicate that 39% is used for beneficiation and processing operations, 75% of which is consumed in comminution[1-3].

Grain size may be considered a fundamental physical characteristic property of earth materials, being relevant to their classification and geological origin, as well as for its applications in geotechnics, agricultural engineering, and industrial technology. Moreover, particle size distribution (PSD) influences various activities of resource and energy utilization, and industrial processes, such as the granular materials flow characteristics, flotation and leaching processes, compacting and sintering processes of metallurgical powders, coal combustion process, settling time of cements, among others processes. Particle size can be determined using several techniques, between them sieving, sedimentation, electrozone sensing,

Eclética Química Journal, vol. 45, n. 1, 2020, 56-64
ISSN: 1678-4618
DOI: 10.26850/1678-4618eqj.v45.1.2020.p56-64

microscopy techniques, X-ray attenuation, and laser diffraction[4].

Several models and expressions have been developed to describe the PSD of particulate materials[3]. These models ranging from the normal and log-normal distributions to the Rosin-Rammler-Bennet (RRB) and Gates-Gaudin-Schuhmann (GGS) models. RRB equation is probably the most well-known distribution in the chemical industries, widely used to analyze all types of materials and GGS equation is another uncomplicated popular model used in the metallic ferrous mining industry[5]. RRB and GGS mathematical models have been widely applied to describe the size distribution of several particles types, such as maize grains[2]; fenugreek seed[5]; sorghum bagasse[6]; copper tailing[7]; babassu, canola, castor seed and sunflower residual cakes[8]; particle assemblages[9], and several ores, such as quartz and marble[3]; iron[10]; uranium[11]; phosphate[12]; apatite[13]; chromite[14]; among others. Other numerous granulometric distribution models have also been proposed for greater accuracy in estimating the PSDs, but they have limit applications due to their greater mathematical complexity[1].

In Brazil, one of the most abundant potassium silicates is regionally known as verdete, a metasedimentary rock formed during the Neoproterozoic era. Verdete is a greenish and banded rock, which has fine granulometry and clay matrix, and it is composed essentially by glauconite, quartz, and kaolinite minerals and potassium feldspars[15]. According to Santos *et al.*[16], the rock occurs in Serra da Saudade, Alto Paranaíba Region (MG), geologically located in the San Francisco Craton. The municipality of Cedro do Abaeté is known to have reasonable reserves of verdete (57.4 million tons)[17]. Potassium oxide (K_2O) high contents in the verdete rock were reported in the literature[15,18-20]. According to Silva and Lana[21], the Cedro do Abaeté's verdete may contain until 14% of K_2O.

According to the journal Brasil Mineral[22], the first mineral project of an industrial processing plant of verdete rock recently was inaugurated in Dores do Indaiá, Minas Gerais State, Brazil. Pioneer in the processing of this potassium rock, the complex of the Kalium Mineração S.A. disposes of a glauconite deposit located in the municipalities of Serra da Saudade and Quartel Geral in Minas Gerais, with total reserves of 218 million tons of ore and an average content of 10.6% K_2O. The mining process certified by Intertek predicts an innovative treatment through processing techniques of crushing/grinding; acid cure; aqueous lixiviation; liquid-solid separation; crystallization; thermic decomposition; and sulfuric acid regeneration. The company mining intended the verdete rock use for the potassium salts production, whose processed products may be applicated as potassium fertilizers, for example, seeking to supply part of great demand of the potassium national market[23].

However, a few previous scientific studies worked with the verdete rock until recently. So far, stand out researches involving chemical, stratigraphic, petrographic and mineralogical characterizations were performed[15,19,24,25], besides other technological studies based on thermal treatment focusing on its reactivity increase[20,26] and its metal availability[21,27-31]. No meaningful previous contributions were found that consistently explored the particle size distribution of verdete rock through grain-size analysis and adjustment to RRB and GGS mathematical models.

In this context, based on the relevance of continuous research efforts in mineral processing studies, as well as on the lack of consistent scientific contributions regarding particle size distribution of the verdete rock through the grain-size property, the present article delineates a new study of grain-size of verdete coarse and fine aggregates. For that, this work strives to describe the particle size distribution of such aggregates using sieving techniques and adjustment to Rosin-Rammler-Bennet (RRB) and Gates-Gaudin-Schuhmann (GGS) granulometric distribution models, with the purpose of providing subsidies to a verdete rock characterization as potassium potential source for the mineral processing Brazilian industry.

2. Experimental

Grain-size analysis of verdete rock was realized at environmental conditions at room temperature (298.15 K) under atmospheric pressure (101,325 Pa). Initially, a representative sample of 20 kg of verdete rock from Cedro do Abaeté in Minas Gerais was properly homogenized and ground in a ball mill (Sew-Eurodrive, model FA37B DRE80S4). The grinding product was passed through a 2.36 mm sieve (8 mesh), getting a sample with granulometry < 2.36 mm. Approximately 2.0 kg of verdete rock were weighed on a balance (Urano, model UDC POP).

Eclética Química Journal, vol. 45, n. 1, 2020, 56-64
ISSN: 1678-4618
DOI: 10.26850/1678-4618eqj.v45.1.2020.p56-64

The sample was subjected to the quartering method of size reduction for homogeneous sampling using a Jones riffle splitter (Gilson Company, model SP-173). In the first step, the quartering method divided the sample into two lots of aggregates of 1.0 kg each. Then, one of the lots was subjected again to riffle splitter for apportioning in two lots of 500 g, and so on; quartering was continued until the obtention of two samples of 250.0 g each (A and B).

Sample A (verdete rock dry aggregates) was directly forwarded grain-size analysis. Sample B (verdete rock wet aggregates) was previously washed before of the granulometric test with deionized water obtained from the purifier Gehaka and dried in a kiln (Infinit, model EMT-200) at 373.15 K by approximately 2 h. The washing procedure exclusively intended to remove possible fine particles natural from the ore. The grain-size analysis consisted of one series montage of granulometric sieves and consecutive vibrating sifting of the sample by 10 min under a frequency of 10 Hz. For that, it was used one kit of seven sieves of Tyler standard screen scale of 4, 8, 28, 35, 48, 100, and 200 mesh (Solotest, model 8X2) and a vibrating sieve shaker (Solotest, model 8X2). Posteriorly, the retained aggregates mass fractions on each sieve were weighed on an analytical balance (Shimadzu, model AW220). Tables 1 and 2 present the grain-size analysis experimental data of dry and wet aggregates of verdete rock.

Table 1. Grain-size analysis data of verdete rock dry aggregates.

Tyler Standard Screen Scale / Mesh		Nominal Sieve Opening Size / mm	Nominal Mean Diameter / µm	Nominal Mean Diameter / mm	Mass Retained / g	Percent Retained / %	Cumulative Mass Retained / g	Cumulative Percent Retained / %	Cumulative Mass Passing / g	Cumulative Percent Passing / %
4	+4	4.6990								
8	-4+8	3.3227			0.00	0.00	0.00	0.00	242.02	100.00
28	-8+28	0.5874	1955.05	0.0196	35.04	14.48	35.04	14.48	206.99	85.52
35	-28+35	0.4153	501.35	0.0050	159.67	65.97	194.70	80.45	47.32	19.55
48	-35+48	0.2937	354.50	0.0035	10.94	4.52	205.64	84.97	36.38	15.03
100	-48+100	0.1468	220.25	0.0022	14.10	5.83	219.75	90.80	22.27	9.20
200	-100+200	0.0734	110.10	0.0011	12.18	5.03	231.93	95.83	10.09	4.17
Bottom	-200				9.15	3.78	241.08	99.61	0.94	0.39
					0.94	0.39	242.02	100.00	0.00	0.00
Sum					242.00					

Table 2. Grain-size analysis data of verdete rock wet aggregates.

Tyler Standard Screen Scale / Mesh		Nominal Sieve Opening Size /mm	Nominal Mean Diameter / µm	Nominal Mean Diameter / mm	Mass Retained / g	Percent Retained / %	Cumulative Mass Retained / g	Cumulative Percent Retained / %	Cumulative Mass Passing / g	Cumulative Percent Passing / %
4	+4	4.6990								
8	-4+8	3.3227			0.00	0.00	0.00	0.00	239.97	100.00
28	-8+28	0.5874	1955.05	0.0196	33.26	13.86	33.26	13.86	206.71	86.14
35	-28+35	0.4153	501.35	0.0050	162.42	67.68	195.68	81.54	44.29	18.46
48	-35+48	0.2937	354.50	0.0035	9.77	4.07	205.45	85.61	34.52	14.39
100	-48+100	0.1468	220.25	0.0022	11.59	4.83	217.04	90.44	22.93	9.56
200	-100+200	0.0734	110.10	0.0011	14.34	5.97	231.43	96.42	8.60	3.58
Bottom	-200				7.15	2.98	238.52	99.40	1.45	0.60
					1.45	0.60	239.97	100.00	0.00	0.00
Sum					240.00					

Eclética Química Journal, vol. 45, n. 1, 2020, 56-64
ISSN: 1678-4618
DOI: 10.26850/1678-4618eqj.v45.1.2020.p56-64

Size parameters – number of particles (*N*, Eq. 1); arithmetic mean diameter (D_A, Eq. 2); volumetric mean diameter (D_V, Eq. 3); surface mean diameter (D_S, Eq. 4); Sauter mean diameter (D_{Sauter}, Eq. 5) – and surface parameters – external surface (*S*, Eq. 6) and specific surface (*S/M*, Eq. 7) – of the dry and wet aggregates of verdete rock were measured from experimentally obtained data and presented in Table 3.

$$N = \frac{M}{b.\rho}\sum_{i=1}^{n}\left(\frac{x_i}{{D_i}^3}\right) \quad (1)$$

where: *N* = Number of particles (units); *M* =Total retained mass in the grain-size analysis (g); *b* = factor assuming cubic format particle = 1; ρ = verdete rock density = 2.376 x 10^{-3} g mm^{-3}; x_i = retained weight fraction of a group of particles in the grain-size analysis; D_i = nominal mean diameter of that group (mm).

$$D_A = \sqrt{\frac{\sum_{i=1}^{n}\left(\frac{x_i}{{D_i}^2}\right)}{\sum_{i=1}^{n}\left(\frac{x_i}{{D_i}^3}\right)}} \quad (2)$$

where: D_A = Arithmetic mean diameter (mm); x_i = retained weight fraction of a group of particles in the grain-size analysis; D_i = nominal mean diameter of that group (mm).

$$D_V = \sqrt[3]{\frac{1}{\sum_{i=1}^{n}\left(\frac{x_i}{{D_i}^3}\right)}} \quad (3)$$

where: D_V = Volumetric mean diameter (mm); x_i = retained weight fraction of a group of particles in the grain-size analysis; D_i = nominal mean diameter of that group (mm).

$$D_S = \sqrt{\frac{\sum_{i=1}^{n}\left(\frac{x_i}{D_i}\right)}{\sum_{i=1}^{n}\left(\frac{x_i}{{D_i}^3}\right)}} \quad (4)$$

where: D_S = Surface mean diameter (mm); x_i = retained weight fraction of a group of particles in the grain-size analysis; D_i = nominal mean diameter of that group (mm).

$$D_{Sauter} = \frac{1}{\sum_{i=1}^{n}\left(\frac{x_i}{D_i}\right)} \quad (5)$$

where: D_{Sauter} = Sauter mean diameter (mm); x_i = retained weight fraction of a group of particles in the grain-size analysis; D_i = nominal mean diameter of that group (mm).

$$S = \frac{M*\lambda*\sum_{i=1}^{n}\left(\frac{x_i}{D_i}\right)}{\rho} \quad (6)$$

where: *S* = External surface (cm^2); *M* = Total retained mass in the grain-size analysis (g); λ = factor assuming cubic format particle = 6; x_i = retained weight fraction of a group of particles in the grain-size analysis; D_i = nominal mean diameter of that group (cm); ρ = verdete rock density = 2.376 g cm^{-3}.

$$\frac{S}{M} = \frac{\lambda*\sum_{i=1}^{n}\left(\frac{x_i}{D_i}\right)}{\rho} \quad (7)$$

where: *S/M* = Specific surface (cm^2 g^{-1}); *M* = Sum retained mass of sieves 28 to 200 mesh (g) λ = factor assuming cubic format particle = 6; x_i = retained weight fraction of a group of particles in the grain-size analysis; D_i = nominal mean diameter of that group (cm); ρ = verdete rock density = 2.376 g cm^{-3}.

Table 3. Size and surface parameters of verdete rock aggregates.

Sample	Number of Particles / units	External Surface / cm^2	Specific Surface / cm^2 g^{-1}	Mean Diameter			
				Surface Diameter / mm	Volumetric Diameter / mm	Arithmetic Diameter / mm	Sauter Diameter / mm
Dry Aggregate	28,430,655	13,685.593	59.007	0.213	0.272	0.169	0.447
Wet Aggregate	31,789,452	13,935.833	60.216	0.203	0.262	0.161	0.435

Eclética Química Journal, vol. 45, n. 1, 2020, 56-64
ISSN: 1678-4618
DOI: 10.26850/1678-4618eqj.v45.1.2020.p56-64

3. Results and Discussion

Particle size distribution study of verdete rock dry and wet aggregates was developed from the mass values of the different particle size obtained in the sieving operations converted to the cumulative and percent mass fractions. Figure 1 shows the granulometric curves of dry and wet aggregates. By assessing the retained fractions percent values against the sieve sizes, it was observed an increase in percentage weight retained of the 28 mesh sieve (0.5874 mm) for 35 mesh sieve (0.4153 mm) and a retained weight meaningful decrease starting of sieve 35, as a response to the decrease of opening size. So that 65.97% of dry aggregates and 67.68% of wet aggregates were retained on 35 size sieve, suggesting a particle size with 0.0050 < mean diameter < 0.0196 mm.

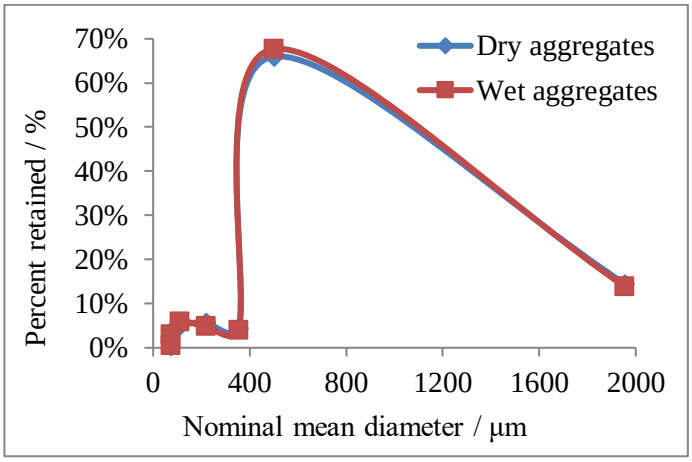

Figure 1. Granulometric curves of verdete rock dry and wet aggregates.

Figure 2 illustrates the grain-size distribution curves of verdete coarse aggregates and Fig. 3 the grain-size distribution curves of verdete fine aggregates. The evolution of the PSD regarding the nominal sieves opening size revealed a distribution with a profile characterized by a decrease of cumulative percent retained in case of the coarse aggregates and an increase of cumulative percent passing of the fine aggregates along of the sieving operations, as expected. The sieving experiments conducted with the wet aggregates (sample B) was previously washed and posteriorly dried intending to remove possible fine particles natural from the ore. It is relevant to emphasize that these particles cannot be confused with fine aggregates with potassium appreciable contents generated by ore fragmentation processes. As could be seen in Figs. 1, 2 and 3, the granulometric curves of dry and wet aggregates exhibited extremely similar profiles suggesting the hypothesis that the verdete ore mother-sample had not an appreciable amount of natural fine particles sufficient to create a significant differentiation between the granulometric distribution of the A and B samples.

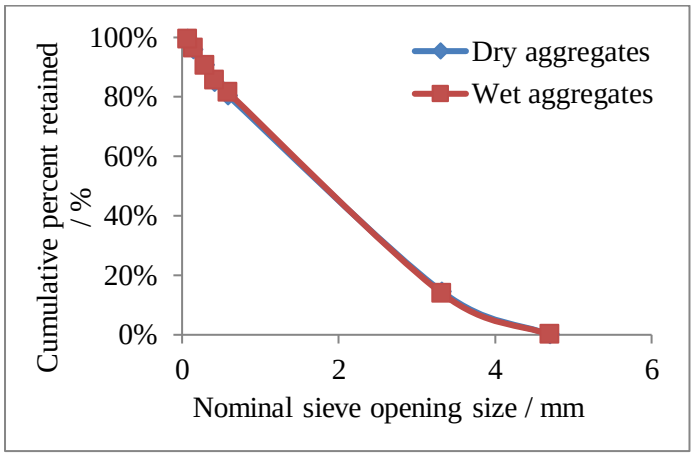

Figure 2. Grain-size distribution curve of verdete dry and wet coarse aggregates.

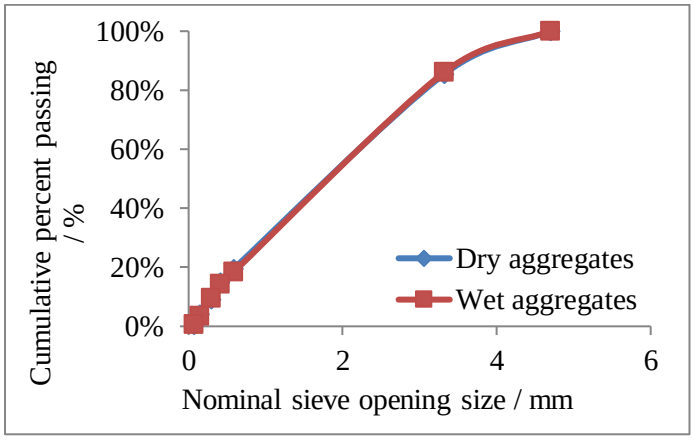

Figure 3. Grain-size distribution curve of verdete dry and wet fine aggregates.

Table 3 lists size and surface parameters of verdete rock's aggregates calculated as defined in equations earlier (Eqs. 1-7) after grain-size analysis via sieve classification. Obtained results for particles number, external and specific surfaces, and mean-diameters showed two particle-populations, the first one composed by dry aggregates and the second population by wet aggregates, with parameters values very similar. Arithmetic, surface, and volumetric mean-diameters obtained values corroborated a particle mean diameter > 0.0050 mm, as foreseen by

Eclética Química Journal, vol. 45, n. 1, 2020, 56-64
ISSN: 1678-4618
DOI: 10.26850/1678-4618eqj.v45.1.2020.p56-64

granulometric curves results. Sauter mean diameter obtained values expressed a larger mean diameter of the dry particulate matter as compared to the wet particulate matter by taking into account the volume-to-surface area ratio.

Grain-size analysis adjustment of verdete rock aggregates was provided by granulometric distribution models of the Rosin-Rammler-Bennet (RRB) and Gates-Gaudin-Schuhmann (GGS), whose nonlinear and linearized equations were presented in Eqs. 8, 9, 10, and 11**,** respectively. Table 4 summarizes intrinsic parameters and nonlinear and linear equations of the RRB and GGS models determined from the obtained experimental data and Fig. 4 shows the granulometric distribution curves and the linearized curves of the RRB and GGS models for verdete rock dry and wet aggregates.

$$X_i = 1 - e^{-\left(\frac{D_i}{D'}\right)^n} \quad (8)$$

$$ln(ln\phi) = n.\,ln\,D_i - n.\,ln\,D' \quad (9)$$

where: X_i = passing weight fraction of a group of particles in the grain-size analysis; $\phi = \frac{1}{1-X_i}$; D_i = nominal mean diameter of that group (μm); n = uniformity coefficient that stands for the width of PSD; D' = characteristic particle diameter (reflecting the particle size of most particles).

$$X_i = \left(\frac{D_i}{k}\right)^m \quad (10)$$

$$ln\,X_i = m.\,ln\,D_i - m\,.\,ln\,k \quad (11)$$

where: X_i = passing weight fraction of a group of particles in the grain-size analysis; D_i = nominal mean diameter of that group (μm); k = maximum particle diameter of the distribution (size modulus) that locates the distribution in overall size spectrum (μm); m = distribution modulus, that measure the broadness of the size distribution.

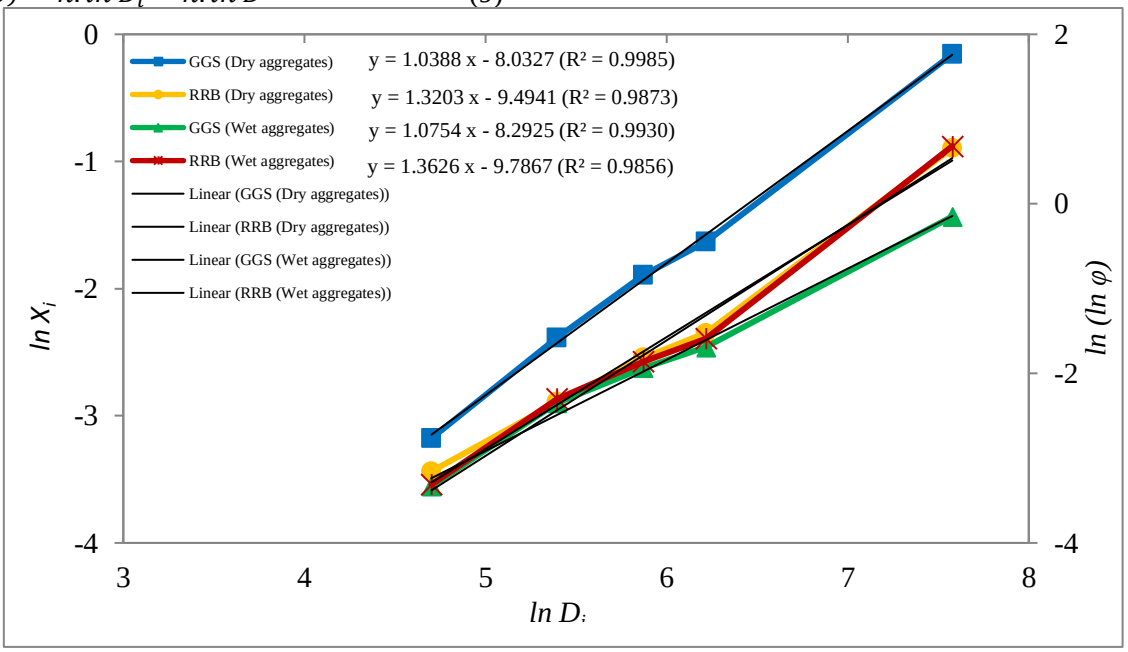

Figure 4. Linearized curves of the Rosin-Rammler-Bennet (RRB) and Gates-Gaudin-Schuhmann (GGS) mathematical models for verdete rock dry and wet aggregates.

Both RRB and GGS granulometric distribution models regressed well to the experimental PSD data, as can be seen in Table 4. The models accuracy was assessed using the correlation coefficient (R^2). The found R^2 values were extremely close between them, all *circa* 0.99, suggesting good quality experimental data. It can be asserted, even if in a tenuous way, that the higher R^2 values of GGS model (nearest 1 unit) suggest a slightly more suitable distribution of Gates-Gaudin-Schuhmann model, as compared to Rosin-Rammler-Bennet model, to represent PSD of verdete rock dry and wet aggregates.

Eclética Química Journal, vol. 45, n. 1, 2020, 56-64
ISSN: 1678-4618
DOI: 10.26850/1678-4618eqj.v45.1.2020.p56-64

Table 4. Rosin-Rammler-Bennet (RRB) and Gates-Gaudin-Schuhmann (GGS) mathematical model parameters and determined equations.

Sample	Granulometric Distribution Model	Parameters		Nonlinear equation	Linear equation	Correlation Coefficient (R^2)
Dry Aggregate	RRB	n	D'	$X_i = 1 - e^{\left[-\left(\frac{D_i}{1327.2517}\right)^{1.3203}\right]}$	$ln\left[ln\left(\frac{1}{1-X_i}\right)\right] = 1.3203\ ln\ D_i - 9.4941$	0.9873
		1.3203	1,327.2517			
	GGS	k	m	$X_i = \left(\frac{D_i}{2281.6915}\right)^{1.0388}$	$ln\ X_i = 1.0388\ ln\ D_i - 8.0327$	0.9985
		2,281.6915	1.0388			
Wet Aggregate	RRB	n	D'	$X_i = 1 - e^{\left[-\left(\frac{D_i}{1316.0261}\right)^{1.3626}\right]}$	$ln\left[ln\left(\frac{1}{1-X_i}\right)\right] = 1.3626\ ln\ D_i - 9.7867$	0.9856
		1.3626	1,316.0261			
	GGS	k	m	$X_i = \left(\frac{D_i}{2232.9620}\right)^{1.0754}$	$ln\ X_i = 1.0754\ ln\ D_i - 8.2925$	0.9930

According to Liu *et al.*[32], D' and n parameters of RRB distribution model play a dominant role in the determination of the distribution characteristics, in other words, the PSD of any particle system described by using this model can be distinguished with values of D' and n. Lower values of m parameter of GGS distribution model suggest that more fine aggregates, more large particles (coarse aggregates) and fewer particles in the middle range will be produced[33]. Comparing the RRB and GGS models parameters obtained for dry and wet aggregates, it was observed a good convergence between the found values, corroborating the hypothesis that the ore mother-sample did not have an amount of fine particles sufficient to create appreciable differentiation between the A and B samples, as foreseen in results obtained by granulometric curves and size and surface parameters.

Due to the lack of studies in the literature dedicated to the description of the particle size distribution of the verdete rock aggregates and its modeling through RRB and GGS models, the work presented here suggests the suitability of the methodology proposed by means of sieving techniques for predicting the grain-size performance the verdete rock beyond enriching its mineral characterization. The developed study could be optimized and enlarged in the purpose to corroborate the described forecasts and to increase of the results representativeness. In this sense, it is recommended to use the method described with other verdete ore granulometry and coming of other mineral reserves, as well as to realize the sieving experiments in triplicate.

4. Conclusions

A grain-size analysis study of verdete rock and adjustments to the Rosin-Rammler-Bennet (RRB) and Gates-Gaudin-Schuhmann (GGS) granulometric distribution models were satisfactorily developed through sieving techniques with sieves of Tyler standard screen scale of 4, 8, 28, 35, 48, 100, and 200 mesh. Both RRB and GGS granulometric models regressed well to the experimental particle size distribution data, presenting correlation coefficient values were extremely close between them approximately 0.99. The PSD results suggested that: 65.97% dry aggregates and 67.68% wet aggregates had a particle size with mean diameter > 0.0050 mm; an extremely similar behavior of the grain-size distributions presented by samples of ore dry and wet aggregates; and a tiny presence of fine particles natural from the analyzed ore sample. The results suggested the suitability of the methodology proposed by work to predict the grain-size performance the verdete ore beyond to show itself as a contribution to the enriching of the mineral characterization of the studied rock, as a potassium potential source for the mineral processing Brazilian industry.

5. References

[1] Ahmed, M. M., A contribution to new measure for evaluation of a particle size distribution, Mineral Processing and Extractive Metallurgy: Transactions of the Institution of Mining and Metallurgy: Section C 116 (4) (2007) 221-230. http://doi.org/10.1179/174328507X198726.

Eclética Química Journal, vol. 45, n. 1, 2020, 56-64
ISSN: 1678-4618
DOI: 10.26850/1678-4618eqj.v45.1.2020.p56-64

[2] Bolaji, O. T., Awonorin, S. O., Sanni, L. O., Shittu, T. A., Adewumi, J. K., Modeling of particle size distribution and energy consumption of wet milled maize at varying soaking period and method in the production of Ogi, Particulate Science and Technology 37 (1) (2017) 94-102. https://doi.org/10.1080/02726351.2017.1343882.

[3] Petrakis, E., Stamboliadis, E., Komnitsas, K., Evaluation of the relationship between energy input and particle size distribution in comminution with the use of piecewise regression analysis, Particulate Science and Technology 35 (4) (2016) 479-489. https://doi.org/10.1080/02726351.2016.1168894.

[4] Kimura, S., Ito, T., Minagawa, H., Grain-size analysis of fine and coarse non-plastic grains: comparison of different analysis methods, Granular Matter 20 (3) (2018) 1-15. https://doi.org/10.1007/s10035-018-0820-3.

[5] Savitha, HG., Manohar, B., Studies on grinding and extraction of oil from fenugreek (*Trigonella foenum-graecum*) seed, International Journal of Food Engineering 11 (2) (2015) 275-283. https://doi.org/10.1515/ijfe-2014-0262.

[6] Miranda, M. R., Cardoso, C. R., Ataíde, C. H., Physical and chemical characterization of sorghum bagasse, Materials Science Forum 727-728 (2012) 1683-1688. https://doi.org/10.4028/www.scientific.net/MSF.727-728.1683.

[7] Liu, S., Li, Q., Song, J., Study on the grinding kinetics of copper tailing powder, Powder Technology 330 (2018) 105-113. https://doi.org/10.1016/j.powtec.2018.02.025.

[8] Castro, A. M., Castilho, L. R., Freire, D. M. G., Characterization of babassu, canola, castor seed and sunflower residual cakes for use as raw materials for fermentation processes, Industrial Crops and Products 83 (2016) 140-148. https://doi.org/10.1016/j.indcrop.2015.12.050.

[9] Cho, J., Sohn, H. Y., Effects of particle shape and size distribution on the overall fluid-solid reaction rates of particle assemblages, The Canadian Journal of Chemical Engineering 94 (8) (2016) 1516-1523. https://doi.org/10.1002/cjce.22533.

[10] Singh, M., Kumar, S., Kumar, S., Nandan, G., Gupta, M., Characterization of iron-ore suspension at in-situ conditions, Materials today: proceedings 5 (9) (2018) 17845-17851. https://doi.org/10.1016/j.matpr.2018.06.110.

[11] Kacham, A. R., Suri, A. K., Application of a topochemical reaction model to predict leaching behavior of high carbonate uranium ores in alkaline solutions: an experimental case study, Hydrometallurgy 141 (2014) 67-75. https://doi.org/10.1016/j.hydromet.2013.10.005.

[12] Xiong, Y., Wu, B., Zhu, J., Fan, X., Cai, P., Wen, J., Liu, X., Preparation of magnesium hydroxide from leachate of dolomitic phosphate ore with dilute waste acid from titanium dioxide production, Hydrometallurgy 142 (2014) 137-144. https://doi.org/10.1016/j.hydromet.2013.11.013.

[13] Santana, R. C., Ribeiro, J. A., Santos, M. A., Reis, A. S., Ataíde, C. H., Barrozo, M. A. S., Flotation of fine apatitic ore using microbubbles, Separation and Purification Technology 98 (2012) 402-409. https://doi.org/10.1016/j.seppur.2012.06.014.

[14] Taşdemir, A., Taşdemir, T., Comparative study on PSD models for chromite ores comminuted by different devices. Particle and Particle Systems Characterization 26 (1-2) (2009) 69-79. https://doi.org/10.1002/ppsc.200800035.

[15] Piza, P. A. T., Bertolino, L. C., Silva, A. A. D., Sampaio, J. A., Luz, A. B., Verdete da região de Cedro de Abaeté (MG) como fonte alternativa para potássio, Geociências 30 (3) (2011) 345-356. https://www.periodicos.rc.biblioteca.unesp.br/index.php/geociencias/article/view/5551.

[16] Santos, W. O., Mattiello, E. M., Costa, L. M., Abrahão, W. A. P., Characterization of verdete rock as a potential source of potassium, Revista Ceres 62 (4) (2015) 392-400. https://doi.org/10.1590/0034-737X201562040009.

[17] Santos, W. O., Mattiello, E. M., Vergutz, L., Costa, R. F., Production and evaluation of potassium fertilizers from silicate rock, Journal of Plant Nutrition and Soil Science 179 (4) (2016) 547-556. https://doi.org/10.1002/jpln.201500484.

[18] Guimarães, D., Geologia do Brasil, Rio de Janeiro, 1964.

[19] Moreira, D. S., Uhlein, A., Fernandes, M. L. S., Mizusaki, A. M., Galéry, R., Delbem, I. D., Estratigrafia, petrografia e mineralização de potássio em siltitos verdes do grupo Bambuí na região de São Gotardo, Minas Gerais, Geociências 35 (2) (2016) 157-171. http://www.ppegeo.igc.usp.br/index.php/GEOSP/article/view/9016/8281.

Eclética Química Journal, vol. 45, n. 1, 2020, 56-64
ISSN: 1678-4618
DOI: 10.26850/1678-4618eqj.v45.1.2020.p56-64

[20] Silva, A. A. S., Medeiros, M. E., Sampaio, J. A., Garrido, F. M. S., Verdete de Cedro do Abaeté como fonte de potássio: caracterização, tratamento térmico e reação com CaO, Matéria (Rio de Janeiro) 17 (3) (2012) 1062-1074. https://doi.org/10.1590/S1517-70762012000300004.

[21] Silva, A. A., Lana, R. M. Q., Incubação do verdete com diferentes fontes de ácidos para disponibilização de potássio, cálcio, magnésio do solo, Holos 5 (2015) 73-83. https://doi.org/10.15628/holos.2015.3210.

[22] Revista Brasil Mineral, Potássio: Projeto da Kalium opera em novembro, 2018. http://www.brasilmineral.com.br/noticias/projeto-da-kalium-opera-em-novembro.

[23] Kalium Mineração S.A., Projeto Glauconita, KM Kalium Mineração S.A. (2017) 1-41. https://docplayer.com.br/74701318-Km-kalium-mineracao-s-a-projeto-glauconita.html.

[24] Silva, A. A. S., Medeiros, M. E., Sampaio J. A., Garrido, F. M. S., Caracterização do verdete de Cedro do Abaeté para o desenvolvimento de um material com liberação controlada de potássio, Holos 5 (2012) 42-51. https://doi.org/10.15628/holos.2012.1093.

[25] Lima, O. N. B., Uhlein, A., Britto, W., Estratigrafia do grupo Bambuí na Serra da Saudade e geologia do depósito fosfático de Cedro do Abaeté, Minas Gerais, Revista Brasileira de Geociências 37 (4, suppl.) (2007) 204-215. https://doi.org/10.25249/0375-7536.200737S4204215.

[26] Santos, W. O., Mattiello, E. M., Pacheco, A. A., Vergutz, L., Souza-Filho, L. F. S., Abdala, D. B., Thermal treatment of a potassium-rich metamorphic rock in formation of soluble K forms, International Journal of Mineral Processing 159 (2017) 16-21. https://doi.org/10.1016/j.minpro.2016.12.004.

[27] Eichler, V., Lopes, A. S., Disponibilidade do potássio do Verdete de Abaeté, calcinado com e sem calcário magnesiano, para a cultura do milho (*Zea mays* L.), em solo de textura argilosa, Ciência e Prática 7 (2) (1983) 136-156.

[28] Leite, P. C., Efeitos de tratamentos térmicos em misturas de verdete de Abaeté, fosfato de Araxá e calcário magnesiano, na disponibilidade de potássio e fósforo. 1985. 146 f. Dissertation (Master's in Agronomy) - School of Agriculture of Lavras, Lavras, 1985.

[29] Martins, V., Gonçalves, A. S. F., Marchi, G., Guilherme, L. R. G., Martins, E. S., Solubilização de potássio em misturas de verdete e calcário tratadas termoquimicamente, Pesquisa Agropecuária Tropical 45 (1) (2015) 66-72. https://doi.org/10.1590/1983-40632015v4527917.

[30] Pereira, A. C., Carvalho, I. S. B., Rocha, S. D. F., Glauconite-bearing rocks as alternative potassium source for fertilizer by thermal processing with additives, Brazilian Applied Science Review 3 (2) (2019) 1455-1467. https://doi.org/10.34115/basrv3n2-050.

[31] Pereira, A. C., Becheleni, E. M. A., Gomes, M. R. S., Rocha, S. D. F., Fluoride aided potassium extraction from Verdete rock by thermal processing with ferrous sulfate heptahydrate, Brazilian Applied Science Review 3 (2) (2019) 1373-1384. http://www.brjd.com.br/index.php/BASR/article/view/1565.

[32] Liu, S., Li, Q., Xie, G., Li, L., Xiao, H., Effect of grinding time on the particle characteristics of glass powder, Powder Technology 295 (2016) 133-141. https://doi.org/10.1016/j.powtec.2016.03.030.

[33] Lu, P., Jefferson, I. F., Rosenbaum, M. S., Smalley, I. J., Fractal characteristics of loess formation: evidence from laboratory experiments, Engineering Geology 69 (3-4) (2003) 287-293. https://doi.org/10.1016/S0013-7952(02)00287-9.

Eclética Química Journal, vol. 45, n. 1, 2020, 56-64
ISSN: 1678-4618
DOI: 10.26850/1678-4618eqj.v45.1.2020.p56-64

Eclética Química Journal

Original article
iq.unesp.br/ecletica

| Vol. 45 | n. 1 | 2020 |

Bound state solutions of the Schrödinger equation with energy-dependent molecular Kratzer potential via asymptotic iteration method

Akpan Ndem Ikot[1], Uduakobong Okorie[1,2], Alalibo Thompson Ngiangia[1], Clement Atachegbe Onate[3], Collins Okon Edet[1+], Ita Okon Akpan[4], Precious Ogbonda Amadi[1]

1. University of Port Harcourt, Department of Physics, Theoretical Physics Group, Nigeria
2. Akwa Ibom State University, Department of Physics, Ikot Akpaden, Nigeria
3. Landmark University, Department of Physical Sciences, Omu-Aran, Nigeria
4. University of Calabar, Department of Physics, Nigeria

[+]Corresponding author: Collins Okon Edet, email address: collinsokonedet@gmail.com

ARTICLE INFO

Article history:
Received: July 21, 2019
Accepted: October 24, 2019
Published: January 1, 2020

Keywords:
1. Kratzer potential
2. Schrödinger equation
3. asymptotic iteration method
4. bound state

ABSTRACT: In this paper, we obtained the exact bound state energy spectrum of the Schrödinger equation with energy dependent molecular Kratzer potential using asymptotic iteration method (AIM). The corresponding wave function expressed in terms of the confluent hypergeometric function was also obtained. As a special case, when the energy slope parameter in the energy-dependent molecular Kratzer potential is set to zero, then the well-known molecular Kratzer potential is recovered. Numerical results for the energy eigenvlaues are also obtained for different quantum states, in the presence and absence of the energy slope parameter. These results are discussed extensively using graphical representation. Our results are seen to agree with the results in literature.

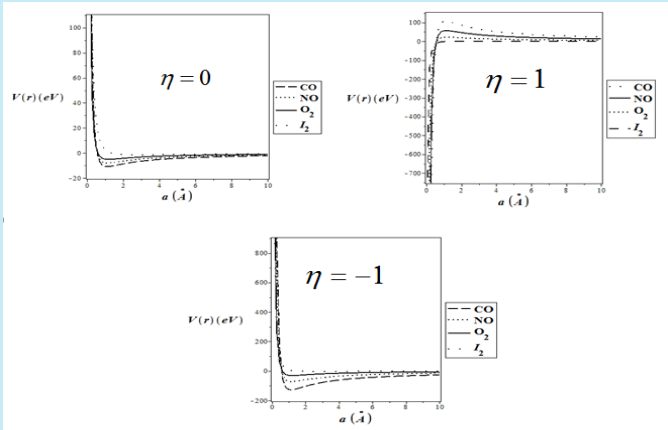

1. Introduction

The exact or approximate solutions of the Schrödinger equations play a vital role in many branches of modern physics and chemistry[1,2]. The solution of this equation is used in the description of particle dynamics in the non-relativistic regime[3,4]. Even though the Schrödinger equation was developed many decades ago, it is still very challenging to solve it analytically[5,6]. The solution of the Schrödinger equation contains all the necessary information needed for the full description of a quantum state such as the probability density and entropy of the system[7,8]. The Schrödinger equation with many physical potentials model have been investigated in recent times with different advance mathematical technique such as Nikiforov-Uvarov (NU) method[9-11], asymptotic iteration method (AIM)[12-16], functional analysis approach[16], supersymmetric quantum mechanics (SUSYQM)[17-20] among others[21]. One of such potential models is the Kratzer potential[22],

$$V(r) = -2D\left(\frac{a}{r} - \frac{1}{2}\frac{a^2}{r^2}\right) \qquad (1)$$

where D is the dissociation energy and a is the equilibrium internuclear length.

The Kratzer potential has been used as a potential model to describe internuclear vibration of diatomic molecules[23,24]. Many authors have investigated the bound state solutions of the Kratzer potential within relativistic and non-relativistic quantum mechanics[25,26]. Recently, Budaca[27] studied an energy-dependent Coulomb-

Eclética Química Journal, vol. 45, n. 1, 2020, 65-76
ISSN: 1678-4618
DOI: 10.26850/1678-4618eqj.v45.1.2020.p65-77

like potential within the framework of Bohr Hamiltonian. Furthermore, Budaca[27] had reported that the energy dependence on the coupling constant of the potential drastically changes the analytical properties of wave function and the corresponding eigenvalues of the system. The energy-dependent potentials have been studied in nuclear physics with applications to quark confinement[28,29]. Several researchers have also given great attention to investigate the energy dependent potentials[30,31]. Boumali and Labidi[32] solved the Klein-Gordon equation with an energy-dependent potential, the Shannon and Fisher information theory was also considered. Also, Lombard *et.al.*[33] studied the wave equation energy-dependent potential for confined systems. Therefore, the energy dependent potential in the Schrödinger equation or other wave equation in physics has many applications such as features in spectrum of confined systems and heavy quark systems in nuclear and molecular physics[34].

In this paper, we shall study the influence of the energy-dependent Kratzer potential on some diatomic molecules defined as:

$$V(r,E) = -2D\left(\frac{a(1+\eta E)}{r} - \frac{1}{2}\frac{a^2(1+\eta E)}{r^2}\right) \qquad (2)$$

where the energy slope parameter η must be positive definite in order to describe a physical system[27].

The shape of the energy dependent Kratzer molecular potential with different energy slope parameters, as it varies with equilibrium internuclear length are illustrated in Fig. 1A-1C, for four selected diatomic molecules (CO, NO, O_2 and I_2).

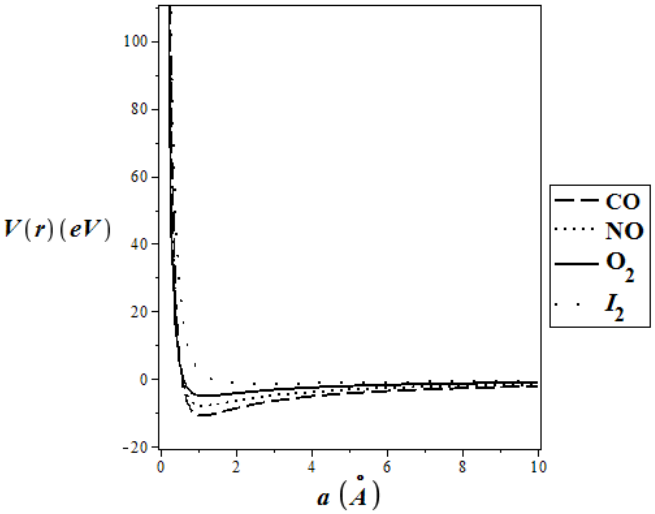

Figure 1A. The shape of Energy-dependent Kratzer molecular potential for different diatomic molecules, with $\eta = 0$.

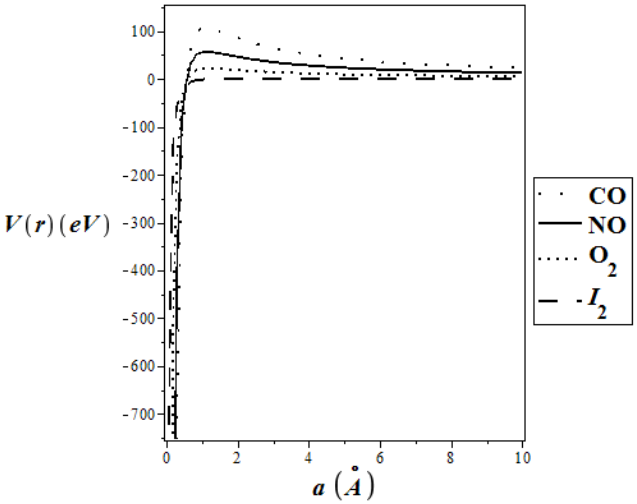

Figure 1B. The shape of Energy-dependent Kratzer Molecular Potential for different diatomic molecules, with $\eta = 1$.

Eclética Química Journal, vol. 45, n. 1, 2020, 65-76
ISSN: 1678-4618
DOI: 10.26850/1678-4618eqj.v45.1.2020.p65-77

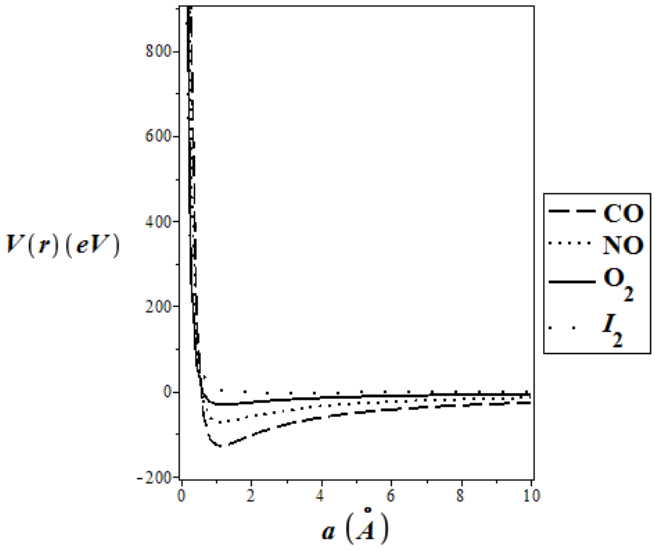

Figure 1C. The shape of Energy-dependent Kratzer molecular potential for different diatomic molecules, with $\eta = -1$.

2 Asymptotic Iteration Method

The AIM has been proposed and used to solve the homogenous linear second-order differential equation of the form[12-16]:

$$y''(x) = \lambda_0(x)y'(x) + s_0(x)y(x) \tag{3}$$

where $\lambda_0 \neq 0$ and the prime denote the derivative with respect to x.

The functions, $s_0(x)$ and $\lambda_0(x)$ must be sufficiently differentiable. Differentiating Eq. 3 with respect to x, we get

$$y'''(x) = \lambda_1(x)y'(x) + s_1(x)y(x) \tag{4}$$

where,

$$\begin{aligned} \lambda_1(x) &= \lambda_0'(x) + \lambda_0^2(x) + s_0(x) \\ s_1(x) &= s_0'(x) + s_0(x)\lambda_0(x) \end{aligned} \tag{5}$$

Taking the second derivative of Eq. 3 yields

$$y''''(x) = \lambda_2(x)y'(x) + s_2(x)y(x) \tag{6}$$

where,

$$\begin{aligned} \lambda_2(x) &= \lambda_1'(x) + \lambda_0(x)\lambda_1(x) + s_1(x) \\ s_2(x) &= s_1'(x) + s_0(x)\lambda_1(x) \end{aligned} \tag{7}$$

Again by taking the $(k+1)th$ and $(k+2)th$ order derivative of Eq. 3 for $k = 1, 2, 3....$, we obtain the following differential equations:

$$\begin{aligned} y^{(k+1)}(x) &= \lambda_{k-1}(x)y'(x) + s_{k-1}(x)y(x) \\ y^{(k+2)}(x) &= \lambda_k(x)y'(x) + s_k(x)y(x) \end{aligned} \tag{8}$$

where,

$$\begin{aligned} \lambda_{k-1}(x) &= \lambda_{k-2}'(x) + \lambda_0(x)\lambda_{k-2}(x) + s_{k-2}(x) \\ s_{k-1}(x) &= s_0(x)\lambda_{k-2}(x) + s_{k-2}'(x) \\ \lambda_k(x) &= \lambda_{k-1}'(x) + \lambda_0(x)\lambda_{k-1}(x) + s_{k-1}(x) \\ s_k(x) &= s_0(x)\lambda_{k-1}(x) + s_{k-1}'(x) \end{aligned} \tag{9}$$

Solving Eq. 8, we obtain the following relation:

$$\frac{y^{(k+2)}(x)}{y^{(k+1)}(x)} = \frac{\lambda_k(x)\left[y'(x) + \dfrac{s_k(x)}{\lambda_k(x)}y(x)\right]}{\lambda_{k-1}(x)\left[y'(x) + \dfrac{s_{k-1}(x)}{\lambda_{k-1}(x)}y(x)\right]} \tag{10}$$

For sufficiently large values of k, the $\alpha(x)$ values are obtained as

$$\frac{s_k(x)}{\lambda_k(x)} = \frac{s_{k-1}(x)}{\lambda_{k-1}(x)} = \alpha(x) \tag{11}$$

This method consists of converting the Schrödinger-like equation into the form of Eq. 3 for a given potential model. The corresponding energy eigenvalues are calculated by means of the quantization condition[12-16].

$$\delta_k(x) = s_k(x)\lambda_{k-1}(x) - \lambda_k(x)s_{k-1}(x), k = 1, 2, 3.... \tag{12}$$

The general solutions of Eq. 3 is obtain from Eq. 10 as:

$$y(x) = \exp\left(-\int^x \alpha(x_1)dx_1\right)\left[C_2 + C_1\int^x \exp\left(\int^x \left[\lambda_0(x_2) + 2\alpha(x_2)\right]dx_2\right)dx_1\right] \tag{13}$$

where C_1 and C_2 are integration constant.

Eclética Química Journal, vol. 45, n. 1, 2020, 65-76
ISSN: 1678-4618
DOI: 10.26850/1678-4618eqj.v45.1.2020.p65-77

Also, the eigenfunction can be obtained by transforming the Schrödinger-like equation of the form:

$$y''(x)=2\left(\frac{ax^{N+1}}{1-bx^{N+2}}-\frac{t+1}{x}\right)y'(x)-\frac{Wx^{N}}{1-bx^{N+2}}y(x) \quad (14)$$

The exact solutions for Eq. 14 are given by

$$y(x)=(-1)^{2}C(N+2)(\sigma)_{n}\,{}_{2}F_{1}\left(-n,\rho+n;\sigma;bx^{N+2}\right) \quad (15)$$

where,

$$(\sigma)_{n}=\frac{\Gamma(\sigma+n)}{\sigma},\sigma=\frac{2t+N+3}{N+2},\rho=\frac{(2t+1)b+2a}{(N+2)b} \quad (16)$$

3. Bound state solution of the Schrödinger equation with energy-dependent Kratzer potential

The radial part of the Schrödinger equation with energy dependent potential $V(r,E_{nl})$ reads[35]:

$$\frac{d^{2}\psi_{nl}}{dr^{2}}+\frac{2\mu}{\hbar^{2}}\left(E_{nl}-V(r,E_{nl})-\frac{l(l+1)\hbar^{2}}{2\mu r^{2}}\right)\psi_{nl}(r)=0 \quad (17)$$

where μ is the reduced mass of the molecules, E_{nl} is the energy of the system, $\hbar$ denotes the reduced Planck constant, n and ℓ represent the principal and orbital angular momentum quantum numbers respectively.

Substituting Eq. 1 into Eq. 17 yields,

$$\frac{d^{2}\psi_{nl}}{dr^{2}}+\frac{2\mu}{\hbar^{2}}\left(E_{nl}+2D\left(\frac{a(1+\eta E)}{r}-\frac{1}{2}\frac{a^{2}(1+\eta E)}{r^{2}}\right)-\frac{l(l+1)\hbar^{2}}{2\mu r^{2}}\right)\psi_{nl}(r)=0 \quad (18)$$

Now using a new variable transformation, $y=ar$, we obtain a second order differential equation of the form:

$$\frac{d^{2}\psi_{nl}}{dy^{2}}+\left[-\varepsilon_{n}^{2}+\frac{\beta}{y}-\frac{\gamma(\gamma+1)}{y^{2}}\right]\psi_{nl}(y)=0 \quad (19)$$

with the following definitions for the used parameters:

$$\varepsilon_{n}^{2}=-\frac{2\mu E_{nl}}{\hbar^{2}a^{2}},\beta=\frac{4\mu D(1+\eta E)}{\hbar^{2}},$$
$$\gamma(\gamma+1)=\frac{2\mu Da^{2}(1+\eta E)}{\hbar^{2}}+l(l+1) \quad (20)$$

In order to transform Eq. 19 into form suitable for the AIM, we write the wave function in the form:

$$\psi_{nl}(y)=y^{\gamma+1}e^{-\varepsilon_{n}y}f(y) \quad (21)$$

Substituting Eq. 21 into Eq. 19, we obtain:

$$f''(y)=\left[\frac{2\varepsilon_{n}y-2(\gamma+1)}{y}\right]f'(y)+\left[\frac{2\varepsilon_{n}(\gamma+1)-\beta}{y}\right]f(y) \quad (22)$$

where,

$$\lambda_{0}(y)=\frac{2\varepsilon_{n}y-2(\gamma+1)}{y},$$
$$s_{0}(y)=\frac{2\varepsilon_{n}(\gamma+1)-\beta}{y} \quad (23)$$

By applying the AIM quantization of Eq. 12 by substituting Eq. 23, we obtain the following iterations:

$$\frac{s_{0}}{\lambda_{0}}=\frac{s_{1}}{\lambda_{1}}\Rightarrow\varepsilon_{0}=\frac{\beta}{2(\gamma_{0}+1)},n=0,$$
$$\frac{s_{1}}{\lambda_{1}}=\frac{s_{2}}{\lambda_{2}}\Rightarrow\varepsilon_{1}=\frac{\beta}{2(\gamma_{1}+2)},n=1, \quad (24)$$
$$\frac{s_{2}}{\lambda_{2}}=\frac{s_{3}}{\lambda_{3}}\Rightarrow\varepsilon_{2}=\frac{\beta}{2(\gamma_{2}+3)},n=2$$

Generally, for arbitrary n, we have

$$\varepsilon_{n}=\frac{\beta}{2(\gamma_{n}+n+1)} \quad (25)$$

Using Eq. 20 with Eq. 25, the energy eigenvalues of the Schrödinger equation with energy-dependent Kratzer potential is obtained as:

Eclética Química Journal, vol. 45, n. 1, 2020, 65-76
ISSN: 1678-4618
DOI: 10.26850/1678-4618eqj.v45.1.2020.p65-77

$$E_{nl} = -\frac{1}{8\mu}\frac{\beta^2\hbar^2a^2}{\left[n+\frac{1}{2}+\frac{1}{2}\sqrt{1+4l\left(l+1\right)+\frac{8\mu Da^2\left(1+\eta E_n\right)}{\hbar^2}}\right]^2} \tag{26}$$

This is a very complicated transcendental energy equation. As a special case, when the energy slope parameter $\eta = 0$, Eq. 26 reduces to the result of the standard Kratzer potential given as:

$$E_{nl} = -\frac{2\mu D^2a^2}{\hbar^2\left(n+\frac{1}{2}+\sqrt{\left(l+\frac{1}{2}\right)^2+\frac{2\mu Da^2}{\hbar^2}}\right)^2} \tag{27}$$

This result is consistent with those reported by Bayrak, Boztosun and Ciftci[29].

4. Results and Discussion

We compute the energy eigenvalues (in eV) of energy dependent Kratzer molecular potential for CO, NO, O_2 and I_2 diatomic molecules. This was done using the spectroscopic parameters given in Table 1, and the conversion $\hbar c = 1973.29\ eV\ \mathring{A}$ [36].

Table 1. Spectroscopic parameters of the various diatomic molecules[29]

Molecule	$D\,(eV)$	$a\,(\mathring{A})$	$\mu\,(amu)$
CO	10.84514471	1.1282	6.860586000
NO	8.043782568	1.1508	7.468441000
O_2	5.156658828	1.2080	7.997457504
I_2	1.581791863	2.6620	63.45223502

The energy eigenvalues of energy dependent molecular Kratzer potential for the ground state diatomic molecules selected are shown in Tables 2 and 3, in the absence of the energy slope parameter η.

Table 2. Energy eigenvalues (in eV) of energy dependent Kratzer molecular potential for different values of n and ℓ for ground states CO and NO diatomic molecules, with $\eta = 0$.

n	ℓ	CO	CO[29]	NO	NO[29]
0	0	-10.79431511	-10.79431532	-8.002659248	-8.002659417
1	0	-10.69383928	-10.69383992	-7.921456326	-7.921456839
	1	-10.69337058	-10.69337123	-7.921043312	-7.921043834
2	0	-10.59475984	-10.59476089	-7.841483114	-7.841483956
	1	-10.59429764	-10.59429869	-7.841076336	-7.841077188
	2	-10.59337335	-10.59337441	-7.840262914	-7.840263771
3	0	-10.49705101	-10.49705246	-7.762714900	-7.762716066
	1	-10.49659519	-10.49659664	-7.762314236	-7.762315413
	2	-10.49568366	-10.49568512	-7.761513040	-7.761514218
	3	-10.49431667	-10.49431814	-7.760311552	-7.760312744
4	0	-10.40068763	-10.40068947	-7.685127602	-7.685129079
	1	-10.40023807	-10.40023992	-7.684732928	-7.684734417
	2	-10.39933907	-10.39934092	-7.683943714	-7.683945203
	3	-10.39799086	-10.39799272	-7.682760192	-7.682761696
	4	-10.39619379	-10.39619567	-7.681182728	-7.681184246

Eclética Química Journal, vol. 45, n. 1, 2020, 65-76
ISSN: 1678-4618
DOI: 10.26850/1678-4618eqj.v45.1.2020.p65-77

5	0	-10.30564512	-10.30564735	-7.608697730	-7.608699509
	1	-10.30520171	-10.30520394	-7.608308928	-7.608310719
	2	-10.30431500	-10.30431723	-7.607531456	-7.607533248
	3	-10.30298523	-10.30298747	-7.606365544	-7.606367349
	4	-10.30121273	-10.30121499	-7.604811550	-7.604813368
	5	-10.29899796	-10.29900024	-7.602869968	-7.602871795

Table 3. Energy eigenvalues (in eV) of energy dependent Kratzer molecular potential for different values of n and ℓ for ground states O_2 and I_2 diatomic molecules, with $\eta = 0$.

n	ℓ	O_2	O_2[29]	I_2	I_2[29]
0	0	-5.126358490	-5.126358625	-1.579082564	-1.579082577
1	0	-5.066640766	-5.066641151	-1.573687115	-1.573687151
	1	-5.066291936	-5.066292323	-1.573677890	-1.573677925
2	0	-5.007960488	-5.007961116	-1.568319272	-1.568319330
	1	-5.007617702	-5.007618329	-1.568310094	-1.568310152
	2	-5.006932272	-5.006932904	-1.568291737	-1.568291796
3	0	-4.950293764	-4.950294624	-1.568291737	-1.562978927
	1	-4.949956880	-4.949957740	-1.562969715	-1.562969796
	2	-4.949283254	-4.949284119	-1.562951452	-1.562951533
	3	-4.948273160	-4.948274034	-1.562924059	-1.562924140
4	0	-4.893617382	-4.893618469	-1.557665652	-1.557665755
	1	-4.893286268	-4.893287355	-1.557656567	-1.557656670
	2	-4.892624178	-4.892625268	-1.557638398	-1.557638501
	3	-4.891631378	-4.891632476	-1.557611144	-1.557611248
	4	-4.890308272	-4.890309388	-1.557574807	-1.557574911
5	0	-4.837908798	-4.837910103	-1.552379504	-1.552379630
	1	-4.837583322	-4.837584627	-1.552370466	-1.552370591
	2	-4.836932504	-4.836933812	-1.552352389	-1.552352514
	3	-4.835956606	-4.835957923	-1.552325274	-1.552325399
	4	-4.834656026	-4.834657357	-1.552289121	-1.552289247
	5	-4.833031292	-4.833032637	-1.552243934	-1.552244060

Our results are very consistent with the results obtained by Bayrak, Boztosun and Ciftci[29]. Also, it is observed that the energy eigenvalues become more bounded as the quantum states of these molecules increases. Moreover, with the introduction of the energy slope parameter, the energy eigenvalues for the different diatomic molecules tends to increase drastically (See Tables 4-6), as compared to the absence of energy slope parameter in Tables 2 and 3.

Eclética Química Journal, vol. 45, n. 1, 2020, 65-76
ISSN: 1678-4618
DOI: 10.26850/1678-4618eqj.v45.1.2020.p65-77

Table 4. Energy eigenvalues (in eV) of energy dependent Kratzer molecular potential for different values of n and ℓ for ground states CO, NO, O_2 and I_2 diatomic molecules, with $\eta = 0.5$.

n	ℓ	CO	NO	O_2	I_2
0	0	-1.685470983	-1.598084322	-1.436597363	-0.8821098304
1	0	-1.679305517	-1.590871796	-1.427770406	-0.8798579292
	1	-1.679233740	-1.590790708	-1.427673989	-0.8798527834
2	0	-1.673229781	-1.583767938	-1.419088479	-0.8776168647
	1	-1.673159688	-1.583688734	-1.418994333	-0.8776117488
	2	-1.673019611	-1.583530439	-1.418806171	-0.8776015171
3	0	-1.667239060	-1.576767407	-1.410544994	-0.8753865376
	1	-1.667170554	-1.576689982	-1.410453001	-0.8753814511
	2	-1.667033643	-1.576535242	-1.410269138	-0.8753712785
	3	-1.666828530	-1.576303400	-1.409993648	-0.8753560203
4	0	-1.661329077	-1.569865334	-1.402133902	-0.8731668498
	1	-1.661262070	-1.569789595	-1.402043954	-0.8731617926
	2	-1.661128150	-1.569638220	-1.401864174	-0.8731516783
	3	-1.660927510	-1.569411413	-1.401594794	-0.8731365078
	4	-1.660660434	-1.569109476	-1.401236158	-0.8731162818
5	0	-1.655495943	-1.563057265	-1.393849636	-0.8709577054
	1	-1.655430353	-1.562983126	-1.393761633	-0.8709526770
	2	-1.655299265	-1.562834945	-1.393585738	-0.8709426205
	3	-1.655102858	-1.562612914	-1.393322171	-0.8709275367
	4	-1.654841404	-1.562317323	-1.392971259	-0.8709074262
	5	-1.654515258	-1.561948551	-1.392533439	-0.8708822905

Eclética Química Journal, vol. 45, n. 1, 2020, 65-76
ISSN: 1678-4618
DOI: 10.26850/1678-4618eqj.v45.1.2020.p65-77

Table 5. Energy eigenvalues (in eV) of energy dependent Kratzer molecular potential for different values of n and ℓ for ground states CO, NO, O_2 and I_2 diatomic molecules, with $\eta = 1$.

n	ℓ	CO	NO	O_2	I_2
0	0	-0.9143283175	-0.8879121698	-0.8355872569	-0.6120188036
1	0	-0.9118740953	-0.8849352196	-0.8316829851	-0.6107178506
	1	-0.9118356154	-0.8848906520	-0.8316274353	-0.6107142849
2	0	-0.9094616292	-0.8820091632	-0.8278482118	-0.6094231767
	1	-0.9094242910	-0.8819658826	-0.8277942378	-0.6094196340
	2	-0.9093497161	-0.8818794293	-0.8276864125	-0.6094125490
3	0	-0.9070878461	-0.8791305048	-0.8240785907	-0.6081347096
	1	-0.9070515614	-0.8790884168	-0.8240260842	-0.6081311896
	2	-0.9069790858	-0.8790043406	-0.8239211853	-0.6081241500
	3	-0.9068706055	-0.8788784754	-0.8237641210	-0.6081135914
4	0	-0.9047500576	-0.8762961642	-0.8203702568	-0.6068523785
	1	-0.9047147491	-0.8762551852	-0.8203191212	-0.6068488809
	2	-0.9046442191	-0.8761733203	-0.8202169568	-0.6068418862
	3	-0.9045386403	-0.8760507547	-0.8200639757	-0.6068313948
	4	-0.9043982696	-0.8758877638	-0.8198604937	-0.6068174077
5	0	-0.9024458954	-0.8735034094	-0.8167197533	-0.6055761139
	1	-0.9024114949	-0.8734634655	-0.8166699025	-0.6055726385
	2	-0.9023427747	-0.8733836647	-0.8165703009	-0.6055656880
	3	-0.9022398959	-0.8732641797	-0.8164211473	-0.6055552630
	4	-0.9021030976	-0.8731052679	-0.8162227378	-0.6055413644
	5	-0.9019326946	-0.8729072681	-0.8159754631	-0.6055239934

Eclética Química Journal, vol. 45, n. 1, 2020, 65-76
ISSN: 1678-4618
DOI: 10.26850/1678-4618eqj.v45.1.2020.p65-77

Table 6. Energy eigenvalues (in eV) of energy dependent Kratzer molecular potential for different values of n and ℓ for ground states CO, NO, O_2 and I_2 diatomic molecules, with $\eta = 2$.

n	ℓ	CO	NO	O_2	I_2
0	0	-0.4774929881	-0.4701556293	-0.4550063750	-0.3795921052
1	0	-0.4765718304	-0.4690143732	-0.4534445388	-0.3789570351
	1	-0.4765520739	-0.4689911448	-0.4534147167	-0.3789548282
2	0	-0.4756699234	-0.4678965624	-0.4519148098	-0.3783251918
	1	-0.4756509229	-0.4678741908	-0.4518860464	-0.3783230016
	2	-0.4756130152	-0.4678295473	-0.4518286336	-0.3783186218
3	0	-0.4747853199	-0.4667999700	-0.4504144000	-0.3776965243
	1	-0.4747669984	-0.4667783719	-0.4503865989	-0.3776943507
	2	-0.4747304393	-0.4667352661	-0.4503311006	-0.3776900040
	3	-0.4746758092	-0.4666708312	-0.4502481107	-0.3776834845
4	0	-0.4739163936	-0.4657227183	-0.4489409312	-0.3770709835
	1	-0.4738986862	-0.4657018233	-0.4489140099	-0.3770688262
	2	-0.4738633478	-0.4656601156	-0.4488602625	-0.3770645119
	3	-0.4738105292	-0.4655977580	-0.4487798774	-0.3770580413
	4	-0.4737404532	-0.4655149913	-0.4486731336	-0.3770494152
5	0	-0.4730617690	-0.4646632066	-0.4474923542	-0.3764485216
	1	-0.4730446207	-0.4646429544	-0.4474662416	-0.3764463803
	2	-0.4730103939	-0.4646025252	-0.4474141038	-0.3764420979
	3	-0.4729592263	-0.4645420684	-0.4473361143	-0.3764356752
	4	-0.4728913214	-0.4644618046	-0.4472325300	-0.3764271130
	5	-0.4728069445	-0.4643620221	-0.4471036873	-0.3764164124

But, the variation of the quantum state with the energy eigenvalues in the presence of the energy slope parameter is in the reverse direction. As the quantum number increases, the energy eigenvalues of energy dependent molecular Kratzer potential becomes more bounded.

Figures 2 and 3 shows the energy eigenvalues variation with the energy slope parameter for different quantum numbers. Both graphs show a similar close trend of increase in energy eigenvalues as the energy slope parameter increases, for different quantum numbers.

Eclética Química Journal, vol. 45, n. 1, 2020, 65-76
ISSN: 1678-4618
DOI: 10.26850/1678-4618eqj.v45.1.2020.p65-77

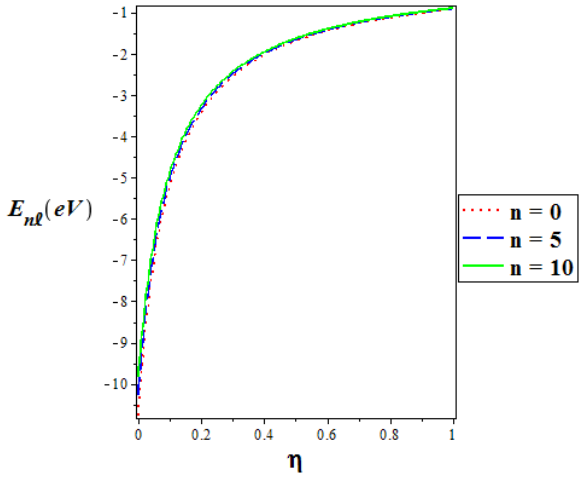

Figure 2. Energy eigenvalues of energy-dependent Kratzer molecular potential vs η for different values of n.

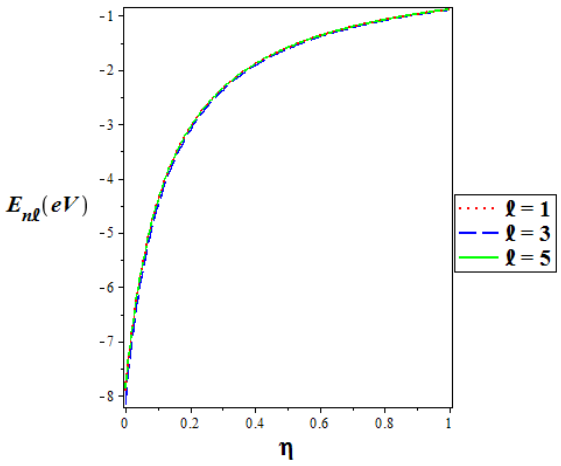

Figure 3. Energy eigenvalues of energy-dependent Kratzer Molecular Potential Vs η for different values of ℓ.

In Fig. 4, there is a diverse behavior of the energy eigenvalues with the potential strength, for different values of the energy slope parameter. Here, there is a direct decrease in energy eigenvalue as the potential strength increase in the absence of the energy slope parameter ($\eta = 0$). With the presence of the energy slope parameter ($\eta = -1$), the energy eigenvalue becomes very bounded with a maximum potential strength of about 1 eV. Similarly, there is a stunted decrease in energy eigenvalue (not more than 1 eV), as the potential strength increase ($\eta = 1$).

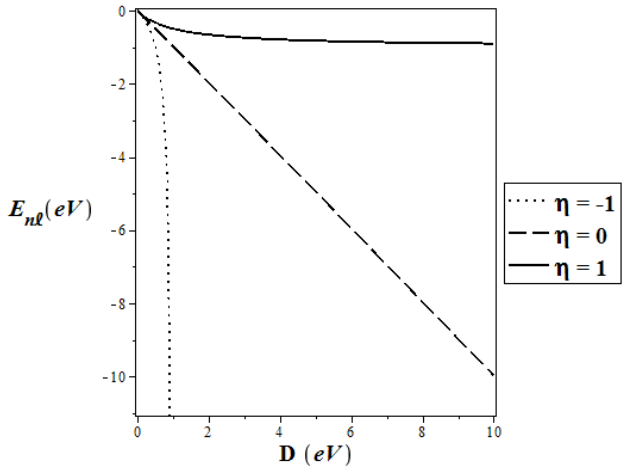

Figure 4. Energy eigenvalues of energy-dependent Kratzer molecular potential vs D for different values of η.

5. Conclusions

We applied the asymptotic iteration method (AIM) to solve the Schrödinger equation with energy dependent molecular Kratzer potential. Its energy eigenvalues and corresponding wave functions in terms of confluent hypergeometric function have been obtained. The numerical results of the energy eigenvalues have been presented in the presence and absence of the energy slope parameter, respectively, for four different diatomic molecules (CO, NO, O_2 and I_2). Our results agree with the results in available literature, especially when the energy slope parameter is set to zero. We have also shown graphically the variation of the energy eigenvalues with some of the potential parameters like energy slope parameter and the potential strength. The behavior of the energy eigenvalues with these parameters is similar in all the diatomic molecules studied. The result obtained in this study finds application in quantum chemistry, molecular physics amongst others.

5. Acknowledgment

The authors thank the kind reviewers for the positive comments and suggestions that lead to an improvement of our manuscript

6. References

[1] Chun-Feng, H., Zhong-Xiang, Z., Yan, L., Bound states of the Klein-Gordon equation with vector and scalar Wood-Saxon potentials, Acta Physica Sinica 8 (8)

Eclética Química Journal, vol. 45, n. 1, 2020, 65-76
ISSN: 1678-4618
DOI: 10.26850/1678-4618eqj.v45.1.2020.p65-77

(1999) 561-565. https://doi.org/10.1088/1004-423X/8/8/001.

[2] Sever, R., Tezan, C., Yesiltas, O., Bucurgat, M., Exact Solution of Effective Mass Schrödinger Equation for the Hulthen Potential, International Journal of Theoretical Physics 47 (9) (2008) 2243-2248. https://doi.org/10.1007/s10773-008-9656-7.

[3] Ikhdair, S. M., An approximate κ state solutions of the Dirac equation for the generalized Morse potential under spin and pseudospin symmetry, Journal of Mathematical Physics 52 (5) (2011) 1-22. https://doi.org/10.1063/1.3583553.

[4] Maghsoodi, E., Hassanabadi, H., Zarrinkamar, S., Spectrum of Dirac Equation Under Deng–Fan Scalar and Vector Potentials and a Coulomb Tensor Interaction by SUSYQM, Few-Body Systems 53 (3-4) (2012) 525-538. https://doi.org/10.1007/s00601-012-0314-5.

[5] Ikot, A. N., Akpabio, L. E., Umoren, E. B., Exact Solution of Schrödinger Equation with Inverted Woods-Saxon and Manning-Rosen Potential, Journal of Scientific Research 3 (1) (2011) 25-33. https://doi.org/10.3329/jsr.v3i1.5310.

[6] Qiang, W. C., Dong, S. H., Analytical approximations to the solutions of the Manning–Rosen potential with centrifugal term, Physics Letters A 368 (1-2) (2007) 13-17. https://doi.org/10.1016/j.physleta.2007.03.057.

[7] Yahya, W. A., Oyewumi, K. J., Thermodynamic properties and approximate solutions of the ℓ-state Pöschl–Teller-type potential, Journal of the Association of Arab Universities for Basic and Applied Sciences 21 (1) (2016) 53-58. https://doi.org/10.1016/j.jaubas.2015.04.001.

[8] Sun, Y., He, S., Jia, C-S., Equivalence of the deformed modified Rosen–Morse potential energy model and the Tietz potential energy model, Physica Scripta 87 (2) (2013) 1-5. https://doi.org/10.1088/0031-8949/87/02/025301.

[9] Edet, C. O., Okoi P. O., Any l-State Solutions of the Schrödinger Equation for q Deformed Hulthen plus Generalized Inverse Quadratic Yukawa Potential in Arbitrary Dimensions, Revista Mexicana de Física 65 (2019) 333-344. https://doi.org/10.31349/RevMexFis.65.333.

[10] Edet, C. O., Okorie, U. S., Ngiangia, A. T., Ikot, A. N., Bound state solutions of the Schrödinger equation for the modified Kratzer potential plus screened Coulomb potential, Indian Journal of Physics (2019) 1-9. https://doi.org/10.1007/s12648-019-01477-9.

[11] Edet, C. O., Okoi P. O., Chima S. O, Analytic solutions of the Schrödinger equation with non-central generalized inverse quadratic Yukawa potential, Revista Brasileira de Ensino de Física 42 (e20190083) (2019) 1-9. https://doi.org/10.1590/1806-9126-RBEF-2019-0083.

[12] Ciftci, H., Hall, R. L., Saad, N., Asymptotic iteration method for eigenvalue problems, Journal of Physics A: Mathematical and General 36 (47) (2003) 11807-11816. https://doi.org//10.1088/0305-4470/36/47/008.

[13] Falaye, B. J., Any ℓ-state solutions of the Eckart potential via asymptotic iteration method, Central European Journal of Physics 10 (4) (2012) 960-965. https://doi.org/10.2478/s11534-012-0047-6.

[14] Qiang, W. C., Dong, S. H., Proper quantization rule, EPL Europhysics Letters 89 (1) (2010) 10003.1-10003.2. https://doi.org/10.1209/0295-5075/89/10003.

[15] Ikhdair, S. M., Sever, R., Exact quantization rule to the Kratzer-type potentials: an application to the diatomic molecules, Journal of Mathematical Chemistry 45 (4) (2009) 1137-1152. https://doi.org/10.1007/s10910-008-9438-8.

[16] Okorie, U. S., Ikot, A. N., Edet, C. O., Akpan, I. O., Sever, R., Rampho, R., Solutions of the Klein Gordon equation with generalized hyperbolic potential in D-dimensions, Journal of Physics Communication 3 (095015) (2019). https://doi.org/10.1088/2399-6528/ab42c6.

[17] Onate, C. A., Ojonubah, J. O., Eigensolutions of the Schrödinger equation with a class of Yukawa potentials via supersymmetric approach, Journal of Theoretical and Applied Physics 10 (1) (2016) 21-26. https://doi.org/10.1007/s40094-015-0196-2.

[18] Ikot, A. N., Obong, H. P., Abbey, T. M., Zare, S., Ghafourian, M., Hassanabadi, H., Bound and scattering state of position dependent mass Klein–Gordon equation with Hulthen plus deformed-type hyperbolic potential, Few-Body Systems 57 (9) (2016) 807-822. https://doi.org/10.1007/s00601-016-1111-3.

[19] Onate, C. A., Onyeaju, M. C., Ikot, A. N., Ojonubah, J. O., Analytical solutions of the Klein–Gordon equation with a combined potential, Chinese Journal of Physics 54 (5) (2016) 820-829. https://doi.org/10.1016/j.cjph.2016.08.007.

[20] Onate, C. A., Ikot, A. N., Onyeaju, M. C., Udoh, M. E., Bound state solutions of D-dimensional Klein–Gordon equation with hyperbolic potential, Karbala International Journal of Modern Science 3 (1) (2017) 1-7. https://doi.org/10.1016/j.kijoms.2016.12.001.

[21] Sadeghi, J., Factorization method and solution of the non-central modified Kratzer potential, Acta Physica Polonica A 112 (1) (2007) 23-28. http://inspirehep.net/record/1426929/files/a112z103.pdf.

[22] Kratzer, A., Die ultraroten rotationsspektren der halogenwasserstoffe, Zeitschrift für Physik A Hadrons and Nuclei 3 (5) (1920) 289-307. https://doi.org/10.1007/BF01327754.

[23] LeRoy, R. J., Bernstein, R. B., Dissociation energy and long-range potential of diatomic molecules from vibrational spacings of higher levels, The Journal of Chemical Physics 52 (8) (1970) 3869-3879. https://doi.org/10.1063/1.1673585.

[24] Ikhdair, S. M., An approximate κ state solutions of the Dirac equation for the generalized Morse potential under spin and pseudospin symmetry, Journal of Mathematical Physics 52 (5) (2011) 052303.1-052303.22. https://doi.org/10.1063/1.3583553.

[25] Saad, N., Hall, R. J., Cifti H., The Klein-Gordon equation with the Kratzer potential in d dimensions, Central European Journal of Physics 6 (3) (2008) 717-729. https://doi.org/10.2478/s11534-008-0022-4.

[26] Hassanabadi, H., Rahimov, H., Zarrinkamar, S., Approximate solutions of Klein-Gordon equation with Kratzer potential, Advances in High Energy Physics 2011 (458087). https://doi.org/10.1155/2011/458087.

[27] Budaca R., Bohr Hamiltonian with an energy-dependent γ-unstable Coulomb-like potential, The European Physical Journal A 52 (2016) 314. https://doi.org/10.1140/epja/i2016-16314-8.

[28] Lombard, R. J., Mareš. J., The many-body problem with an energy-dependent confining potential, Physics Letters A 373 (4) (2009) 426-429. https://doi.org/10.1016/j.physleta.2008.12.009.

[29] Bayrak, O., Boztosun, I., Ciftci, H., Exact analytical solutions to the kratzer potential by the asymptotic iteration method, International Journal of Quantum Chemistry 107 (3) (2007) 540-544. https://doi.org/10.1002/qua.21141.

[30] Hassanabadi, H., Zarrinkamar, S., Rajabi, A. A., Exact solutions of D-dimensional Schrödinger equation for an energy-dependent potential by NU method, Communications in Theoretical Physics 55 (4) (2011) 541-544. https://doi.org/10.1088/0253-6102/55/4/01.

[31] Hassanabadi, H., Zarrinkamar, S., Hamzavi, H., Rajabi, A. A., Exact solutions of D-dimensional Klein–Gordon equation with an energy-dependent potential by using of Nikiforov–Uvarov method, Arabian Journal for Science and Engineering 37 (1) (2012) 209-215. https://doi.org/10.1007/s13369-011-0168-z.

[32] Boumali, A., Labidi, M., Shannon entropy and Fisher information of the one-dimensional Klein–Gordon oscillator with energy-dependent potential, Modern Physics Letters A 33 (6) (2018) 1-26. https://doi.org/10.1142/S0217732318500335.

[33] Lombard, R. J., Mareš, J., Volpe, C., Wave equation with energy-dependent potentials for confined systems, Journal of Physics G: Nuclear and Particle Physics 34 (9) (2007) 1879-1889. https://doi.org/10.1088/0954-3899/34/9/002.

[34] Gupta, P., Mehrotra, I., Study of heavy quarkonium with energy dependent Potential, Journal of Modern Physics 3 (10) (2012) 1530-1536. https://doi.org/10.4236/jmp.2012.310189.

[35] Ikot, A. N., Chukwuocha, E. O., Onyeaju, M. C., Onate, C. A., Ita, B. I., Udoh, M. E., Thermodynamics properties of diatomic molecules with general molecular potential, Pramana 90 (2) (2018) 22-30. https://doi.org/10.1007/s12043-017-1510-0.

[36] Falaye, B. J., Corrigendum: Energy spectrum for trigonometric Pöschl–Teller potential solved by the asymptotic iteration method, Canadian Journal of Physics 91 (4) (2013) 365-367. https://doi.org/10.1139/cjp-2013-0011.

Eclética Química Journal, vol. 45, n. 1, 2020, 65-76
ISSN: 1678-4618
DOI: 10.26850/1678-4618eqj.v45.1.2020.p65-77